QUANTUM MONTE CARLO STUDY
OF HYDROGEN ADSORPTION
ON CARBON AND TRANSITION METAL SYSTEMS

BY

TODD DAVID BEAUDET

DISSERTATION

Submitted in partial fulfillment of the requirements
for the degree of Doctor of Philosophy in Physics
in the Graduate College of the
University of Illinois at Urbana-Champaign, 2010

Urbana, Illinois

Doctoral Committee:

Assistant Professor Dallas R. Trinkle, Chair
Professor Emeritus Richard M. Martin, Director of Research
Professor Munir H. Nayfeh
Professor John D. Stack

Abstract

This thesis research has successfully carried out a QMC study of hydrogen adsorption on Ti-ethylene molecular systems demonstrating reversible hydrogen adsorption on molecular $TiH_2C_2H_4$. This system is chosen as representative of larger carbon-transition-metal systems that may be relevant for practical hydrogen storage. To the author's knowledge this is the first study of hydrogen adsorption on transition metal systems by QMC methods. These systems present challenges in terms of a large number of possible molecular structures that are very close in energy, 3d states of transition elements that are difficult to treat, and molecular geometries that can be difficult to determine.

Several studies are presented that demonstrate the suitability of QMC methods for this class of problem. A QMC study of hydrogen on benzene, which has already been published, tests the Slater-Jastrow (SJ) trial function against a more highly correlated Geminal trial function. The Slater-Jastrow form used here is shown to perform equivalently in measuring the small energy differences associated with physisorption. A series of tests is conducted on the Ti atom transition energies. QMC SJ results are found to be in excellent agreement with experiment so that significant cost savings can be achieved by using a pseudopotential for Ti. An extensive study on the TiH_2 system which is relevant to the final system studied is also presented. There a fixed-node DMC geometry optimization is conducted. It is shown the Perdew-Burke-Ernzerhof (PBE) functional for Density Functional Theory (DFT) is able to give geometries with energies that are within 1.5 mHa of the DMC optimal geometries. Also, it is consistently demonstrated throughout the work that QMC methods with SJ trial functions are only weakly dependent on the single-body theory used to produce the trial function.

The primary results related to hydrogen storage are derived from studies on many structures of Ti-ethylene with up to 5 H_2 molecules. Ground and excited states are both considered. Formation energies are calculated and comparison is made to other work. It is shown that at least three hydrogen molecules can be adsorbed with energies in the range considered relevant for practical hydrogen storage.

To Michelle
and our children

Acknowledgments

First I would like to thank the committee members for taking the time to serve on my committee. I truly appreciate it and know that all of you are very busy people.

There is no doubt, however, the most important help has been my research advisor Prof. Richard M. Martin. Prof. Martin (as I most always call him) has been possibly the most patient person I have personally known. I'm not sure I could have endured this experience were it not for his exceptional patience and kindness. I will always appreciate the countless hours he spent working with me and asking me questions so that I can answer them. I could write pages about the kindness and hospitality Prof. Martin and his wife have shown me. I thank them both.

I would also like to thank Jeongnim Kim for all the time she has spent working with me on several projects. I also want to thank Michele Casula for all that he has done in helping me with my thesis research. Also, I would like to thank all the members of our group for making work the pleasant experience that it has been.

I also want to thank my beautiful wife who has given me the love and support to see this ordeal through to the end. She alone knows what I've went through, the struggles, challenges, and victories. Not only that, the Lord has given us two wonderful boys who have added untold joy to both our lives. Matthew and Michael, I love you. My wife and I are in this together and she has made many sacrifices, some of which I need to remind myself of from time to time - our marriage is not just about me it is about us. In many ways our lives have been on hold for seven years, not just mine but hers too. She doesn't know how much I appreciate and love her.

Most importantly I will thank and acknowledge my Lord and Savior Jesus Christ in giving me the wherewithal and strength to complete this thesis research. I would not have wanted to do it without Him.

This work was supported by the Materials Computation Center at the University of Illinois under NSF grant DMR- 0325939, the U.S. Army MURI grant A6062 UMC00005071-3 and NSF grant DMR04-04853. Calculations were done at the National Center for Supercomputing Applications (NCSA) and Computational Science and Engineering (CSE) facilities at Illinois and resources of the

National Center for Computational Sciences at Oak Ridge National Laboratory, which is supported by the Office of Science of the U.S. Department of Energy under Contract No. WE-AC05-00OR22725.

Table of Contents

List of Tables

List of Figures

List of Abbreviations

AGP	Antisymmetric Geminal Power
BFD	M. Burkatzki, Claudia Filippi, M. Dolg
BSSE	Basis Set Superposition Error
SA-CASSCF	State Averaged Complete Active Space Self Consistent Field theory
CCSD	Coupled Cluster Singles Doubles
CCSD(T)	CCSD with Triples added using perturbation theory
CG	Conjugate Gradient
CI	Configuration Interaction
CISD	Configuration Interaction Singles Doubles
DFT	Density Functional Theory
DMC	Diffusion Monte Carlo
ECP	Effective Core Potentials
FN	Fixed Node
GGA	Generalized Gradient Approximation
GTO	Gaussian Type Orbital
HF	Hartree Fock
HS	Hydrogen Storage
JAGP	Jastrow correlated Antisymmetric Geminal Power
LDA	Local Density Approximation
LRDMC	Lattice Regularized Diffusion Monte Carlo
MC	Monte Carlo
MP2	Møller-Plesset Second Order Perturbation Theory
MRCI	Multi-Reference Configuration Interaction
NCPP	Norm Conserving Pseudopotentials
PBE	Perdew-Burke-Ernzerhof

QMC	Quantum Monte Carlo
ROHF	Restricted Open-shell Hartree-Fock
SJ	Slater-Jastrow
TM	Transition Metal
VdW	van der Waals
VMC	Variational Monte Carlo

Chapter 1

Introduction

1.1 Hydrogen Storage

Research on hydrogen storage systems is timely given the increasingly urgent calls for practical solutions to our energy and environmental problems however, the phenomenon is by no means new. Storing hydrogen in a form other than gas has a long history that starts with Graham's discovery of reversible hydriding in palladium in 1866.[1] Hydrogen was not liquefied until 1898 by James Dewar.[2] Since that time a great deal of study has gone into this subject. Systems such as metal hydrides [3] and complex hydrides [4, 5, 6, 7] have been the source of a great deal of research that continues to this day. More recently, materials such as carbon nanotubes [8], fullerenes [9], metal-organic-frameworks (MOF) [10, 11, 12], and others have been studied.

While many materials have some capacity to store hydrogen reversibly, however small, it is important to quantify what makes a practical hydrogen storage material. The United States Department of Energy has developed a multi-year plan with a set of goals that can result in practical hydrogen storage for a number of applications.[13] In order to meet the plan's time line, by 2010 a material should be found that is able to store hydrogen at $\sim$ 6 wt%, this includes the weight of the tank, storage media and related equipment. This level of hydrogen storage capacity corresponds to about half the hydrogen content of water. The storage should be reversible between -20 to 50°C, stable to $\sim$ 1000 cycles, and have good uptake at 100 atm along with some other detailed considerations. Ultimately, the plan calls for even higher storage capacities and better thermal properties. While many solutions to this problem have been offered, none satisfies all these constraints.

Reversible adsorption at room temperature is indicative of a binding energy of between 7 and 15 mHa/H_2 due to thermodynamic constraints. [11] Binding that is significantly greater will result in irreversible storage while weaker binding will result in poor uptake especially toward the higher temperatures. Additionally, this range of energetics is indicative of hydrogen binding that likely does not break the H-H bond, hence hydrogen binding is often referred to as adsorption or physisorption. This type of bonding is in contrast higher energy binding, sometimes referred to as chemisorption, where cleavage of the hydrogen bond occurs. Further, this energy scale is also suggestive of the physical mechanisms that might be required.

This work will strive toward studying systems where the bonding energetics is in a range compatible with the above constraints. The choice of systems one studies should thus have the correct bonding mechanisms so that such energetics can at least possibly be achieved. While there are generally several bonding mechanisms simultaneously at work in any system, one should consider chiefly those that are dominant. It will prove to be insightful to consider the main bonding mechanisms that can be at work. Namely, dispersion forces, electrostatic forces, and forces due to donor-acceptor physics.

1.2 Physical Mechanisms of Hydrogen Sorption and some Related Materials

A possible means of storing hydrogen can involve breaking the H_2 bond. While breaking this bond is often associated with strongly exothermic reactions, it need not be. In fact, there are classes of chemical reactions that break the H-H bond and yet have energetics suitable for reversible storage. Metal hydrides and complex metal hydrides have been pursued for a long time to this end. As far back as the 1970s, experimental vehicles have been powered by hydrogen stored in metal hydride systems. For example, titanium iron hydride was used but proved to be impractical for a number of reasons.[3] Among the challenges facing these systems are mass and thermal transfer issues and stability under cycling. Hydrogen that is stored by way of chemical reaction is often referred to as a chemisorption process; and while they are worthy of further pursuit, this work focuses on alternative mechanisms that might sidestep some of the above difficulties that result from breaking hydrogen's bond.

There are also possible mechanisms that bond hydrogen without breaking the H-H bond. However, some of these can result in a bond strength that is not sufficiently strong to bond hydrogen at ambient temperatures. Weak binding involving hydrogen can result from several mechanisms. Dispersion forces, also referred to as van der Waals forces, can result in weak binding due to the charge polarization fluctuations in interacting systems. The potential of these forces goes as $-1/r^6$ in the region of non-overlap. Such forces typically result in binding energies on the order of $\sim$1 mHa. Electrostatic forces can also play a role in binding hydrogen. H_2 carries a quadrapole moment of $22.1\text{x}10^{-40}$ Cm^2 that can weakly interact with other charges resulting in a potential that falls off as $-1/r^3$. Such forces can result in binding energetics on the order of between $\sim$1-2 mHa. Additionally, hydrogen can interact by way of a charge induced dipole interactions that fall off as $-1/r^3$. Since H_2 has a polarizability $8.79\text{x}10^{-41}$ $\text{C}^2\text{m}^2\text{J}^{-1}$ these forces can bind with energies on the order of $\sim$2-3 mHa. In a general sense, these interactions alone will not achieve the energies necessary for adsorption. Using $E = k_B T$, 1 mHa corresponds approximately to 300K (room temperature). This sort of bonding is often referred to physisorption and typically results in stability only at low (cryogenic) temperatures. Examples of these kind of systems are pure carbon systems like graphene, carbon nanotubes and fullerenes.[8, 9]

In 1983, Kubas discovered a new type of chemical bonding that results in the stable coordination of an essentially intact molecule of hydrogen.[14] In this bonding mechanism, Donor-acceptor interactions occurring between the *d*-states of a transition metal (TM) and σ-state of H_2 can result in hydrogen bonding with properties that are particularly desirable where hydrogen storage is concerned. This type of hydrogen bonding is sometimes referred to as a *σ-complex* or a *Kubas complex.* Rather than acting like a physisorption mechanism, this type of bonding involves the occupied H_2 σ-states donating to the unoccupied TM *d*-states while the occupied TM *d*-states back-donate to the unoccupied H_2 σ^*-states as shown in Fig. 1.1. It was originally thought that such mechanisms occurred only as an intermediate state in the chemisorption process of breaking the hydrogen bond. However, the seminal discovery of Kubas in 1983 showed that this kind of bonding can result in stable *adsorption* of intact hydrogen molecules. Furthermore, this type of non-classical binding is complementary to π-complex non-classical bonding model, originally put forward by Dewar-Chatt-Duncanson more than 50 years ago.[15] As it turns out, this kind of bonding is highly suitable for reversible hydrogen storage at room temperature almost by definition and in fact can result in the correct energetics for this to occur. It should be noted that if the back donation is too strong then the H-H bond breaks resulting in chemisorption and the donor-acceptor mechanism becomes an intermediate process. To garner this interaction for practical hydrogen storage candidate systems must be carefully studied so that the energetics and other properties of the system are properly tuned.

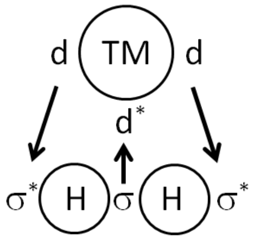

Figure 1.1: σ-Bond donor-acceptor bonding mechanism. Here, TM indicates a transition metal. The bond is stabilized by the interaction between the metal *d*-states and the H_2 σ-states. Specifically, the occupied σ-states donate to the unoccupied TM d^*-states while the occupied TM *d*-states back-donate to the unoccupied σ^*-states respectively.

1.3 Motivation for using Quantum Monte Carlo Methods

Quantum Monte Carlo (QMC) methods have been successfully applied to a variety of systems where electron correlations play an important role. Other investigators have successfully treated systems such as high pressure hydrogen and transition metals with excellent results. Historically, systems that involve adsorption of hydrogen, which is the focus here, are treated with methods such as Hartree-Fock, Density Functional Theory (DFT), or other higher level deterministic theories such as Configuration Interaction (CI) or Couple Cluster (CC) methods. Monte Carlo methods address many of the short comings of these various methods while providing high accuracy in a broad variety of circumstances. To our knowledge, QMC has not been used to study hydrogen adsorption on transition metals.

A number of standard methods are typically applied to molecular systems. While these methods have proven to be invaluable, they are limited and don't always provide as good of results as one would like. The Hartree-Fock method has been applied to systems of interest here; however, it is not able to address cases where electron correlations are more dominant such as those involving transition metals or van der Waals forces. Post Hartree-Fock methods such as DFT have been widely applied to virtually any kind of system you can think of; however, the accuracy of the results is not always clear and often require accurate theories to validate results. The DFT methods allow for a lot of versatility through the use of different functionals that are designed for a specific class of applications. As an example, the Local Density Approximation (LDA) functional is best suited for metallic systems that more closely approximate the electron gas. Even so, it is not always clear how good the results will be. A number of highly accurate methods are also applied such as Configuration Interaction methods and Coupled Cluster Methods. However, these methods are limited in their use to smaller systems due to poor scaling that is at least $\mathcal{O}(N^6)$ and even $\mathcal{O}(N!)$ in the number of electrons N.

The QMC methods that are used here offer some genuine advantages over the methods listed above but fundamentally differ in that they rely on stochastic sampling processes to solve the Schrödinger equation. The Variational and Diffusion Monte Carlo (VMC and DMC) methods allow the investigator to leverage the single-body methods which are generally easier and less expensive to use so that accuracy comparable to CCSD(T) can be obtained, but with $\mathcal{O}(N^3)$ scaling which is suitable for larger systems. However, QMC methods present their own challenges, some of which are common to virtually all methods. For example, measuring small energy differences in QMC can be difficult due to the inherent noise of the sampling process and other factors. Further, in order to reduce noise and cost, effective core potentials (ECP), also referred to as pseudopotentials (PP), can be used. The use of PPs allow atomic core electrons to be replaced by a potential so that the number of electrons and the energy scale of the problem is reduced. However, pseudopotentials are generally only consistent within single-body methods like HF. So it is essential to insure that the ECP is suitable for use in QMC. In addition, the DMC methods used here require a trial wave function. In this work the trial function is derived in part from single-body methods like DFT and thus there is some trial function dependence. This dependence is the result of fixed-node error for fermion systems as will be discussed in Sec. 4.2. The fixed-node error can only be eliminated by knowing the exact ground state wave function nodal surface. Since this is unknown, care must be taken to construct a trial function that results in good cancellation of fixed node error for energy differences. In addition, it is difficult to optimize geometries in DMC and it is often desirable to use geometries derived from other methods, such as DFT. This potential source of error must also be quantified. Even with these challenges, it seems that QMC methods uniquely offer both the high accuracy and scalability necessary to study potentially complicated hydrogen storage systems.

1.4 Systems Studied Here

The main system we have chosen to study is hydrogen on a Ti-ethylene sorbent with as many as 5 hydrogen molecules added. In most of the runs the first molecule chemisorbs resulting in a TiH_2-ethylene adsorbent. This system is selected because it has chemical properties representative of larger transition metal decorated carbon systems.[16] Thus the results obtained here should be more broadly applicable and highly relevant to larger systems. Such carbon and transition metal systems combine the advantages of the high surface areas associated with many carbon systems with the advantageous bonding mechanisms associated with σ-bonding on transition metals that result in adsorption.

In order to demonstrate that our methods are accurate enough for this demanding problem, a substantial amount of work has gone into conducting tests of our QMC methods at each step along the research path. For this reason, the final results presented are not only the numbers pertaining to hydrogen storage energetics, but the systematic body of test results that substantiate the accuracy of the conclusions. This work is composed of five studies where the last study applies QMC methods to hydrogen adsorption on the Ti-ethylene systems.

The first study presented is that of H_2. In this work some very general issues about treating hydrogen are addressed that apply to the work as it moves forward. Some of the ideas of this study serve as a template for other elements that are included later in the research. Second, a study of hydrogen on benzene is presented. That work has already resulted in a publication in the Journal of Chemical Physics.[17] The main purpose of this study, within the context of this thesis research, is to test the quality of our trial wave function and the ability of our methods to resolve even the small energy differences associated with hydrogen physisorption. Third, a study of atomic Ti is presented. Since this work is done with an eye toward even larger systems, we like to use pseudopotentials for the Ti core electrons. This results in a significant savings of computer time and improved statistics. The trial wave functions are tested here as well. Fourth, we treat TiH_2 which is an important building block of the adsorbent systems we finally study. Moreover, the Ti d-states determine the symmetry of the overall molecular state. This results in low lying excited states that are very close in energy. Again, trial functions are compared. A big part of this work involves studying the error due to using PBE-DFT optimal geometries as opposed to DMC optimized geometries. This is done by conducting a full DMC geometry optimization for the ground and two excited states. DMC potential energy surfaces are constructed so that optimal geometries can be statistically estimated. Finally we study hydrogen adsorbed on Ti-ethylene where numerous structures are compared and formation energies calculated. This body of work will allow not just for conclusions about hydrogen storage but of the suitability of the QMC method in this context.

1.5 Thesis Outline

A description of single-body and many-body deterministic methods is given in Chapters 2 and 3. Hartree-Fock (HF) theory and Density Functional Theory (DFT) are discussed along with issues related to basis sets and the corrections associated with basis set superposition error. Further discussion regarding the Configuration Interaction (CI), Coupled Cluster and Møller-Plesset second order perturbation (MP2) theories are also touched upon for reference purposes. These chapters are not designed to be exhaustive studies, but rather to serve as reference points so that the result with which we compare can be put into context.

In Chapter 4, significantly more detail is given regarding the Monte Carlo methods that are used throughout this work. Starting with Monte Carlo integration and importance sampling, discussion is made regarding the standard Variational and Diffusion Monte Carlo (VMC and DMC) algorithms we use as well as the Lattice Regularized DMC (LRDMC) variant. Particular attention is paid to describing the fixed-node and time-step error issues in DMC. Further discussion is made with regard to pseudopotentials, the localization error and the partial remedy put forth by Casula[18] that restores the variational character and partial cancellation of errors for energy differences.

A discussion regarding the correlated trial wave functions that are used in this work is given in Chapter 5. Here we describe the Slater-Jastrow trial function form which is used in the majority of the work. It is shown how additional correlations beyond those of single slater determinants (or even some large determinant expansions) can be included through use of a Jastrow factor. Also, the critical role of the single-body orbitals in defining the nodal surface is explained. In addition, the Jastrow correlated Antisymmetric Geminal Power (JAGP) trial function is also described. This trial function form is ideally suited in describing resonant valence bonds (RVB) in systems like benzene and even correlations of more complicated systems.

Chapter 6 is the first of five studies. Here, methodology and results pertaining to hydrogen are given. These results are not an end in and of themselves but rather illustrate how the choices are made in treating hydrogen and other atoms in more general systems. Discussions regarding basis sets and convergence are also presented along with results for HF, PBE-DFT and DMC.

Hydrogen binding on benzene is presented in Chapter 7. Here comparison is made between the PBE-DFT results using a Slater-Jastrow and JAGP (Geminal) trial function. This work establishes the level of accuracy that can be obtained using DMC methods. Moreover, this study also presents a strong test of the Slater-Jastrow nodal surface in describing this system, comparing it to significantly more correlated trial function. This establishes fixed-node accuracy in energy differences between two significantly different trial functions. This study also seeks to assess the nature of the bonding between hydrogen and benzene.

A study of atomic titanium is given in Chapter 8. Here we test the Ti pseudopotential given by Burkatzki, Filippi and Dolg (BFD).[19] Comparison is made between HF and DFT trial functions and usable Jastrow cutoffs are determined. Comparisons are made for the 1^{st} and 2^{nd} ionization potentials along with the lowest σ-excitation. This study also allowed for the gaining of some initial experience with d-state behavior and experience in obtaining correct angular momentum states when the single body orbitals are real. This study also yields insight into how to go about searching for hard to find states in other systems.

In Chapter 9, findings are provided for a DMC optimization of titanium dihydride ($\mathrm{TiH_2}$). Here attempt is made to study how good PBE optimized geometry is as compared to a DMC optimized geometry. Geometry optimization of DMC is generally quite costly and not typically done. This study quantifies the energy error due to optimization in PBE-DFT theory. Geometry optimization in DMC is conducted by quadratic fit of DMC energy data on a configuration space grid allowing optimal energies and geometries to be calculated to within a statistical accuracy. Trial functions from both HF theory and PBE-DFT are compared for the ground and two excited states of $\mathrm{TiH_2}$. These tests of trial wave function and accuracy for small energy differences are thereby extended to a system that is very similar and an important component of the hydrogen storage systems we finally study.

Chapter 10 presents the main study of this thesis research which is hydrogen adsorption on Ti-ethylene. This system has shown excellent potential to store hydrogen in previous work.[16] Several spin states for each structure are considered so that the ground state in both PBE-DFT and DMC can be confirmed. Comparison is made between PBE-DFT and DMC for all calculations done. Formation energies are also calculated for both ground and excited state transitions. Various aspects of the bonding are also discussed.

This work concludes with a summary of findings. In addition, the suitability of the QMC methods used will also be discussed in some length. Conclusions are also drawn about the Ti-ethylene system as a foundation for practical hydrogen storage. Final thoughts are also given regarding possible future work and also other approaches to this problem that might be relevant.

Chapter 2

Single-Body Methods

Single-body methods offer a cost effective means of getting good results, although not as reliably as many-body methods. Addition, single-body methods can serve as a starting point for higher-level theories. For example, the QMC methods discussed later in Chapter 4 use single-body methods to derive a trial function. In this way these methods are complementary. The descriptions given here are by no means intended to be complete treatments. Rather, because these methods are directly relevant to the present work, it will prove useful to have some basic reference material so that distinctions can be made as discussion moves on to the many-body theories that are the methods of interest.

2.1 Slater Determinant Wave Function

Description of a quantum mechanical wave function with many bodies requires certain properties to be satisfied. For bosonic systems, the wave function must be symmetric under particle exchange while fermion systems must be antisymmetric. Mathematically this means that

$$\Psi(\mathbf{x}_1, \mathbf{x}_2) = \pm\Psi(\mathbf{x}_2, \mathbf{x}_1) \tag{2.1}$$

where Ψ is the wave function, $\mathbf{x}_i$ indicates the coordinate of particle i (it can have spin too), with $+$ and $-$ is for boson and fermion systems respectively. Since this work focuses on molecules and the description of electrons, the fermion form is used. In 1929 Slater observed that an antisymmetric wave function can be constructed from a determinant [20], i.e.

$$\Psi_S(\mathbf{x}_1, \ldots, \mathbf{x}_N) = \frac{1}{\sqrt{N!}} \begin{vmatrix} \chi_{i_1}(\mathbf{x}_1) & \chi_{i_2}(\mathbf{x}_1) & \ldots & \chi_{i_N}(\mathbf{x}_1) \\ \chi_{i_1}(\mathbf{x}_2) & \chi_{i_2}(\mathbf{x}_2) & \ldots & \chi_{i_N}(\mathbf{x}_2) \\ \vdots & \vdots & & \vdots \\ \chi_{i_1}(\mathbf{x}_N) & \chi_{i_2}(\mathbf{x}_N) & \ldots & \chi_{i_N}(\mathbf{x}_N) \end{vmatrix} \tag{2.2}$$

where each $\chi_i(\mathbf{x})$ is a spin orbital. Particle exchange is equivalent to a transposition of rows which changes the sign of the wave function. Since there are no spin orbit interactions it turns out that Eqn. (2.2) can effectively be simplified by factoring it into spin up and spin down parts as

$$\Psi_S(\mathbf{x}_1,\ldots,\mathbf{x}_N) \cong \frac{1}{\sqrt{N^{\uparrow}!N^{\downarrow}!}} \begin{vmatrix} \varphi_{i_1}(\mathbf{r}_1) & \cdots & \varphi_{i_{N^{\uparrow}}}(\mathbf{r}_1) \\ \vdots & \ddots & \vdots \\ \varphi_{i_1}(\mathbf{r}_{N^{\uparrow}}) & \cdots & \varphi_{i_{N^{\uparrow}}}(\mathbf{r}_{N^{\uparrow}}) \end{vmatrix}^{\uparrow} \times \begin{vmatrix} \varphi_{i_{N^{\uparrow}+1}}(\mathbf{r}_{N^{\uparrow}+1}) & \cdots & \varphi_{i_N}(\mathbf{r}_{N^{\uparrow}+1}) \\ \vdots & \ddots & \vdots \\ \varphi_{i_{N^{\uparrow}+1}}(\mathbf{r}_N) & \cdots & \varphi_{i_N}(\mathbf{r}_N) \end{vmatrix}^{\downarrow} \tag{2.3}$$

where each $\varphi_i(\mathbf{r})$ is a single-body space orbital, indices i_1 - $i_{N^{\uparrow}}$ are for spin up, and $i_{N^{\uparrow}+1}$ - i_N are for spin down. While the factored form in Eqn. (2.2) and the standard form in Eqn. (2.3) are not equal, they are equivalent in the sense that all observable expectation values are the same. Finally, it should be clarified that Eqn. 2.2 above is a single-body description because wave function is in effect completely defined by the single body orbitals. This description has certain limitations that will be expounded upon later in the Chapter 5 on correlated wave functions.

Hartree-Fock (HF) theory [21, 22] seeks the best variational solution to the Schrödinger equation where the solution is restricted to a single Slater determinant (2.5). The electronic part of the standard many-body Hamiltonian is given by

$$\hat{H} = -\sum_i \frac{1}{2}\nabla_i^2 + \sum_i V_{ext}(\mathbf{r}_i) + \sum_{i\neq j} \frac{1}{|\mathbf{r}_i - \mathbf{r}_j|} \tag{2.4}$$

where $V_{ext}(\mathbf{r}) = -\sum_I \frac{Z_I}{|\mathbf{r}-\mathbf{R}_I|}$ and Z_I is the charge of nuclear center I. Restricting solutions to those representable as a single Slater determinant gives rise to a integro-differential system of equations that lead to an effective single-body Hamiltonian involving a mean field (the sum of the potentials). This system of equations, referred to as the Fock operators, can be written as

$$H^{\sigma}_{eff} = -\frac{1}{2}\nabla^2 + V_{ext}(\mathbf{r}) + V_{Hartree}(\mathbf{r}) + \hat{V}^{\sigma}_x, \tag{2.5}$$

where $V_{Hartree}(\mathbf{r})$ is the average Coulomb potentials due to the electrons and $\hat{V}^{\sigma}_x$ is the exchange operator that acts differently on each orbital.

By choosing a basis for the spin and spatial orbitals, equation (2.5) further simplify to one of the forms of the Roothaan equations. Choosing specific basis sets, e.g. Gaussians or plane-waves, can result in further gains in computational efficiency.

Hartree-Fock serves as a starting point for higher-level many body theories and perturbation theory. In addition HF also serves as a reference point for the correlation energy. The HF solution is uncorrelated and so is defined to have zero correlation energy. Certainly less restrictive wave function forms will result in a lower variational energy, where the energy difference is defined as the correlation energy.

2.2 Density Functional Theory

Density functional theory (DFT) is based on theorems put forth by Hohenberg and Kohn in 1964 [23] and the ansatz of Kohn and Sham in 1965 [24]. The Hohenberg-Kohn theorems state that the ground state particle density uniquely defines the external potential (e.g. coulomb potential from the atomic nuclei) and that, for a given external potential, there exists a universal energy functional valid on the set of V-representable density functions. The power of the Hohenberg-Kohn theorems is to reduce the problem of finding a many-body wave function to one of finding an electron density that is a function of position only. The Kohn-Sham ansatz is an assumption that there is a mapping from the many-body problem to some single-body (non-interacting) problem. The single-body solutions have no physical meaning other than to provide contributions to the density. While there is no proof for this ansatz, it has been shown to work well in many cases.

The density functional formalism [25, 26] results in an auxiliary single-body Hamiltonian given by

$$H^{\sigma}_{aux} = -\frac{1}{2}\bigtriangledown^2 + V_{ext}(\mathbf{r}) + V_{Hartree}(\mathbf{r}) + V^{\sigma}_{xc}(\mathbf{r}) \tag{2.6}$$

which has the same form as the HF Hamiltonian except that the $\hat{V}^{\sigma}_{x}$ term is now $V^{\sigma}_{xc}(\mathbf{r}) = \delta E_{xc}[n(\mathbf{r},\sigma)]/\delta n(\mathbf{r},\sigma)$ which is a local exchange-correlation potential where E_{xc} is the exchange-correlation energy functional. This leads to a set of self-consistent differential equations that are simpler than the HF equations. Unfortunately the exact E_{xc} functional is not known and there is no known way to systematically generate an approximation that approaches the exact limit. For this reason approximations are made. Among the most widely used of these is the local density approximation (LDA) and the generalized gradient approximation (GGA).

The local density approximation (LDA) essentially is designed to reproduce the behavior for the electron gas and has an exchange-correlation energy functional of the form

$$E_{xc}[n(\mathbf{r})] = \int d\mathbf{r} n(\mathbf{r}) \epsilon^{LDA}_{xc}(n(\mathbf{r})). \tag{2.7}$$

Where ϵ_{xc} is the sum of exchange and correlation functions for the LDA. Here local exchange energy is given analytically by the Dirac exchange energy function [27] and correlation energy computed by Monte Carlo methods in 1980 by Ceperley and Alder [28]. As such, this approximation produces exact results for the electron gas and generally good results for systems where the electron density varies slowly such as periodic metal systems. On the other hand, many systems, such as surfaces or molecules, produce more rapidly varying electron densities that are problematic for LDA because it does not incorporate known density gradient corrections. In practice, LDA is known to overbind and give too short of bond lengths.

The Perdew, Burke, and Enzerhof (PBE) functional [29, 30] based on the generalized gradient approximation (GGA) is used here throughout except possibly where other functionals were tried, e.g. the hybrid B3LYP [31, 32, 33], for comparison purposes. The main idea of the PBE-GGA is to use an exchange-correlation energy functional of the form

$$E_{xc}[n_\uparrow, n_\downarrow] = \int d\mathbf{r} f(n_\uparrow, n_\downarrow, \bigtriangledown n_\uparrow, \bigtriangledown n_\downarrow). \tag{2.8}$$

which can account for both spin density and gradients. The correlation functional exactly satisfies the slow varying and rapidly varying density limits and the high density limits. The exchange energy functional in addition satisfies uniform coordinate scaling, spin scaling, unpolarized uniform electron gas linear response, and the Lieb-Oxford bound. In practice, the GGA results in a marked improvement in total energies, atomization energies, energy barriers and structural energy differences over LDA. Practically speaking, the GGA corrects the overbinding of LDA (although sometimes this is an overcorrection). Nonetheless, the success of the GGA in accurately describing inhomogeneous systems such as molecules has resulted in widespread adoption of DFT methods and the chemistry community and also motivates this author regarding its use in the present work on molecular systems.

Finally it should be noted that while the single-body orbitals in DFT have no formal meaning, they can be used to construct a trial wave function in the form of a Slater determinant. This is reasonable when one considers the similarity between Eqns. 2.6 and 2.5 and that the resulting trial function has the DFT electron density. While it is rigorously true that a DFT derived Slater determinant does not have an expectation energy that is lower than the HF solution, such a statement does not apply to correlated Slater-Jastrow wave functions as will be discussed later in Chapter 5.

2.3 Basis Set Issues

Both HF and DFT, as mentioned above, require that the solutions be cast in some basis. While there are a variety of choices, for molecular systems, the most efficient functions are localized atom-centered orbitals. This is in contrast to periodic systems where a plane-wave description has obvious value. Atomic centered orbitals are typically constructed in terms of Gaussian functions for computational efficiency since multiplying and integrating Gaussians can be done analytically. There are certain deficiencies to Gaussians, however, that deserve discussion.

The wave function description of a molecule requires cusp conditions to be satisfied as electrons approach atomic centers. This is generally not a problem in single-body methods because those cusp regions represent a small portion of configuration space that can be integrated over. This is more of a concern for quantum Monte Carlo calculations as will be discussed later in Chapter 4. This problem cannot be fully addressed with more complete basis sets because Gaussians always have a gradient of zero about the origin.

Another problem is basis set superposition error (BSSE). As two non-overlapping molecules approach one another the basis functions centered on each of the molecules start to complement the other molecules description so that the basis becomes more complete than when they are separated. This results in an artificial deepening of binding wells because this error is always negative. The counterpoise correction developed by Boys and Bernadi [34] is used to correct for this. Here the energy of a dimer AB is corrected by subtracting off the energy by which the constituent monomers A and B are *lowered* by adding the basis functions associated with the other monomer. The counterpoise corrected energy can be written as

$$E_{AB}^{CP} = E_{AB} - (E_{A(B)} - E_A) - (E_{B(A)} - E_B) \tag{2.9}$$

and the basis set superposition error can be written as

$$\mathrm{BSSE} = (E_{A(B)} - E_A) + (E_{B(A)} - E_B). \tag{2.10}$$

In practice this becomes more difficult as the individual basis sets themselves become more complete, e.g quadruple-zeta or 5-zeta. Basis set over-completeness can result in convergence difficulties in the self-consistent energies which can sometimes be challenging even without calculating the correction. It should be noted that this error can become significant especially when binding is weak.[35]

Chapter 3

Deterministic Many-Body Methods

This work does not focus on methods such as Configuration Interaction, Coupled Cluster or Møller-Plesset Second Order Perturbation Theory, however, comparisons are made against these theories to test and qualify our results. For this reason it is important to have an idea of what these theories are along with their strengths and weaknesses. There will be no attempt to develop a complete treatment of these theories, rather only sketches will be given that really should only serve as a convenient starting point for reference purposes. Possibly the most important point to be made about these various theories is in regards to computational scaling. In practice, the Coupled Cluster method (CCSD(T)) has an accuracy most comparable to the quantum Monte Carlo (QMC) methods that will be discussed in the next chapter. It turns out that QMC methods scale roughly as $\mathcal{O}(N^3)$ where as CCSD(T) scales as $\mathcal{O}(N^7)$, a huge difference, giving QMC methods a significant advantage for larger systems.

3.1 Configuration Interaction

Configuration interaction (CI) [22] is a method that expands a correlated wave function in Slater determinants constructed from single-body orbitals derived from theories such as HF. Single-body excitation terms are simply the HF solution where one of the orbitals is replaced by higher orbital. In like manner, one can construct two-body, three-body, ..., and n-body excitations. To find the coefficients, one simply sets up the space restricted Schrödinger equation $H_{CI}\psi_i = E_i\psi_i$. Here the wave function is defined in terms of excitations as

$$\Phi_0 = c_0 \left|\psi_0\right\rangle + \sum_{ar} c_a^r \left|\psi_a^r\right\rangle + \sum_{abrs} c_{ab}^{rs} \left|\psi_{ab}^{rs}\right\rangle + \sum_{abcrst} c_{abc}^{rst} \left|\psi_{abc}^{rst}\right\rangle + \dots \tag{3.1}$$

The problem with full CI is that even for relatively small systems the size of H becomes unmanageable due to approximately $\mathcal{O}(N_{det}N^4)$ (implying exponential or factorial) scaling where N is the number of orbitals and N_{det} is the number of determinants.[36] This restricts its application to small systems with small basis sets. However, the full CI yields the lowest possible variational energy for a given basis set. In order to get around the very high cost of a full CI calculation, the CI expansion is truncated so that only certain excitations are included. For example, the truncated CI expansion containing all single and double excitations is known as singles doubles CI (SDCI). While this approximation brings the scaling into the polynomial realm the solutions are no longer *size consistent.*[37] For typical cases, SDCI scales as $\mathcal{O}(N^6)$ and SDTQCI scales as $\mathcal{O}(N^{10})$. Among the many benefits of CI is the ability to get excited states.

3.2 Coupled Cluster Methods

The coupled cluster approximation [22, 37] seeks to describe higher excitations in terms of lower ones. This method has its roots in nuclear physics and has proven to be a very powerful tool for chemistry.[38] This is done by assuming that the quadruples are related to the doubles by $c_{ijkl}^{rstu} \approx c_{ij}^{rs} c_{kl}^{tu}$ plus all permutations. It turns out that this approximation, when extended to hex-tuples etc., can approximate all the even excitations of the full CI expansion. If single excitations are added, one has the coupled cluster singles doubles (CCSD) approximation with $\mathcal{O}(N^6)$ scaling. Additionally, triples are added by way of perturbation theory (CCSD(T)) resulting in a very accurate method with $\mathcal{O}(N^7)$ scaling that has been referred to as the "gold-standard".[39] This method is size consistent and invariant to unitary transformation of degenerate states and provides a good tradeoff between cost and accuracy for smaller systems. A drawback is that the method is not variational.

3.3 Møller-Plesset Second Order Perturbation Theory

Møller-Plesset second order perturbation theory (MP2) [22, 40] actually follows a formalism identical to general perturbation theory with only one stipulation: the unperturbed Hamiltonian $H_0 = \sum_i H_{eff}(\mathbf{r}_i)$ is the HF Hamiltonian and is the sum over the single-body Fock operators as described in Section 2.5. Thus the correlation energy to second order is

$$E_0^{(2)} = \sum_{abrs} \frac{| < \psi_0 | \sum_{i<j} r_{ij}^{-1} | \psi_{ab}^{rs} > |^2}{\varepsilon_a + \varepsilon_b - \varepsilon_r - \varepsilon_s}. \tag{3.2}$$

Here the sum is over the double excited states, ψ_0 is the HF ground state, and ε_i is the eigenvalue of the ith HF orbital. This method is size consistent, extendable to higher orders (although not often greatly advantageous), and computationally inexpensive (once the HF calculations are done) and result in a scaling that goes as $\mathcal{O}(N^7)$. Note that MP2, like Coupled Cluster, is not variational.[41]

Chapter 4

Monte Carlo Many-Body Methods

Monte Carlo (MC) methods are based on stochastic rather than deterministic processes. These methods were pioneered by McMillan [42] in 1965 for bosonic systems and by Ceperley, Chester, and Kalos [43] in 1977 for fermions. As a result of favorable $\mathcal{O}(N^3)$ scaling, they are the only methods known that can treat large numbers of interacting particles. The reason for this lies in the fact that MC integration scaling is itself independent of integrand dimensionality.[44] Additionally, MC methods are easy to parallelize and allow wave function forms that would otherwise be prohibitive. As a result the restriction to Gaussian or plane-wave basis sets is lifted. While these functional forms have convenient properties, they can be expensive to evaluate. The methods used here allow for function transformations that can result in further speed increases as, for example, by transforming a Gaussian contraction to a B-spline form.

Two zero-temperature methods will be discussed, Variational Monte Carlo (VMC) and Diffusion Monte Carlo (DMC) along with the Lattice Regularized extension of DMC (LRDMC).[45] Next pseudopotentials will be discussed, explaining their role and means of implementation in DMC. Additionally, a recently developed method that restores the variational character of DMC normally broken by the localization approximation will be outlined. Finally, details will be given regarding the B-spline transformations used in many of the calculations done in this work.

4.1 Variational Monte Carlo

Variational Monte Carlo (VMC) is based on the variational principle in quantum mechanics combined with Monte Carlo integration. The variation principle is essentially true by definition and states that

$$E_g \leq \langle \psi_T | H | \psi_T \rangle \tag{4.1}$$

where ψ_T is a trial wave function and E_g is the ground state energy. Employing the variational principle should not be surprising since it the premise of many methods, among them being HF and CI. The main challenge of this method is the necessity of supplying ψ_T. Combining VMC with a good correlated trial wave function (Chapter 5) along with optimization methods suitable for stochastic processes results in a very powerful method that often leads to accurate estimates of ground state and excited state energies. In addition, the resultant analytic wave functions can be valuable for other purposes and give physical insight.

Monte Carlo integration is a method of estimating an integral by random sampling. Consider a function $f(x)$ on the interval $[0, 1]$. Further suppose that one has a Markov chain of n numbers $\{x_1, x_2, ..., x_n\}$ uniformly distributed on this interval. Then in the limit of large n,

$$\int_0^1 dx f(x) \approx \frac{1}{n}\sum_{i=1}^{n} f(x_i) \pm \frac{\sigma_f}{\sqrt{n}}. \tag{4.2}$$

Here, n must be large enough so that the central limit theorem holds. The error in Eqn. 4.2 is the standard deviation and equals $\sigma_f/\sqrt{n}$ where σ_f is the standard deviation of $f(x)$ on the interval $[0, 1]$. The key point is that the above result holds even when x is some high dimensional vector $\mathbf{x}$. This is in contrast to quadrature integration scaling which goes as $n^{-k/d}$, where k is some positive integer and d is the dimension of the problem.

Importance sampling schemes have been devised to make VMC more efficient. Importance sampling seeks to focus sampling on the important regions of space (e.g. where the wave function is predominantly non-zero). Suppose one wants to integrate $f(\mathbf{x})$ over all space. Further, suppose one knows of a non-negative (*weight*) function $w(\mathbf{x}) \overset{\sim}{\propto} |f(\mathbf{x})|$ whose integral over all space is 1. Then, given a Markov chain $\{\mathbf{x}_1, \mathbf{x}_2, ..., \mathbf{x}_n\}$ distributed according to $w(\mathbf{x})$, one can compute the integration as

$$\int dx\, f(\mathbf{x}) = \int dx\, w(\mathbf{x})\, \frac{f(\mathbf{x})}{w(\mathbf{x})} \approx \frac{1}{n}\sum_{i=1}^{n} \frac{f(\mathbf{x}_i)}{w(\mathbf{x}_i)} \pm \frac{\sigma_{f/w}}{\sqrt{n}}. \tag{4.3}$$

This transformation serves to improve scaling by a factor of $\sigma_f/\sigma_{f/w}$ as well as allow for integration over all space. Recasting VMC with importance sampling gives

$$E_{VMC} \equiv \int d\mathbf{x}\, |\psi(\mathbf{x})|^2\, E_L(\mathbf{x}) \approx \frac{1}{n}\sum_{i=1}^{n} E_L(\mathbf{x_i}) \pm \frac{\sigma_{E_L}}{\sqrt{n}}. \tag{4.4}$$

where $E_L(\mathbf{x}) \equiv \psi^{-1}(\mathbf{x}) H \psi(\mathbf{x})$ is the local energy. At this point, all that's needed are electron configurations distributed according to the many-body density $|\psi(\mathbf{x})|^2$.

The Metropolis algorithm, due to Metropolis et al. [46], generates a random-walk with probability distribution matching a given weight function $w(\mathbf{X})$. One starts with a configuration of electrons $\mathbf{X}$ and generates a trial configuration $\mathbf{X}_T$ according to some transition probability $T(\mathbf{X} \to \mathbf{X}_T)$ where $T(\mathbf{X} \to \mathbf{X}_T) = T(\mathbf{X_T} \to \mathbf{X})$ (generalized Metropolis relaxes this constraint

[45]). The trial configuration is accepted with probability

$$\min\left\{\frac{w(\mathbf{X}_T)}{w(\mathbf{X})}, 1\right\}. \tag{4.5}$$

If accepted, $\mathbf{X}_T$ becomes the next step of the random walk, otherwise $\mathbf{X}$ is. This algorithm has been improved upon by using a generalized Metropolis algorithm along with the Fokker-Planck formalism so that the diffusion is built into the transition probability T above.

Correlated Sampling [45] is a method by which energy differences, or the difference in some other expectation value, can be estimated while at the same time reducing uncertainty. Consider two wave functions Ψ_1 and Ψ_2. Construct a guiding function $\Pi = |\Psi_1|^2 + |\Psi_2|^2$ and weights $w_{ij} = \Psi_i^*\Psi_j^*/\Pi$. Then the energy difference between states 1 and 2 is given by

$$\Delta E_{12} = \frac{\int d\mathbf{X}|\Psi_1(\mathbf{X})|^2 E_L^1(\mathbf{X})}{\int d\mathbf{X}|\Psi_1(\mathbf{X})|^2} - \frac{\int d\mathbf{X}|\Psi_2(\mathbf{X})|^2 E_L^2(\mathbf{X})}{\int d\mathbf{X}|\Psi_2(\mathbf{X})|^2} = \frac{\langle w_{11}E_L^1\rangle}{\langle w_{11}\rangle} - \frac{\langle w_{22}E_L^2\rangle}{\langle w_{22}\rangle} \tag{4.6}$$

where the averages $\langle\cdots\rangle$ are weighted according to the guiding function Π and E_L^i is the local energy of Ψ_i. When $\Psi_1 \simeq \Psi_2$ then $w_{11} \simeq w_{22} \simeq \frac{1}{2}$ (away from nodes) and the statistics is correlated so that Eqn. (4.6) resembles $\Delta E_{12} = \langle E_L^1 - E_L^2\rangle$ thus reducing the uncertainty. However, if Ψ_1 and Ψ_2 are significantly different the statistics are uncorrelated and Eqn. (4.6) resembles $\Delta E_{12} = \langle E_L^1\rangle - \langle E_L^2\rangle$. Correlated sampling is particularly important for optimization calculations. Consider calculating an energy derivative with respect to some optimizable parameter α (e.g. a Jastrow coefficient). In finite difference form, the derivative is calculated $\Delta E/\Delta\alpha$. However, the uncertainty $\sigma(\Delta E)$ *does not* approach 0 as $\Delta\alpha \to 0$ for an uncorrelated energy difference. Using a correlated energy difference, $\sigma(\Delta E) \to 0$ as $\Delta\alpha \to 0$ because $\Delta\Psi \to 0$ as $\Delta\alpha \to 0$. Thus correlated sampling allows accurate derivatives of energy (or any observable) to be calculated.

4.2 Diffusion Monte Carlo

Diffusion Monte Carlo (DMC) is a stochastic method that evolves the imaginary time ($\tau = \imath t$) Schrödinger equation such that the ground state is projected out of a trial wave function ψ_T such that

$$\psi_g \propto \lim_{\tau\to\infty} e^{-(\hat{H}-E_g)\tau}\psi_T = \lim_{\tau\to\infty}\sum_i e^{-(E_i-E_g)\tau}c_i\psi_i. \tag{4.7}$$

Here $\hat{H}$ is the Hamiltonian, E_g is the ground state energy and the trial wave function $\psi_T = \sum_i c_i\psi_i$ is expanded in the basis of eigenstates ψ_i and is not orthogonal to the ground state. Unfortunately, because $\hat{H} = \hat{T}+\hat{V}$ and $[\hat{T},\hat{V}] \neq 0$ the exact Green's function for $e^{-(\hat{H}-E_g)\tau}$ is not known. An approximate

Green's function can be constructed by using the Trotter-Suzuki formula for the exponentiation of a sum of operators

$$e^{-\tau(\hat{A}+\hat{B})} = e^{-\tau\hat{B}/2}e^{-\tau\hat{A}}e^{-\tau\hat{B}/2} + \mathcal{O}(\tau^3). \tag{4.8}$$

This results in an approximate Green's function that is exact in the limit as $\tau \to 0$ but results in a *time step error* for finite τ that must be quantified. However, due to antisymmetry in systems containing more than two fermions, ψ will take on both positive and negative values that result in an exponential increase in statistical noise near nodal surfaces. Also, additional problems arise due to Coulomb potential singularities. These problems can be alleviated by doing an importance sampling transformation where the *mixed estimator*

$$f \equiv \psi_T \psi \tag{4.9}$$

is evolved in imaginary time according to

$$-\partial_\tau f(\mathbf{R},\tau) = -\frac{1}{2}\bigtriangledown^2 f(\mathbf{R},\tau) + \bigtriangledown \cdot [\mathbf{v}_D(\mathbf{R}) f(\mathbf{R},\tau)] + [E_L(\mathbf{R}) - E_T] f(\mathbf{R},\tau). \tag{4.10}$$

Here, $\mathbf{v}_D(\mathbf{R}) = \bigtriangledown \ln|\psi_T(\mathbf{R})|$ is the drift velocity and E_L is the local energy as defined in Eqn. (4.4). To make f non-negative everywhere an additional boundary condition, $\mathrm{sign}(\psi) = \mathrm{sign}(\psi_T)$, is implemented. This is the *fixed-node approximation* that results in a *fixed-node error* that is trial function dependent. Finally, the Coulomb potential singularities necessitate the local energy cusp conditions be satisfied in the trial function. The detailed cusp conditions will be discussed later in Chapter 5 when correlated wave functions are discussed in detail.

The first two terms on the left hand side of Eqn. (4.10) represent diffusion and drift respectively. These can be implemented by way of a Langevin equation. The last term in Eqn. 4.10 is a branching term. The number of walkers evolving from $\mathbf{R}$ to $\mathbf{R}'$ is given by $\lfloor P + \eta \rfloor$ where $P = \exp(-\tau[E_L(\mathbf{R}) + E_L(\mathbf{R}') - 2E_T]/2)$ and η is a random number between 0 and 1. It immediately follows that E_T can be used to control the overall walker population. The ground state energy can be estimated as

$$E_{DMC} = \lim_{\tau\to\infty} \frac{\langle e^{-\tau H/2}\psi_T|H|e^{-\tau H/2}\psi_T\rangle}{\langle e^{-\tau H/2}\psi_T|e^{-\tau H/2}\psi_T\rangle} = \frac{\langle\psi|H|\psi_T\rangle}{\langle\psi|\psi_T\rangle} \approx \frac{1}{n}\sum_{i=1}^{n} E_L(\mathbf{R}_i). \tag{4.11}$$

Here a distribution of n walkers has been assumed. Expectation values of observables that don't commute with the Hamiltonian can be calculated by a combination of VMC and mixed DMC estimators.[44]

With Monte Carlo integration, the more accurate the calculation the more it costs. However, time-step errors often necessitate a time-step τ that is smaller than the autocorrelation time t_{ac} in the sample. This results in a rescaling of the number of samples to account for the autocorrelation length $n_{ac} = t_{\mathrm{ac}}/\tau$ in the samples so that the error Δ in the expectation is given by

$$\Delta = \sigma\sqrt{\frac{n_{ac}}{n}} \tag{4.12}$$

Clearly the cost of a calculation is proportional to number of samples n given by

$$n = \frac{t_{\mathrm{ac}}\sigma^2}{\tau\Delta^2}. \tag{4.13}$$

This allows one to see the relationships that often need to be considered when setting up runs. The cost is proportional to the variance σ^2, and inversely proportional to the square of the desired accuracy (Δ^2). In addition, when the time-step is so small that the autocorrelation length is less than 1, the cost is also inversely proportional to the time-step (a useful relationship with conducting convergence studies).

4.3 Lattice regularized diffusion Monte Carlo (LRDMC)

The lattice regularized form of DMC (LRDMC) samples on two incommensurate grids so that sampling density can vary depending on the level of wave function detail. The usual DMC Trotter breakup results in a time-step error while the LRDMC paradigm results in a space step-error, but both share the same upper bound property in the zero-time-step/zero-lattice-space limit and converge to the same projected fixed-node (FN) energy.[18]

In the LRDMC approach, the kinetic energy operator T is replaced by a discretized kinetic energy operator T^a. T^a is a linear combination of two discrete operators with incommensurate lattice spaces a and a' ($a' = \nu a$, with ν an irrational number > 1), namely

$$T^a = -\frac{\eta}{2}(\Delta^{a,p} + \Delta^{a',1-p}), \tag{4.14}$$

where $\Delta^{a,p}$ is the discretized Laplacian with mesh a and weighting function p (see Refs. [47] and [48]), and $\eta = 1 + \mu a^2$ is a prefactor with the parameter μ tunable to improve the efficiency of the diffusion process. Working with two incommensurate meshes helps to sample densely the continuous space by performing discrete moves of length a and a'. The finest hop samples are more likely in regions near atomic centers while the coarser hop samples more often occur in valence regions, the result being an efficient sampling of the overall configuration space. The difference between the continuous and discretized local kinetic energies is added to the potential $V(\mathbf{R})$, resulting in a mesh dependent potential

$$V^a(\mathbf{R}) = V(\mathbf{R}) + \left[\frac{(T - T^a)\Psi_T}{\Psi_T}\right](\mathbf{R}). \tag{4.15}$$

The consequence is a faster convergence of the energies in the $a \rightarrow 0$ extrapolation. In spite of the discretization of T in Eqn. 4.14 and the redefinition of V in Eqn. 4.15, the LRDMC method is equivalent to the continuous space FN DMC. Indeed, in the limit of small mesh sizes a and a', the discretized Hamiltonian H^a approaches the continuous H.

4.4 Pseudopotentials

Pseudopotentials reproduce the combined effects of inert core electrons and the nucleus. They not only reduces the number of particles in a simulation, they smooth the wave function so that larger time steps can be used. These factors work together to allow $\mathcal{O}(N^3)$ scaling in the number of electrons to be realized.[44] There are costs to using pseudopotentials. Pseudopotentials assume a frozen core and as such don't account for the interplay between the core and valence electrons. This approximation becomes problematic when the core is large and there are only one or two valence electrons (it should be noted that core-polarization potentials are designed to address this issue). Additionally, some pseudopotentials are non-local and not truly compatible with the standard DMC implementation so that additional approximations are required to localize the pseudopotential.

The norm conserving pseudopotentials (NCPP) used in this work are constructed according to the description given by Hammenn, Schluter, and Chiang [49] so that the pseudo valence wave function has properties that match the all-electron valence wave function for a reference *ab initio* DFT calculation. Specifically, the following pseudo- and all-electron wave function quantities must match: the valence wave functions beyond some radius R_c, the eigenvalues, the logarithmic derivatives at R_c, and the integrated charge inside R_c (orbital by orbital). With these criteria satisfied, Hammenn, Schluter, and Chiang have shown that the energy derivatives of the dimensionless logarithmic derivative,

$$\frac{\partial^2}{\partial \varepsilon \partial r} \ln \psi_l(\varepsilon, r), \tag{4.16}$$

evaluated at R_c also match. This implies that the pseudo- and all-electron valence wave functions respond similarly to first order, an important property that suggests these pseudopotentials are transferable to other (e.g. molecular) systems. The cutoff R_c is chosen to be as large as possible (soft) for smoothness while being small enough so that bonds are accurately described. The general form of the pseudopotential $\hat{V}_{nl}$ is given by

$$\hat{V}_{nl} = \sum_i \hat{V}_{nl,i} \quad \text{where} \quad \hat{V}_{nl,i} f(\mathbf{r}_i) = \sum_{l,m} V_{nl,l}(\mathbf{r}_i) Y_{lm}(\mathbf{\Omega}_i) \int_{4\pi} Y^*_{lm}(\mathbf{\Omega}'_i) f(\mathbf{r}'_i) d\mathbf{\Omega}'_i \tag{4.17}$$

and is non-local since the radial part varies with angular momentum.

The localization approximation is used in DMC because non-local pseudopotentials in effect create another sign error (similar to the sign error that leads to the fixed node approximation). When non-local pseudopotentials are used the MC diffusion equation (4.10) becomes

$$-\partial_\tau f = -\frac{1}{2}\nabla^2 f + \nabla \cdot [\mathbf{v}_D(\mathbf{R}) f] + [E_L(\mathbf{R}) - E_T] f - \left\{ \frac{\hat{V}_{nl}\psi_T}{\psi_T} - \frac{\hat{V}_{nl}\psi}{\psi} \right\} f. \tag{4.18}$$

The problem arises in the last term of (4.18). It is essential to have a very good trial wave function so that $\psi_T \simeq \psi$, the last term in (4.18) can be taken to be negligible. A consequence of the approximation is that the solution is no longer variational.

A variational upper bound DMC scheme for non-local pseudopotentials has been recently devised by Casula in 2006.[18] This scheme is a sort of fixed node approximation for the non-local part of the Hamiltonian that addresses some of the major short comings of the standard localization approximation. In contrast, this method provides a variational upper bound of the true non-local Hamiltonian. Additionally, DMC stability is improved due to a softening of the most attractive parts of the non-local potential. While this method still results in a localization error, there is now a strict partial cancellation of this error in energy differences, an important property.

This method is compatible with both the standard DMC and LRDMC implementations. In contrast to the localization approximation, a breakup[47, 18] of the non-local potential localizes the positive matrix elements into the branching term while treating the negative matrix elements as a non-local diffusion operator sampled via a *heat bath* scheme.[18] The positive and negative terms are defined by

$$V^{\pm}_{\mathbf{R}',\mathbf{R}} = 1/2(V_{\mathbf{R}',\mathbf{R}} \pm |V_{\mathbf{R}',\mathbf{R}}|) \tag{4.19}$$

where

$$V_{\mathbf{R}',\mathbf{R}} = \frac{\Psi_T(\mathbf{R}')}{\Psi_T(\mathbf{R})} \langle \mathbf{R}' | V_{\text{non-local}} | \mathbf{R} \rangle , \tag{4.20}$$

and $\mathbf{R}$, $\mathbf{R}'$ are all-electron configurations on a quadrature mesh with one electron rotated around a pseudo ion.[50] The breakup corresponds to an effective Hamiltonian H^{eff}, defined as

$$\begin{aligned} H^{\text{eff}}_{\mathbf{R},\mathbf{R}} &= K + V^{\text{eff}}(\mathbf{R}) && (4.21) \\ H^{\text{eff}}_{\mathbf{R}',\mathbf{R}} &= \langle \mathbf{R}' | V_{\text{non-local}} | \mathbf{R} \rangle \qquad \text{if } V_{\mathbf{R}',\mathbf{R}} < 0, \end{aligned}$$

with the modified local potential $V^{\text{eff}}(\mathbf{R}) = V_{\text{loc}}(\mathbf{R}) + \sum_{\mathbf{R}'} V^{+}_{\mathbf{R}',\mathbf{R}}$ that includes the *sign flip* terms. The FN ground state energy of the Hamiltonian in Eqn. 4.21 is a variational upper bound of the original non-local Hamiltonian.[51] Furthermore, DMC stability is improved substantially compared to the local approximation, where the most attractive parts of the localized pseudopotential can result in a walker population "blow up". Moving the negative part of the localization into a diffusion-like term causes the walkers to be driven away from such regions.

4.5 B-spline Grid Transformations

As mentioned in the introduction of this chapter, QMC methods are not married to a particular basis set or wave function form. Evaluating the single-body orbitals and/or derivatives is certainly where the main cost in calculations arises. For example, it turns out that Gaussian contractions can be very expensive to evaluate all by themselves. Transforming Gaussian contractions into a B-spline grid form results in significant increases in speed. Recently the einspline C library for the creation and evaluation of interpolating cubic B-splines (basis splines) has been developed by Kenneth Esler [52] for general use and also for specific use in the QMCPACK computer code by Jeongnim Kim et al. [53] which has been used for all the standard DMC calculations done in this work.

The cubic B-spline transformations done for the present calculations are on a uniform grid. Namely 3^{rd} order polynomials are fit piecewise on a uniformly partitioned grid so that the resulting function is continuous, continuous on its 1^{st} and 2^{nd} derivatives, and piecewise continuous on its 3^{rd} derivative. This allows for a very versatile basis that can efficiently describe Gaussian contractions. Using B-splines, the Gaussian contractions need only be evaluated on the grid once at the beginning of the calculation. Afterward the main calculation, which typically requires millions of function evaluations, proceeds using the more efficient cubic polynomials instead.

In addition to transforming other functional forms, B-splines are useful in their own right. As will be mentioned in Chapter 5, B-splines in conjunction with stochastic optimization techniques can be used to describe Jastrow factors where the functional form is not obvious from the outset.

Chapter 5

Correlated Wave Functions

Throughout this work, two types of correlated trial wave functions are used, the Slater-Jastrow (SJ) and the Jastrow correlated Antisymmetric Geminal Power (JAGP). These wave function forms are a departure from the Slater determinant used in HF theory and the determinant expansions used in CI and related theories. The reason a simple Slater determinant is not desirable for this work is because it results in a wave function that fundamentally lacks electron correlations. This is problematic for QMC methods because electron-electron correlations can be directly accounted for in both VMC and DMC. On the other hand, multi-determinant expansions have also been avoided. This function form can give a proper correlated wave function, however, it is expensive. The trial functions used here are designed to be computationally less demanding like the Slater determinant while providing for electron correlations somewhat similar to multi-determinant expansions. Below I start with a general explanation regarding Jastrow-Determinant form with some discussion specifically regarding the Slater-Jastrow form. Next cusp conditions are explained. Finally the JAGP will be discussed along with its relevance to describing the resonating valence bonds (RVB) like those in benzene which is a system that is studied as a part of this thesis research.

5.1 The Jastrow Factor

The Monte Carlo methods used here work most efficiently when correlated trial wave functions that reasonably approximate the ground state are used. One of the most straightforward ways to introduce correlation is to start with an antisymmetric wave function (e.g. a Slater determinant) and multiply it by a Jastrow factor. The N-electron wave function can then be expressed as

$$\Psi(\mathbf{x}_1, \ldots, \mathbf{x}_N) = J_S(\mathbf{x}_1, \ldots, \mathbf{x}_N)\, \Psi_{AS}(\mathbf{x}_1, \ldots, \mathbf{x}_N). \tag{5.1}$$

where $\mathbf{x}_i \equiv \{\mathbf{r}_i, \sigma_i\}$ is a space-spin coordinate, the factor J_S is the symmetric Jastrow factor defined to be positive and symmetric upon particle exchange, and Ψ_{AS} is the antisymmetric factor which typically is a determinant or sum of determinants. The Jastrow factor can be further factored into symmetric one-body, two-body, three-body, and higher terms which correspond to electron-ion, electron-electron, electron-electron-ion, etc. interactions. Since the Jastrow factor must be strictly positive and because the form is advantageous, the Jastrow form used throughout this work is defined as

$$J_S \equiv e^{-(J_1+J_2+J_3+\ldots)} \tag{5.2}$$

where J_1, J_2, and J_3 are one-, two-, and three-body Jastrow functions. The resulting wave function is efficient in QMC calculations and the one- and two-body Jastrow functions can be used to satisfy the cusp conditions.

The most used wave function form throughout this work is indeed the Slater-Jastrow. Single-body orbitals are obtained from theories such as HF and PBE-DFT and combined with a Jastrow factor that includes electronic correlation by way of VMC optimization of the Jastrow functions. The resulting trial function has a lower variance, smaller time-step error, and a reduced pseudopotential localization error. This form is then suitable to project out the fixed-node DMC energy. Note that in the work presented here, no attempt is made to modify the Slater factor so that the nodal surface is that from the single-body theory used (e.g. HF or PBE-DFT). However, as will be shown, this nodal surface is sufficient to recover much of the correlation energy while at the same time there is a partial cancellation of the fixed-node error in energy differences. Still we like to qualify our results against a more correlated JAGP trial function that will be described in Sec. 5.3. However, it will be useful to discuss the cusp conditions that are relevant to both the SJ and JAGP.

5.2 Cusp conditions

Cusp conditions describe the behavior of the wave function as two (or possibly more) particles approach one another. The most important cusp conditions for the DMC algorithm are for the electron-electron and electron-nucleus cusps. While a proper cusp description is a property of the true ground state wave function, it is usually not so important in many methods because this region of configuration space can usually be integrated over. In the DMC algorithm this is not the case. The problem arises in the branching (last) term of the diffusion equation involving the mixed estimator in Eqn. 4.10. If the local energy becomes unbounded the walker population explodes ultimately resulting in the computer code crashing (typically), a potentially serious problem. In order to remedy this situation, it is necessary that the kinetic energy term in the local energy diverge with the potential energy so that a cancellation of terms keeps the local-energy finite. It should be noted that this cusp behavior is correct physics for any method since the local-energy should be a constant for the exact ground state wave function.

Starting with the electron-ion cusp conditions, consider the relevant parts of the local energy, $E_{loc} = H\Psi/\Psi$, that involve the diverging terms that must cancel as the electron-ion separation $r \to 0$. This implies

$$-\frac{1}{2}\bigtriangledown^2 \Psi - \frac{Z}{r} = 0 \tag{5.3}$$

where Z is the charge of the nucleus. Writing this in terms of the radial form of the Laplacian and neglecting terms that don't involve $1/r$ gives

$$-\frac{2}{r}\frac{\partial \Psi}{\partial r} - \frac{Z}{r} = 0. \tag{5.4}$$

Using the wave function form $\Psi = e^{-J_1}\Psi_{AS}$ (note Ψ_{AS} can be taken to include any other Jastrows for the purposes of this derivation) gives the final result which is

$$\frac{\partial J_1}{\partial r} = Z. \tag{5.5}$$

It should be noted that terms involving Ψ_{AS} have been dropped because in this work Gaussian basis functions are used (the Laplacian of a Gaussian evaluates to zero at the cusp).

The electron-electron interaction demands a cusp condition because, like the electron-ion interaction, it has a diverging potential given by $1/r_{ij}$ when electrons i and j approach one another. The main difference as compared to the electron-ion cusp is that the sign of the divergence is opposite. The derivation follows similar arguments to the electron-ion result except that now a center-of-mass Hamiltonian is required and the Jastrow function J_2 must have explicit dependence on distances r_{ij}. The cusp condition for opposite spin electrons is then given by

$$\frac{\partial J_2}{\partial r_{ij}} = -\frac{1}{2} \tag{5.6}$$

while for electrons of the same spin it is

$$\frac{\partial J_2}{\partial r_{ij}} = -\frac{1}{4}. \tag{5.7}$$

The calculations done in this work only use the two-body Jastrow for opposite spin electrons because it is recognized that the Pauli exclusion principle for fermions will prevent like spin electrons from approaching too close.

A brief word about practical implementation of the Jastrow is now in order. As mentioned above, the Jastrow factor must be symmetric under exchange. So suppose one wants to implement an electron-ion Jastrow for ion I. Then a function form is assumed so that the relationship between electron i and ion I is indicated by $J_I(r_{iI})$. Then the symmetric one-body Jastrow function for a set of ions indexed by I is given by

$$J_1(\mathbf{r}_1, \ldots, \mathbf{r}_N) = \sum_{iI} J_I(r_{iI}) \tag{5.8}$$

so that just one Jastrow function needs to be defined for each ion. Similarly, one function is needed for the electron-electron Jastrow.

In the following chapters a number of different Jastrow function forms are used. Most recently the B-spline form has been implemented in the QMCPACK code so that no functional form is assumed other than the cusp condition as a boundary condition and an additional boundary condition that enforces continuous derivatives at the cutoff. However, other forms are presented and it will prove to be more insightful to explain what is done in the context of the specific calculation. One- and two- body Jastrows are used on all the calculations with the addition of three- and four-body Jastrows, which provide electron-electron-ion and electron-electron-ion-ion correlations, used in the JAGP calculations done for the hydrogen on benzene problem.

5.3 Jastrow correlated Antisymmetric Geminal Power (JAGP)

While the Slater determinant description is appropriate for cases where correlations are weak and well-represented by the HF solution, there are notable shortcomings. For example, a single determinant fails to describe bond breaking such as $H_2 \rightarrow 2H$, where at least two determinants are required. In general, large determinant expansions dramatically increase the cost of a calculation (e.g. scaling is $\mathcal{O}(N^6)$ for SDCI and $\mathcal{O}(N!)$ for full CI). An alternative is the Jastrow correlated antisymmetric geminal power (JAGP).

A JAGP is a Jastrow correlated single-determinant wave function constructed of two-body orbitals (geminals). This approach has been successfully applied in diverse contexts where electron correlations play a significant role. For example, the JAGP form is related to the pairing in the BCS wave function for superconductivity [54, 55], molecules where resonating valence bonds (RVB) proposed by Pauling in 1939 [56] plays a role, and strongly-correlated electrons in transition metals. Recent applications include benzene [57], benzene dimers interacting via weak van der Waals forces,[58] and the iron dimer.[59]

The form of the AGP part of the JAGP wave function for an unpolarized spin singlet system is

$$\Psi_{AGP}(\mathbf{r}_1^{\uparrow}, \mathbf{r}_1^{\downarrow}, \cdots, \mathbf{r}_{N/2}^{\uparrow}, \mathbf{r}_{N/2}^{\downarrow}) = \hat{A}[\Phi(\mathbf{r}_1^{\uparrow}, \mathbf{r}_1^{\downarrow}) \cdots \Phi(\mathbf{r}_{N/2}^{\uparrow}, \mathbf{r}_{N/2}^{\downarrow})] \tag{5.9}$$

where $\hat{A}$ is the antisymmetrizing operator and the geminals are singlets given by

$$\Phi(\mathbf{r}^{\uparrow}, \mathbf{r}^{\downarrow}) = \phi(\mathbf{r}^{\uparrow}, \mathbf{r}^{\downarrow})(|\uparrow\downarrow\rangle - |\downarrow\uparrow\rangle). \tag{5.10}$$

Under the assumption that $\phi(\mathbf{r}, \mathbf{r}')$ is symmetric, the spatial part of the AGP can be written as a determinant of pairing functions [60]

$$\Psi_{AGP}(\mathbf{r}_1^{\uparrow},\mathbf{r}_1^{\downarrow},\cdots,\mathbf{r}_{N/2}^{\uparrow},\mathbf{r}_{N/2}^{\downarrow}) = \begin{vmatrix} \phi(\mathbf{r_1}^{\uparrow},\mathbf{r_1}^{\downarrow}) & \dots & \phi(\mathbf{r_1}^{\uparrow},\mathbf{r_{\mathit{N}/2}}^{\downarrow}) \\ \vdots & \ddots & \vdots \\ \phi(\mathbf{r_{\mathit{N}/2}}^{\uparrow},\mathbf{r_1}^{\downarrow}) & \dots & \phi(\mathbf{r_{\mathit{N}/2}}^{\uparrow},\mathbf{r_{\mathit{N}/2}}^{\downarrow}) \end{vmatrix} \tag{5.11}$$

and the paring function $\phi(\mathbf{r}^{\uparrow},\mathbf{r}^{\downarrow})$ can be expanded in single-body orbitals about the ionic centers so that

$$\phi(\mathbf{r}^{\uparrow},\mathbf{r}^{\downarrow}) = \sum_{lmab} \lambda_{ab}^{lm}\varphi_{al}(r_i^{\uparrow})\varphi_{bm}(r_j^{\downarrow}) \tag{5.12}$$

where l and m index the orbitals on ionic centers a and b respectively. In this work Gaussian type orbitals (GTO) are used.

The Jastrow part of the JAGP wave function provides a way for additional correlations and cusp conditions to be incorporated into the wave function. The Jastrow must therefore contain the cusps since the pairing function in Eqn. (5.12) is constructed from GTOs. For the electron-ion Jastrow, the one-body Jastrow function J_1 (as defined above in Eqn. 5.2) is used to correct the cusps where electrons approach ions and is given by

$$J_1(\mathbf{r}_1,\ldots,\mathbf{r}_N) = \sum_i\sum_I (2Z_a)^{3/4}u((2Z_I)^{3/4}|\mathbf{r}_i - \mathbf{R}_I|) \tag{5.13}$$

where the sum I is over ion centers, and ion charge and position are given by Z_a and $\mathbf{R}_a$ respectively, $u(x)$ can take any form where $u(0) = 0$ and $u'(0) = \frac{1}{2}$ (e.g. a Padé form). In this work, $u(r) \equiv \frac{F}{2}\left(1 - e^{-r/F}\right)$ where F is an optimizable parameter. For the electron-electron Jastrow, the J_2 function is given by

$$J_2(\mathbf{r}_1,\ldots,\mathbf{r}_N) = -\sum_{i<j} u(r_{ij}) \tag{5.14}$$

and accounts for the cusp condition between up and down spin electrons. Cusps between same spin electrons are not accounted for because both antisymmetry and coulomb interaction keep them apart. The electron-electron-ion and electron-ion-electron-ion Jastrow, conventionally referred to as three- and four-body, can be thought of as a two-body Jastrow that is not translationally invariant. The J_{34} form used here is a pairing function like that in Eqn. 5.12 and is given by

$$J_{34}(\mathbf{r}_1,\ldots,\mathbf{r}_N) = \sum_{ij}\sum_{IJlm} g_{lm}^{IJ}\chi_{Il}(\mathbf{r}_i^{\uparrow})\chi_{Jm}(\mathbf{r}_j^{\downarrow}). \tag{5.15}$$

where g_{lm}^{IJ} are optimizable parameters and l, m index orbitals on nuclei I, J respectively. This three- and four-body term provides for electron-correlations substantially beyond the largely cusp related one- and two-body terms and is able to describe subtle effects like van der Waals forces at the VMC level as has already been demonstrated in previous work.[61] However, Eqn. 5.15 does not include the three-body cusp conditions recently derived by Fournias *et al.*,[62] which can improve the quality of the nodes of the JAGP wave function described here. The effect of the three-body cusp conditions in the energy optimization and nodal structure is presently under investigation.

Chapter 6

Hydrogen

6.1 Motivation

Hydrogen is a crucial and fundamental part of most of the systems that are studied in this work. Certainly the solution to the hydrogen atom is known analytically and very accurate solutions to H_2 have been known for a long time.[63] That being said, the solution to H_2 in several theories is important for comparison purposes as well as finding formations energies for other systems. More importantly, the treatment of hydrogen specific to this work deserves to be detailed and clarified. Carefully describing what was done and why regarding this simplest of atoms actually demonstrates a template of approach that eliminates a lot of the trial and error and guess work as the work progresses toward larger and more difficult systems. I will show how the hydrogen Jastrow is constructed and why. Also, the Hartree-Fock and PBE-DFT solutions will be compared for triple and quadruple zeta basis sets. Convergence in DMC will be tested and comparison will be made between the DMC result using HF and PBE-DFT optimized geometry and the exact solution.

In every case, H_2 should never be taken for granted and has served consistently as a first test to validate that codes are working as expected and input files are properly constructed. One of the very nice features of H_2 is that it is bosonic and as such has no fixed-node error in DMC so that it is possible to compute the exact ground state energy to whatever precision one is willing to pay for. Care must still be taken, however, because the exact solution is the limiting case of small time step and corresponding time step error. Gaussian basis functions are used throughout this work and while they have some significant advantages they also have some disadvantages as well. As mentioned in Chapter 5, Gaussian basis functions do a poor job of describing the cusp conditions because the gradient of a Gaussian type orbital (GTO) is always zero. Additionally, even a Gaussian contraction cannot properly describe the tail because Gaussian functions always approaches zero faster than exponential beyond some radius. Of these two issues, the cusp issue is the most important for the QMC methods used here.

6.2 Methods

While a possible solution to the one-body cusp problem is to use pseudo-hydrogen (hydrogen with a pseudopotential), we prefer and choose to use the standard Coulomb potential. The cusp can be included in the Jastrow as was discussed in Chapter 5. However, the cusp is generally very short ranged while any abnormal tail behavior due to either basis set or theory is very long range. Much of this work employs uniform cubic B-splines in order to describe trial function Jastrows and radial functions in general. It is disadvantageous to use the same high resolution B-spline to describe both the short range cusp behavior and the long range tail behavior. For this reason a double Jastrow will be used to describe hydrogen. A high resolution short range Jastrow will describe the cusp while a lower resolution long range Jastrow will describe the tail. A final note is that the electron-electron Jastrow (for H_2) does not require a double Jastrow, however, it should be as extensive as possible.

Using B-splines certainly offers many advantages, not the least of which is their flexibility to describe unknown Jastrow forms. However, B-splines as used here are necessarily of limited range and have a specific cutoff which is specified in advance and should match the physics of the problem. In conducting many studies, too numerous to include here, I have found that specifying a the B-spline cutoff to land in a region of relatively high electron density can result in spikes (or strong ripples) in the local energy on and around the cutoff sphere which can result in an increased time step error. On the other hand, using too long of a cutoff results in insufficient sampling of the tail region which results in the Jastrow being ill-defined and can cause problems in the optimization of the Jastrow. The most straight-forward means of addressing this issue is to plot the charge density as a function of the radius and attempt to extend the Jastrow as far a possible.

6.3 Results and Discussion

Consider the plots of an ideal PBE-DFT hydrogen Jastrow given in Fig. 6.1. Both plots are of the same Jastrows. The two Jastrows in each figure, indicated by red and blue, correspond to a 3- and 4-zeta basis respectively. Notice that the main difference is that the wiggles in the 3-zeta basis are more pronounced. Figure 6.1a gives the long range view extending out to 8 Bohr so that it is clear there is a very small cusp region near the origin. Figure 6.1b gives an expanded view near the origin so the fine structure of the Jastrow can be seen. As it turns out, the first and second hump are most always present even in molecular calculations. These vary over a vary small range and are not well described by a long range Jastrow unless a lot of variables are used. In order to address this, a double Jastrow will be employed. A short range Jastrow with resolution of 0.1 Bohr extending out to 0.6 Bohr and a long range Jastrow with resolution of

0.5 Bohr extending out as far as practical, in this case 8 Bohr.

Regarding geometry optimization and basis sets. I have found through experience that the difference between 3- and 4-zeta in terms of geometry optimization is very minimal. While it might seem somewhat anecdotal, consider the PBE-DFT and HF plots of H_2 given in Fig. 6.2. By inspection it appears that the curves are more or less offset vertically. This is not strictly true of course, but it should be clear that the optimal geometry will not change much while the energy will changes significantly with basis. I can say through experience that this holds basically true even for the the most complicated molecular systems presented in this thesis research.

Converging DMC results for time-step error is always a concern. For this reason I use H_2 to show that indeed the Jastrow setup described above does indeed result in good convergence at a sensible time-step. H_2 is a very nice example of this because the cusp conditions are in play but there is no fixed node error so that in principle as accurate an answer as desired can be obtained. Results are presented in Fig. 6.3. Convergence is found to occur somewhere around τ=0.02 and 0.04. Excellent agreement is seen when plotted against what is essentially the exact answer to eight figures.[63].

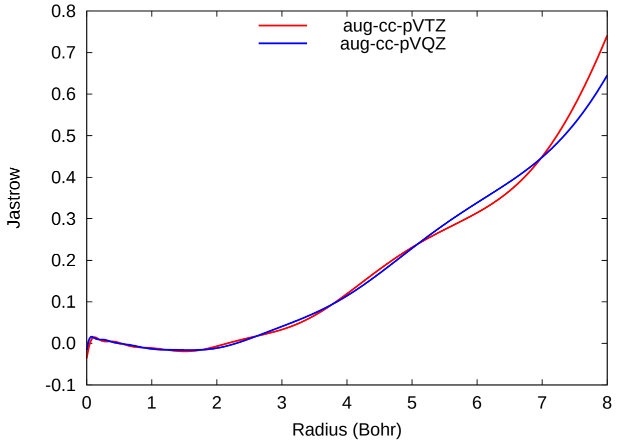

(a) PBE-DFT atomic hydrogen ideal Jastrow - long range behavior

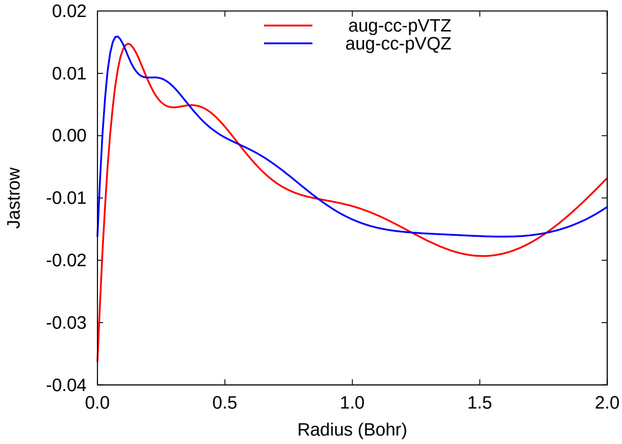

(b) PBE-DFT atomic hydrogen ideal Jastrow - short range behavior

Figure 6.1: Both figures above show the ideal Jastrow for atomic hydrogen when the trial function is derived from PBE-DFT. A Slater-Jastrow composed of the PBE-DFT single-body orbital and the above Jastrow results in the exact solution for atomic hydrogen. The top figure (a) shows the long range behavior while the bottom figure (b) shows the cusp and short range behavior. The basis sets used are aug-cc-pVTZ and aug-cc-pVQZ indicated by red and blue respectively.

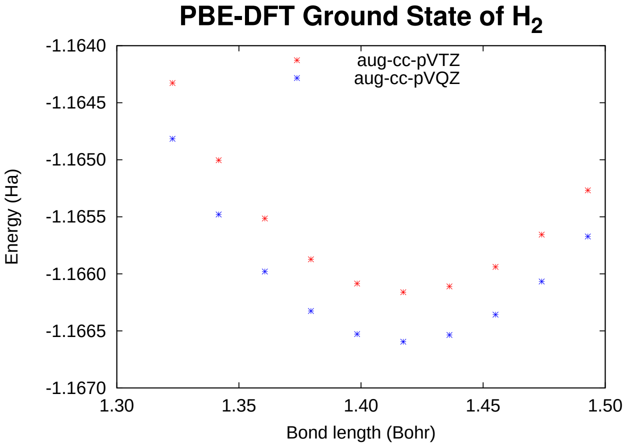

(a) Potential energy curve of H_2 for PBE-DFT

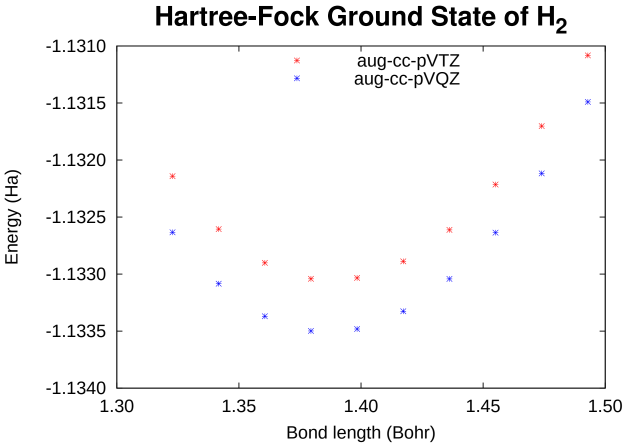

(b) Potential energy curve of H_2 for Hartree-Fock

Figure 6.2: Both figures above show the potential energy curve of H_2 with respect to bond length. Red and blue correspond to aug-cc-pVTZ and aug-cc-pVQZ respectively. (a) Shows the PBE-DFT results while (b) shows the HF results.

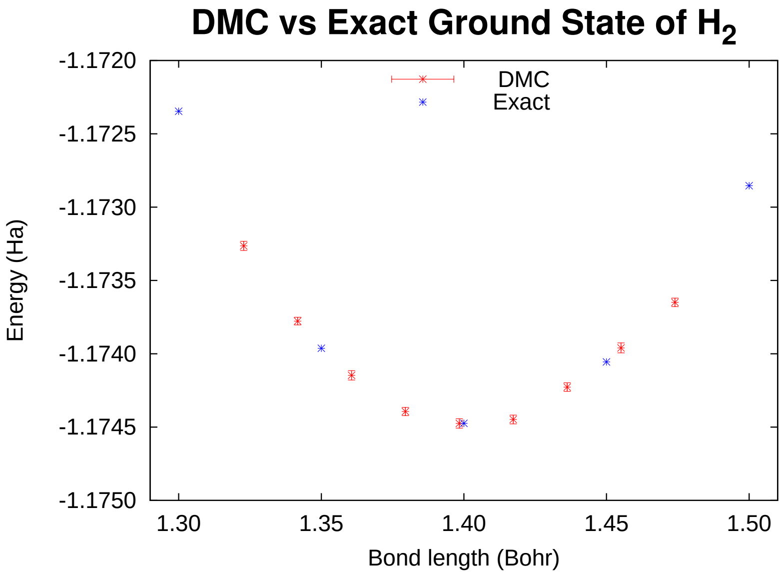

Figure 6.3: DMC potential energy surface using a PBE-DFT trial function with B-spline Jastrow for both one- and two-body terms. Both Jastrows use a an 8 Bohr cutoff and 0.5 Bohr resolution. The one-body Jastrows has an additional short range Jastrow with 0.6 Bohr cutoff and 0.1 Bohr resolution.

Chapter 7

Hydrogen on Benzene

The work in this chapter was conducted in collaboration with my coworkers[1] and has already resulted in a publication in the Journal of Chemical Physics in 2008.[17] This study was the first major research focus of my thesis work for several reasons and lends perspective and insight to QMC study of hydrogen storage systems. It should be noted that previous work had already indicated this system as weakly bound. Weak binding systems are difficult for many theories and QMC methods are no exception. Thus hydrogen on benzene is an excellent test to see how well our methods perform. Also, we compare to significantly different trial wave function forms, the Slater-Jastrow and the JAGP or geminal trial functions. Essentially, we would like to establish if the cancellation of fixed-node and pseudopotential localization errors resulting from a SJ trial function with PBE-DFT single-body orbitals is sufficient in sensitive systems. As a matter of practicality, the SJ form is desirable due to the many well tested tools already available to generate the Slater part of the trial function and a significant reduction in the number of parameters to optimize.

The details of hydrogen binding on benzene present additional concerns. We are testing PBE-DFT on a system where van der Walls (VdW) or dispersion forces play a significant role. The PBE-DFT functional is not designed to capture correlations due to these effects, but those effects can in principle be recovered in DMC using a PBE-DFT trial function. In addition, the benzene molecule involves a resonating valence (RVB) bond between the carbon atoms which is shown diagrammatically in Fig. 7.1. It is not clear *a priori* that the nodal surface of a Slater determinant is sufficient at the DMC level to capture RVB correlation effects. The extent to which the fixed-node DMC recovers those

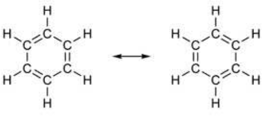

Figure 7.1: Standard picture describing the resonating valence bond in benzene. This can be understood as benzene being in a superposition of two competing stable bond configurations.

---

[1] The authors of this paper (in order) are myself, Michele Casula, Jeongnim Kim, Sandro Sorella, and Richard M. Martin.

correlations effects needs to be tested.

The JAGP trial function, which was described in chapter 5 may literally be interpreted as a superposition of bonds similar to the resonating valence bonds picture first proposed by Pauling in 1939 [56] and is therefore seen as ideally suited as a strong comparative standard. This wave function is even versatile enough to describe pairing in the BCS wave function for superconductivity and strongly-correlated electrons in transition metals. Recent applications include benzene,[57] benzene dimers interacting via weak van der Waals forces,[58] and the iron dimer.[59] Since the H_2 binding energy is expected to be small, the quality of the trial wave function is all the more important. The quality of this trial function form is enhanced because the VMC optimization involves the determinant in addition to the Jastrow so that correlation effects, including those due to VdW, can be accounted for in the nodal surface. Since the trial functions are significantly different, the sensitivity of the fixed-node approximation can be assessed.

7.1 Computational details

7.1.1 Slater-Jastrow trial function

The Slater part of the Slater-Jastrow trial function (see Sec. 2.1) was constructed of single-body orbitals via the Perdew-Burke-Ernzerhof [29, 30] (PBE) functional in DFT theory using the Gaussian03 [64] computer code. The single body orbitals are built of a VTZ Gaussian basis [65] modified to include diffuse functions from the aug-cc-pVTZ basis.[66] We chose to use a very simple Jastrow factor because our goal was to improve DMC efficiency as opposed to obtaining a well converged binding curve at the VMC level. The Jastrow factor we applied to the Slater determinant is a Wagner-Mitas form [67] modified so that the electron-ion and electron-electron cusp conditions are fulfilled. The one- and two-body Jastrow functions, as defined in Eqns. 5.2 and 5.8, are given by

$$J_I(\mathbf{r}_{iI}) = \sum_k -(b_{Ik} r_{iI} + c_{Ik}) \upsilon_{Ik}(r_{iI}) \tag{7.1}$$

and

$$J_{ee}(\mathbf{r}_{ij}) = \sum_k -(b_k r_{ij} + c_k) \upsilon_k(r_{ij}) \tag{7.2}$$

where i, j and I index electrons and ions (i.e. nuclei) respectively, r_{iI} and r_{ij} are electron-ion and electron-electron distances, and k indexes the expansion terms. In our work we used three terms and, when needed, a cusp term. In the above equations, $\upsilon_k(r) = (1-z(r/r_{cut}))/(1+\beta_k z(r/r_{cut}))$, with $z(x) = x^2(6-8x+3x^2)$ and parameters b, c, β optimizable (with the exception of those that are cusp dependent). The function $z(x)$ has the properties $z(0) = z'(0) = z'(1) = 0$ and $z(1) = 1$, so that the Jastrow has a well defined cutoff at $r_{cut} = 10$ Bohr. Cusps between same spin electrons are not accounted for. This is justified because of the Pauli exclusion principle, which keeps them apart. It should be emphasized that the single-body Slater orbitals obtained from PBE-DFT are not further optimized since we would like to check the accuracy of the PBE-DFT nodes with respect to a more correlated and fully optimized wave function, such as the JAGP form described below. However, optimizing the above Jastrow is convenient as it improves the VMC energy and variance and shortens the DMC projection time, without changing the nodes. This optimization is done using a stochastic version the conjugate gradient method.

7.1.2 JAGP function

The JAGP bases are constructed from Gaussians as follows. For the AGP basis we use a contracted $(6s6p)/[2s2p]$ for the carbon atoms, $(2s2p)/[1s1p]$ for molecular hydrogen's atomic sites, and a single s Gaussian for benzene's hydrogen sites. For the Jastrow we use an uncontracted $(3s2p)$ basis for the carbon sites, an uncontracted $(1s1p)$ for molecular hydrogen's atomic sites, and a single s Gaussian for benzene's hydrogen sites. Each atomic basis in the Jastrow includes a constant that generates additional electron-ion terms when multiplied by other orbitals χ_{bm} in Eqn. 5.15. For benzene's hydrogen constituents we used just a single s Gaussian both in the AGP and Jastrow geminals, since they are not supposed to play a key role in the interaction between the hydrogen molecule and the benzene ring. The fully optimized benzene basis included in the JAGP wave function gives a quite good variational energy for aromatic rings.[57] An analysis of the basis used for the hydrogen molecule will be given in Sec. 7.2.1.

7.1.3 Methods

In setting up our Hamiltonian, we use the Born-Oppenheimer approximation, a Hartree-Fock norm conserving soft pseudopotential for the He core of carbon[2], and the bare Coulomb potential for hydrogen and electron-electron interactions. Our procedure is to start with a trial wave function which includes variational parameters (see Chap. 5 for the forms employed in this work). We proceed to optimize its energy and variance at the VMC level using minimization methods suitable for the particular form.[68, 69, 48, 70] The resulting analytic wave function is projected to the FN ground state using DMC methods[47, 18] recently developed to yield a stable simulation and an upper bound of the ground state energy even for non-local pseudopotentials.

As we mentioned above, we use the full electron-nucleus Hamiltonian except for the carbon core which is replaced by a pseudopotential. This leads to better statistics due to a narrower energy scale, a reduction in the number of optimization parameters, a more stable optimization of our JAGP wave function,[48] and

---

[2] The pseudopotentials we used are norm-conserving Hartree-Fock generated by E. Shirley's code with the construction by D. Vanderbilt, Phys. Rev. B **32**, 8412 (1985).

a larger DMC time step needed for convergence, which results in a cheaper computational cost of the simulation. On the other hand, its drawback is that part of the fully local Coulomb potential is replaced by a non-local pseudopotential $V_{\text{non-local}}$ that is angular momentum dependent. Within the VMC framework the corresponding angular integration of the non-local potential remains possible since the wave function is known analytically. However, problems arise in the FN DMC because the FN ground state is given only by a stochastic sampling. A partial solution is the localization approximation, where the trial (or guiding) wave function Ψ_G is used to approximate the projected ground state so that the non-local pseudopotential terms can be evaluated.[44] However, numerical instabilities are introduced and the projected energy is no longer a variational upper bound of the original non-local FN Hamiltonian.

Our FN DMC calculations are done with either continuous or lattice regularized (LRDMC) moves both of which utilize a common means of treating the non-local part of the pseudopotential. In contrast to the localization approximation, we use a breakup[47, 18] of the non-local potential that localizes the positive matrix elements into the branching term while treating the negative matrix elements as a non-local diffusion operator sampled via a *heat bath* scheme.[18] The details of this procedure are given in Sec. 4.4.

Our SJ calculations were done using continuous space DMC with QMCPACK [53]. This code provides many features that make it easy to work with SJ wave functions. The LRDMC method, available in the TurboRVB,[71] has been applied to the JAGP wave function after a full optimization of its parameters. We used two optimization procedures. For the SJ work we employed the method of conjugate gradients (CG) introduced by Hestenes and Stiefel[68] in 1952. This is a first-derivative method that finds the minimum of a cost function (in our case a linear combination of the variance and the energy), in a number of steps significantly smaller than the standard steepest descent method, because for a quadratic cost function it converges in a finite number of iterations, at most equal to the dimension of the vector space.[25, 26] We optimized 10 parameters of the Jastrow functions but used the same VTZ basis set at all hydrogen-benzene molecular separations. However, the statistical noise inherent in the QMC framework limits the applicability of our CG implementation to systems involving not too many parameters, such as our SJ optimization. The JAGP optimization, on the other hand, involves a large number (~ 1000) of parameters, mainly coming from the λ_{ab}^{lm} (Eqn. 5.12) and g_{lm}^{ab} (Eqn. 5.15) matrices in the AGP and Jastrow geminal expansions over the atomic basis set. Therefore, an optimization technique robust under stochastic conditions is required. For this we used the stochastic reconfiguration (SR) method recently introduced by one of us (S.S.) [69] in conjunction with subsequent improvements, [48, 72, 73, 70] including Hessian acceleration which is explained in Ref. [48], that have been shown to be very efficient in minimizing the variational energy.

7.2 Results

In this section we present results for hydrogen-benzene binding where the hydrogen molecule is oriented along the C_6 symmetry axis of the benzene molecule. Previous studies[74, 75] found this configuration the most stable. Here, we do not take into account other possible orientations, because our goal is to check the accuracy of different QMC wave functions and provide benchmarks for the lowest energy configuration. In order to resolve its potential energy surface, we consider the system at different molecular center-of-mass separations R. In our QMC calculations we have kept the geometry of each molecule fixed and close to its experimental structure.[3] We checked the effect of relaxing the geometries at the MP2 level and found an energy lowering on the order of μHa, indicating this effect is completely negligible.

We emphasize that our QMC results do not include any corrections for basis set superposition error (BSSE). The binding curves and the final results for binding energies and distances are determined from directly calculated energy differences with the largest computed distance ($R = 15$ Bohr) taken as the zero energy reference. On the other hand the results presented for the DFT calculations have included a correction (see Sec. 2.3 for a description); we quantified the BSSE using PBE-DFT using the VTZ basis with added diffuse functions. In that case, the BSSE correction was 0.39 mHa, roughly half the corrected binding energy which was found to be 0.79 mHa at 6.45 Bohr.

The BSSE arises due to an incomplete basis set, and it is important to point out that the magnitude of the effect is different in the various QMC methods. In VMC the BSSE are due to the finite basis and the consequences can be understood using the same arguments as for other variational methods. In the present work, the error is greatly reduced because we fully optimize the AGP and Jastrow bases along with all exponents at each R. In DMC methods, the basis is complete in the continuous configuration space, and the only inherent limitation is the fixed node (FN) approximation. Since we use nodes determined with a finite basis there is necessarily some error due to superposition; however, the effect upon the final DMC energies is greatly reduced since the diffusion algorithm leads to the best possible estimate of the energy within the nodal constraint.

Our results support this analysis and justify the conclusion that the BSSE errors are negligible for the QMC calculations reported here. The good agreement between the VMC and DMC JAGP results, presented in Subsec. 7.2.1, highlights that the basis set superposition bias is not relevant (smaller than the statistical error of ~ 0.2 mHa) for the fully optimized basis set used in the JAGP wave function, while the agreement between the projected SJ and JAGP energies, shown in Subsec. 7.2.2, suggests that the FN bias is negligible.

---

[3] The actual bond lengths used in this work are: $C - C = 2.63$ Bohr, $H - C = 2.04$ Bohr, and $H - H = 1.40$ Bohr. They are close to the best experimental and theoretical values.[76, 77]

It should be noted that there is another possible kind of basis error that can also occur due to restrictions in the trial wave functions. If the trial functions are zero (or very small) in regions of configuration space, then the DMC calculation may not properly sample the full space. This can happen particularly in the tails of the wave functions, and it is important to ensure that the basis includes sufficiently diffuse functions so that the tail regions are properly sampled. This is especially relevant for calculation of weak binding energies with small overlap in the tails of the molecular wave functions.

Finally, we note that a further possible source error arises through use of a pseudopotential to replace the effect of the cores of the carbon atoms. In the previous section we discussed the procedures for treating the errors due to use of non-local pseudopotentials in DMC. Errors due to these and other effects of the pseudopotential should cancel in the energy differences, because the effects occur mainly in the core region, which changes very little as a function of the distance between the molecules for any separation relevant to the present problem.

7.2.1 Jastrow correlated Antisymmetric Geminal Power

We optimized the variational JAGP wave function by means of the most recent version of the stochastic reconfiguration energy minimization with Hessian acceleration.[48] Although the basis set used here is quite compact, it turns out that the variational energies are very accurate, as we optimize both the determinant and Jastrow part. For instance, the basis set for the hydrogen molecule is a $(2s2p)/[1s1p]$ Gaussian in the AGP expansion, while it is an uncontracted $(1s1p)$ Gaussian plus a constant in the Jastrow geminal. In spite of this small basis set, the variational energy of an isolated H_2 molecule is $-1.174077(29)$, very close the exact result (-1.174475).[78] The second Gaussian in the s and p contractions of the hydrogen AGP is fairly diffuse, their exponents ranging from 0.05 to 0.1, as the distance R between the benzene molecule and the hydrogen dimer shrinks from 15 to 6 Bohr.

We found that the inclusion of the diffuse orbitals in the basis set of the hydrogen molecule is crucial for the hydrogen-benzene binding, both at the VMC and LRDMC level. On the other hand, some Gaussians related to the contracted p orbital of the benzene ring become more delocalized in the binding region. This is reasonable, because the interaction is supposedly driven by the resonance between the carbon p_z and molecular hydrogen s components of the total wave function. Therefore, the minimal basis set should include diffuse orbitals on both sides. We would like to stress that the extension of those diffuse orbitals is not determined *a priori*, but is found by optimizing the wave function with the necessary variational freedom.

After a full optimization of the variational wave function at several distances $(R = 5, 5.5, 6, 7, 8, 10, 15$ Bohr) we carried out VMC and LRDMC simulations to study the properties of the system, in terms of energetics and charge density distribution. The LRDMC kinetic parameter in Eqn. 4.14 which optimizes the lattice space extrapolation is $\mu = 3.2$, that allows one to work with a quite large (and highly efficient) mesh size ($a = 0.25$ a.u.). Properly setting the parameters of the LRDMC effective Hamiltonian is crucial in order to speed up the simulation, and so be able to resolve the small binding energy of this system. To check the convergence of our LRDMC energies with respect to the mesh size, we computed the energy difference $E(R = 6) - E(R = 15)$ for $a = 0.125$, 0.25, and 0.5, as reported in Tab. 7.1. It is apparent that the energy differences are converged within the error bar of 0.25 mHa in the lattice space range taken into account. It is therefore accurate to work with $a = 0.25$.

Table 7.1: LRDMC binding energy ($E(R = 6) - E(R = 15)$) dependence on mesh size a. The energies are reported in mHa, the lengths are in Bohr.

a	E_{binding}
0.125	1.53(24)
0.25	1.57(19)
0.5	2.07(23)

The results of our calculations of the VMC and LRDMC dispersion curves are presented in Fig. 1a, 7.2a, which shows the energy as a function of distance R relative to the value at $R = 15$ Bohr for each of the methods. There is excellent agreement between the two curves, with a difference that is less than 0.18 mHa for most points. Of course, the diffusion calculation leads to a lower total energy than the variational calculation in every case, but the agreement of the two methods for the energy difference supports the idea that our results are accurate and the calculated binding energy is close to the exact value.

In order to extract the values for the equilibrium distance R_0 and the binding energy E_{b}, we fitted our LRDMC points with the Morse function:

$$V(R) = E_\infty + E_{\text{b}} \left[e^{-2a(R-R_0)} - 2e^{-a(R-R_0)} \right], \tag{7.3}$$

where a is related to the zero point motion of the effective one dimensional potential $V(R)$, and E_∞ is chosen to be $E(R = 15)$, i.e. the zero of energy. This choice is motivated by the fact that the overlap of the wave function in between the two fragments is negligible at that distance. Beyond that point the variation of $V(R)$ up to infinity is much smaller than the statistical accuracy of our points. We estimated the error on the fitting parameters by carrying out a Bayesian analysis of the fit, in a way similar to what described in Ref. [79]. Our result is 6.33(15) Bohr for the equilibrium distance, and 1.53(12) mHa for the binding energy, as reported in Tab. 7.2.

Table 7.2: Fitting parameters of the Morse function (see Eqn. 7.3) which minimize the χ^2 of the JAGP-LRDMC and SJ-DMC data sets. Their error is computed by means of a Bayesian analysis based on the statistical distribution of the FN energy points. The energies are reported in mHa, the lengths are in Bohr.

	JAGP	SJ
a	0.56(7)	0.66(9)
E_b	1.53(12)	1.43(16)
R_0	6.33(15)	6.31(21)

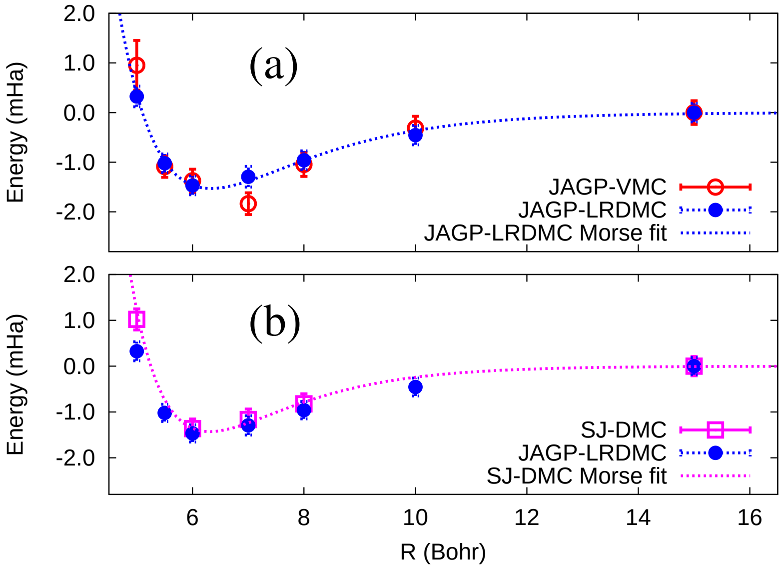

Figure 7.2: QMC results for the dispersion energy of the hydrogen-benzene bond as a function of intermolecular distance R with zero energy difference taken at $R = 15$ Bohr. (a) Compare variational and the diffusion results using the correlated geminal wave function, labeled JAGP-VMC and JAGP-LRDMC. (b) Compares diffusion results using two types of trial functions, the JAGP (the same as in Fig. a) and the Slater-Jastrow function labeled SJ-DMC. Morse fits of the diffusion data for the two wave functions are also plotted as continuous curves. The close agreement of all three results is strong evidence that the binding curve is accurate and the analytic JAGP function is a reliable representation of the fully correlated many-body valence wave function.

7.2.2 Slater-Jastrow Trial Function

At this point, it is interesting to make a comparison with a simple SJ wave function to determine whether the use of the JAGP is necessary to get the correct dispersion energy out of the FN projection. The Slater part is constructed of PBE-DFT single-body orbitals and a simple Jastrow as described in Section 7.1.1. We chose to use a simple Jastrow factor because our goal was only to improve DMC efficiency as opposed to obtaining a well converged binding curve at the VMC level. The Jastrow factor was optimized within the VMC framework using the conjugate gradient method,[68] as explained in Sec. 7.1.3. While the SJ variational energy is quite poor, its quality is not directly reflective of the DMC energy, which depends only on the nodes of the trial wave function.

Table 7.3: Slater-Jastrow trial function DMC binding energy ($E(R = 6) - E(R = 15)$) dependence on time step τ. The energy extrapolated for $\tau \to 0$ is within one error bar from the point at $\tau = 0.01$. Therefore, we chose $\tau = 0.01$ as the time step for all our DMC simulations. The energies are reported in mHa, the time steps are in Ha^{-1}.

τ	E_b
0.01	1.38(19)
0.02	0.93(19)
0.04	0.64(15)

We found that the DFT nodes are very good by carrying out DMC simulations with the non-local scheme. Our projection was done in time steps of $\tau = 0.01$ which we found to be converged as reported in Tab. 7.3. Remarkably, the DMC-SJ energies are in very good agreement with the LRDMC-JAGP data points (see Fig. 7.2b. Indeed, the SJ fitting parameters of the Morse dispersion curve (Eqn. 7.3), such as binding energy, equilibrium distance, and curvature, differ from the JAGP ones by less than one error bar (Tab. 7.2). This consistency between different trial wave functions signals that the FN bias is negligible and the results are well converged. Moreover, in addition to the nodes of the PBE wave function being good, the PBE binding energy is underestimated only by a factor of 2 with respect to our best value. It is notable that the PBE functional performs quite well, even though it does not include any VdW contribution. In the case of a pure VdW bond, the PBE result should be much poorer, as already pointed out by Hamel and Côté.[74] This is suggestive of a more complex binding mechanism which goes beyond the standard physisorption. We will focus on this point in Sec. 7.4.

7.3 Comparison to other work

The hydrogen-benzene system has been the subject of several theoretical works, whereas to our knowledge no direct study of this system has been carried out on the experimental side. Hydrogen adsorbed on metal-organic frameworks (MOF), where benzene-like structures serve as ligands, has been studied by Rosi *et al.*[10] who performed inelastic neutron scattering (INS) measurements. The INS data could be related to the rotational states of hydrogen adsorbed over benzene. However, the binding sites in the MOF structure are not known with certainty, and thus it is hard to find a one-to-one correspondence between the experiment and the isolated hydrogen-benzene compound.

Given the lack of direct experimental data for this system, we compare our results with those from empirical models that are often used to estimate complex

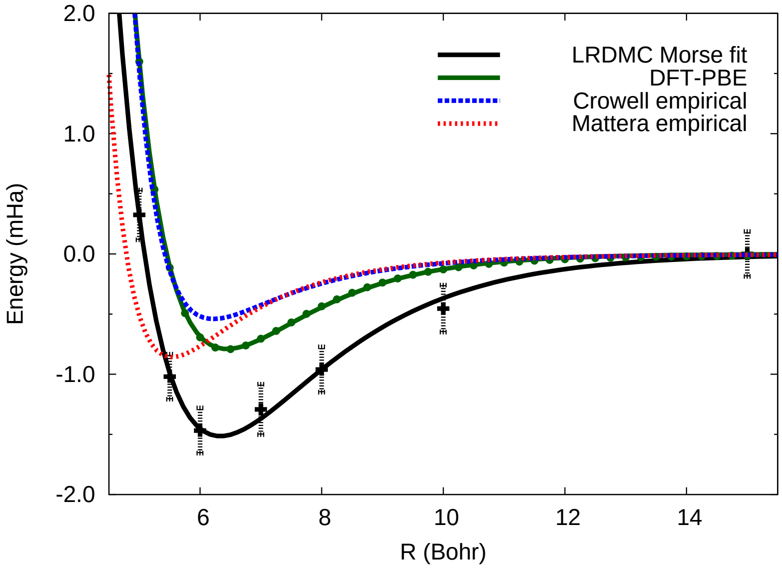

Figure 7.3: Results for hydrogen-benzene binding as a function of intermolecular distance R using four theoretical methods. The JAGP-LRDMC data and Morse fit with zero binding energy taken at $R = 15$ Bohr is shown in solid black. The PBE-DFT counterpoise corrected result using the VTZ basis plus diffuse functions from the aug-cc-pVTZ basis is shown in solid green. The Crowell and Brown empirical potential (shallowest) that takes into account the bond asymmetry of the sp^2 hybridized carbon atom is shown in dotted blue. The Mattera *et al.* empirical potential that seeks to reproduce the hydrogen bound states over graphite by a much simpler model is shown in dotted red.

system properties, such as the hydrogen storage capabilities of carbon nanotubes and fullerene nanocages.[80, 81] Here we consider two empirical models, both derived from experiments of hydrogen molecules scattered on graphite surface, carried out by Mattera *et al.*.[82] To reproduce their data, they proposed a simple model interaction between the carbon atoms and the hydrogen dimer which depends only on the distance from the graphite layers by assuming a lateral average. This model was improved later by Crowell and Brown,[83] who constructed an empirical potential based not only on the experimental scattering data but also on the polarization constants built in the VdW (6,12) potential. Their model assumes both a radial and angular dependence, which takes into account the sp^2 hybridization asymmetry of carbon atoms in graphitic and aromatic compounds. We applied these potentials to the hydrogen-benzene system by summing the terms for the 6 carbons taking into account distance and, for the Crowell potential, the angle the hydrogen-carbon interaction makes with the benzene C_6 axis. Both empirical potentials significantly underbind the system, roughly by factors of 2 and 3 respectively when compared to the JAGP LRDMC results (see Fig. 7.3). More precisely, Mattera's interaction gives a binding energy of 0.86 mHa at 5.6 Bohr, while Crowell's gives a minimum of 0.54 mHa at 6.2 Bohr.

Hamel and Côté[74] calculated the dispersion curves using DFT with the local density and generalized gradient approximations (LDA and GGA) where the GGA is implemented in the PBE density functional.[29, 30] Their calculations used a plane wave basis with a 60 Ha cutoff. They found that the DFT-LDA gives the strongest binding (3.30 mHa), while the DFT-PBE binding is much weaker (0.69 mHa). This is consistent with the general overbinding of LDA and underbinding of PBE. It is also well known that DFT is not a favorable method for systems where van der Waals forces play an important role;[4] in those cases, MP2 and CCSD(T) can be applied with more reliability. Hamel and Côté also calculated binding curves using those theories. They found MP2/6-311+G(2df,2p) binding of 1.58 mHa and CCSD(T)/6-31+G(d,p) binding of 0.65 mHa.

Perhaps the most careful and accurate MP2 and CCSD(T) calculations were done by Hübner *et al.*[75] In order to resolve the weak interaction between hydrogen and benzene, high accuracy is required, and so a large basis set is needed to reduce both basis set superposition and incompleteness errors which are a significant fractions of the binding energy (the BSSE was found to be as much as $\sim 25\%$ of the final estimated binding). On the other hand, the use of a larger basis set is limited by a poorer scaling of the calculations, particularly at the CCSD(T) level of theory, which is the most expensive. In their work, Hübner *et al.* optimized the binding distance using MP2 with the TZVPP basis. They found a center-of-mass distance of 5.80 Bohr and a binding energy of 1.47 mHa. This geometry was then used for further MP2 and CCSD(T) calculations. The CCSD(T) method with the same TZVPP basis gives 1.17 mHa, while the MP2 theory was pushed up to a aug-cc-pVQZ$'$ basis to give a binding of 1.83 mHa, a significant increase from the TZVPP basis. At this point, it is possible to estimate the true binding energy by correcting the best MP2 energy with the CCSD(T)-MP2 difference obtained at the TZVPP level. This gives a value of ~ 1.5 mHa, remarkably close to the JAGP LRDMC binding of 1.53 ± 0.12 mHa, found in this work.

7.4 Analysis of the bonding

In order to investigate more deeply the physics of hydrogen adsorbed on benzene, we study the induced difference in electronic density at the equilibrium bond distance with respect to the separated fragments. For this study we compare our best DMC results to the density functional calculation using the PBE functional. The QMC densities are calculated from the optimized correlated geminal (JAGP) as a mixed estimator, which is an accurate representation of the DMC

---

[4] Note that in our work, we used the single-body orbitals from the PBE-DFT calculation in the Slater-Jastrow wave function. The DMC energies depend only on the accuracy of the nodes of the many-body wave function. The DMC calculation includes van der Waals attraction and other terms and the result is independent of the errors in the PBE functional for the energy.

results since the diffusion calculation leads to only small changes (within the error bar) from the VMC density. The contour plot in Fig. 7.4 shows the difference in the calculated electron density at the separation $R = 6$ Bohr. Here, the electron density of the isolated molecules has been subtracted from the combined system so that the change in charge distribution due to bonding is apparent. In this figure the benzene ring lies in the xy plane at $z = 0$ and the hydrogen molecule is oriented along the z axis, with its center of mass at $z = 6$ Bohr. The two dimensional plot in the yz plane is generated by integrating the density distribution over the x coordinate. As one can see, the hydrogen molecule is polarized by the electronic repulsion with the benzene cloud, which pushes the electrons to the opposite side of the molecule, leading to a static dipole moment on the hydrogen. On the other hand, the density redistribution in the benzene is non trivial, and shows patches of charge accumulation and depletion. To catch the net effect of this redistribution, we integrated the density also over the y coordinate, and obtained an effective linear density profile, plotted in Fig. 7.5. Here, it is apparent that the overall effect on the benzene is the formation of another effective dipole moment, oriented to the same direction as the static dipole moment on the hydrogen molecule, which lowers the electrostatic energy. Notice that in Fig. 7.5 we have plotted separately the VMC and the LRDMC mixed estimate of the densities. The close agreement supports our conclusion the VMC wave function is very accurate not only for the energy but also for other properties such as the density.

At large distances the attractive interaction is due to VdW dispersive forces, which is included in the Monte Carlo calculations. At short distances the interaction is repulsive due to overlap of the closed shells, which would lead to density displaced outward on both the hydrogen and benzene, i.e. opposite dipoles on the two molecules. However, Figs. 7.4 and 7.5 show that the hydrogen-benzene bond is not a pure VdW interaction, since in the binding region also electrostatic effects come in with the onset of dipolar interactions that lower the charge repulsion. For comparison, density differences calculated using the PBE density functional are also shown in Figs. 7.4 and 7.5 at the separation $R = 6$ Bohr. Of course, the PBE functional does not include VdW interactions so that the binding decreases too rapidly at large distance as shown in Fig. 7.3. Nevertheless, near the equilibrium distance the density is similar to the QMC result but with smaller magnitude of the change in density, which is consistent with the fact that the PBE functional underbinds the system. It is well known that GGA functionals like PBE tend to underbind because they favor systems with larger gradients, whereas LDA tends to overbind molecules and solids since it favors more homogeneous systems.[26] Recent work by Langreth *et al.*[84, 85] has led to improved functionals including van der Waals interactions; however, they have not been considered here.

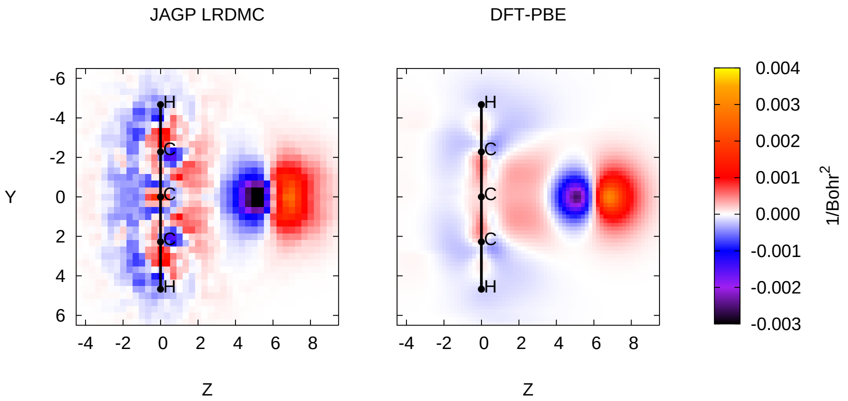

Figure 7.4: Contour plots of the difference in projected electronic charge per unit area between hydrogen-benzene separated by 6 Bohr and the isolated hydrogen and benzene using JAGP-LRDMC and PBE-DFT. The x-axis has been integrated over so that the charge per unit area has been projected into the yz-plane. (Left) The areal charge density difference is a mixed estimate of LRDMC calculations with a JAGP trial wave function. (Right) Computation is done within the PBE-DFT framework using the VTZ basis plus diffuse functions from the aug-cc-pVTZ basis.

7.5 Discussion

These benzene results, while interesting in and of themselves, have important implications for the rest of this work. In particular, the SJ trial function is found to be comparable to the more sophisticated and computationally demanding JAGP in recovering the correlation energy of the hydrogen binding on benzene. Further, this particular test case represents a strong challenge for our methods since the binding energy measured is between 5 and 10 times smaller than those associated with reversible hydrogen storage.[11] Thus for efficiency and simplicity, the SJ will be used in the remainder of this work since this trial function has demonstrated excellent results using just standard DFT methods and a Jastrow factor with significantly fewer optimizable parameters. Also, the standard DMC implementation with the variational treatment of non-local pseudopotentials will be used. The increased computational stability and cancellation of errors in localization has proven itself desirable and highly effective even in this sensitive case. Altogether, these methods represent an improvement over PBE-DFT when used by itself. As study moves to include the transition metal titanium, checks will be conducted with these said methods as the first choice.

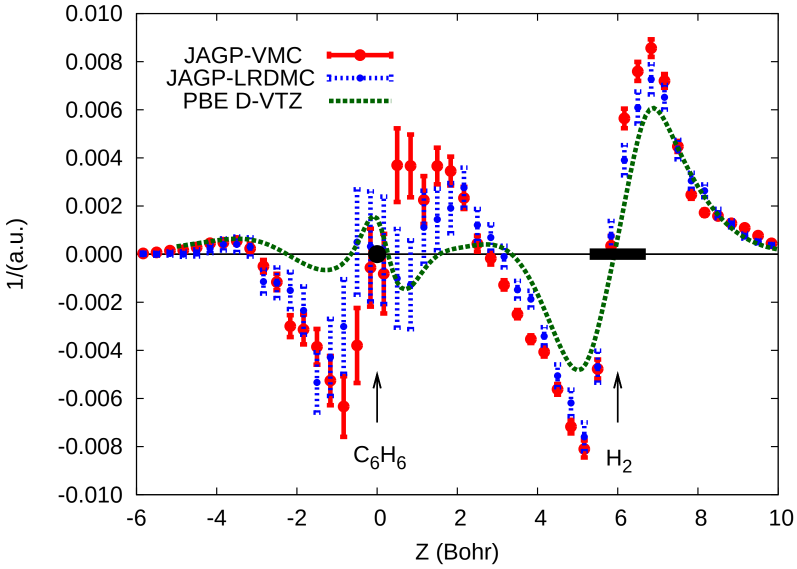

Figure 7.5: Difference in linear electronic charge density between hydrogen-benzene separated by 6 Bohr and the isolated hydrogen and benzene using three theories. The x- and y-axes have been integrated over so that the charge per unit length has been projected into the z-axis. The solid red data with error bars show the induced charge changes using the analytic JAGP wave function at the VMC level. The dotted blue data with error bars show the mixed estimate of the density given by the LRDMC projection of the JAGP trial wave function. The dotted green line shows the PBE-DFT result using the VTZ basis plus diffuse functions from the aug-cc-pVTZ basis.

Chapter 8

Atomic Titanium

The choice in studying systems that involves the transition metal titanium presents certain challenges all by itself. While the Monte Carlo methods used in this work offer an advantage in scaling, they are still costly. Pseudopotentials allow for a significant reduction in computer time and statistical fluctuations due to the elimination of the higher energy core electrons. This work chooses to use the pseudopotential recently developed by Burkatzki, Filippi and Dolg (BFD) in 2008 for use in QMC calculations.[19] Not only this, the initial work presented here allows for experience to be gained regarding d-states and role played in the overall wave function.

While the BFD Ti pseudopotential has undergone testing it has not been widely disseminated and thus it seemed good to check. Here the pseudopotential is tested in its ability to reproduce the 1^{st} and 2^{nd} ionization potentials and the lowest σ-excitation using the QMC methods specific to this work. Specifically, Slater-Jastrow trial functions will be compared using single-body orbitals from two theories, HF and PBE-DFT. Triple and quadruple zeta basis sets are used and compared. Not only this, it will allow for testing of the Jastrow factor which will be applied to the final adsorption systems of interest.

It is important to note that the BFD pseudopotential has a neon core so that the $3s^2 3p^6$... are treated as valence states and only the tightly bound $1s^2 2s^2 2p^6$ (associated with the electronic configuration of neon) are treated as core states. This has been shown by many people to be very accurate and essentially equivalent to all-electron calculations. Some early work used an Argon core pseudopotential in which the 3d states are treated as valence states, but the 3s and 3p are treated as core states as a part of the pseudopotential.[86] This can lead to large errors because the 3s, p, and d states in the same shell have large spatial overlap and large exchange that is not accurately treated by this approximation. While other work using auxiliary-field MC uses pseudopotentials with longer cutoffs r_c due to certain advantages specific to those methods in treating non-locality [87], here a *harder* pseudopotential having shorter cutoff r_c is used. This is due to the necessity of localizing the pseudopotential; the BFD version we use is designed with this particular need in mind.[19]

8.1 Angular momentum and spin states of atomic Ti

We constructed the various spin and angular momentum states as follows. First we recognized that in order to get the proper spin state of the Ti atom, the spin paired single-body states must be spatially identical. When they are not identical spin contamination is introduced. In general this did not have a great effect on our results. To construct the proper angular momentum states it is necessary to combine the proper spherical harmonics. These states are somewhat obvious when complex orbitals are used, however, this is not so much the case when a single determinant of real valued orbitals is used. Each state with its ionization, spin and angular momentum requires the construction of a proper real space state for use in our methods. The below derivation shows how those real states are determined.

8.1.1 General

We start by establishing some language and results that apply to both $\hat{\mathbf{S}}$ and $\hat{\mathbf{L}}$. Consider the case of a single Slater determinant wave function with single body orbitals given by $\chi_i(\mathbf{x}) \equiv \phi_i(\mathbf{r})\alpha(w)$ or $\chi_i(\mathbf{x}) \equiv \phi_i(\mathbf{r})\beta(w)$ where α and β are spin up and spin down respectively, ϕ is the spatial part of the orbital, and $\mathbf{x} \equiv (\mathbf{r}, w)$ the space-spin coordinate. We further stipulate that all the orbitals are mutually orthonormal. This allows us to look at the unrestricted orbital case where the spatial part of the α orbitals don't exactly match the that of the β orbitals.

Before moving on to more specific results regarding $\hat{\mathbf{S}}^2$ and $\hat{\mathbf{L}}^2$, it will be useful to work out some general properties of single body operators operating on Slater determinants. Define

$$\hat{\mathrm{O}}^{\Sigma} \equiv \sum_i \hat{\mathrm{O}}^{i} \tag{8.1}$$

where the sum is over all coordinates and $\hat{\mathrm{O}}^{i}$ operates on coordinate $\mathbf{x}_i$. Note that Szabo and Ostlund make similar definitions (see Eqn. 2.101 of Ref. [22]). We start by showing

$$\hat{\mathrm{O}}^{\Sigma}\Psi(\mathbf{X}) = \sum_i \Psi(\mathbf{X})|_{\chi_i \to \hat{\mathrm{O}}\chi_i} \tag{8.2}$$

where $\hat{\mathrm{O}}$ is operating on orbital χ_i using an implied dummy coordinate. Thus the operator $\hat{\mathrm{O}}^{\Sigma}$ can be thought of as acting on orbitals rather than coordinates, an important distinction. Recalling that a Slater determinant can be written as

$$\Psi(\mathbf{X}) = N!^{-1/2} \sum_p^{\mathbf{P}} (-1)^{\wp(p)} \chi_{p_1}(\mathbf{x}_1)\chi_{p_2}(\mathbf{x}_2)...\chi_{p_N}(\mathbf{x}_N) \tag{8.3}$$

where the sum is over all permutations $\mathbf{P}$ of the coordinates (this gives $N!$ terms) and $\wp(p)$ counts the permutations in mapping p. We proceed

$$\begin{array}{rcl} \hat{\mathrm{O}}^{\Sigma}\Psi(\mathbf{X}) & = & \sum_i \hat{\mathrm{O}}^{i}\Psi(\mathbf{X}) \\ & = & \sum_i \hat{\mathrm{O}}^{i} N!^{-1/2} \sum_p^{\mathbf{P}} (-1)^{\wp(p)} \chi_{p_1}(\mathbf{x}_1)\chi_{p_2}(\mathbf{x}_2)...\chi_{p_N}(\mathbf{x}_N) \\ & = & N!^{-1/2} \sum_p^{\mathbf{P}} (-1)^{\wp(p)} \sum_i \hat{\mathrm{O}}^{i} \chi_{p_1}(\mathbf{x}_1)\chi_{p_2}(\mathbf{x}_2)...\chi_{p_N}(\mathbf{x}_N) \\ & = & N!^{-1/2} \sum_p^{\mathbf{P}} (-1)^{\wp(p)} \sum_i \hat{\mathrm{O}}^{p_i} \chi_{p_1}(\mathbf{x}_1)\chi_{p_2}(\mathbf{x}_2)...\chi_{p_N}(\mathbf{x}_N) \\ & = & \sum_i N!^{-1/2} \sum_p^{\mathbf{P}} (-1)^{\wp(p)} \hat{\mathrm{O}}^{p_i^{-1}} \chi_{p_1}(\mathbf{x}_1)\chi_{p_2}(\mathbf{x}_2)...\chi_{p_N}(\mathbf{x}_N) \\ & = & \sum_i \Psi(\mathbf{X})\big|_{\chi_i \to \hat{\mathrm{O}}\chi_i} \end{array} \tag{8.4}$$

where

$$\Psi(\mathbf{X})\big|_{\chi_i \to \hat{\mathrm{O}}\chi_i} = c\Psi(\mathbf{X})\big|_{\chi_i \to \chi_i'} \quad \text{and} \quad \chi_i' \equiv \frac{1}{c}\hat{\mathrm{O}}\chi_i - \frac{1}{c}\sum_{j \neq i} \chi_j \langle \chi_j | \hat{\mathrm{O}} | \chi_i \rangle. \tag{8.5}$$

Here, χ_i' is the new i^{th} orbital and is equal to $\hat{\mathrm{O}}\chi_i'$ after subtracting all the linear dependence with the remaining orbitals and normalizing (factor c). This is just a linear algebra result - see Eqn. 1.40 in Szabo and Ostlund for reference.

Writing the $\hat{\mathbf{S}}^2$ and $\hat{\mathbf{L}}^2$ operators in a useful form will greatly simplify our work. We will will show that

$$\hat{\mathbf{S}}^2 = \hbar\hat{\mathrm{S}}_z^{\Sigma} + \hat{\mathrm{S}}_z^{\Sigma}\hat{\mathrm{S}}_z^{\Sigma} + \hat{\mathrm{S}}_-^{\Sigma}\hat{\mathrm{S}}_+^{\Sigma}. \tag{8.6}$$

Only the raising and lowering operators $\hat{\mathrm{S}}_\pm \equiv \hat{\mathrm{S}}_x \pm i\hat{\mathrm{S}}_y$ and commutation rule $[\hat{\mathrm{S}}_x, \hat{\mathrm{S}}_y] = i\hbar\hat{\mathrm{S}}_z$ as described in Griffiths are used.[88] Since both $\hat{\mathbf{S}}$ and $\hat{\mathbf{L}}$ obey the same algebraic rules the proof is identical for each - just substitute $\hat{\mathbf{L}}$ for $\hat{\mathbf{S}}$.

$$\begin{array}{rcll} \hat{\mathbf{S}}^2 & = & (\hat{\mathrm{S}}_x^{\Sigma})^2 + (\hat{\mathrm{S}}_y^{\Sigma})^2 + (\hat{\mathrm{S}}_z^{\Sigma})^2 & \\ & = & \frac{1}{4}(\hat{\mathrm{S}}_+^{\Sigma} + \hat{\mathrm{S}}_-^{\Sigma})^2 - \frac{1}{4}(\hat{\mathrm{S}}_+^{\Sigma} - \hat{\mathrm{S}}_-^{\Sigma})^2 + (\hat{\mathrm{S}}_z^{\Sigma})^2 & \text{using } \hat{\mathrm{S}}_\pm = \hat{\mathrm{S}}_x \pm i\hat{\mathrm{S}}_y \\ & = & \frac{1}{2}\hat{\mathrm{S}}_+^{\Sigma}\hat{\mathrm{S}}_-^{\Sigma} + \frac{1}{2}\hat{\mathrm{S}}_-^{\Sigma}\hat{\mathrm{S}}_+^{\Sigma} + \hat{\mathrm{S}}_z^{\Sigma}\hat{\mathrm{S}}_z^{\Sigma} & \\ & = & \frac{1}{2}[\hat{\mathrm{S}}_+^{\Sigma}, \hat{\mathrm{S}}_-^{\Sigma}] + \hat{\mathrm{S}}_-^{\Sigma}\hat{\mathrm{S}}_+^{\Sigma} + \hat{\mathrm{S}}_z^{\Sigma}\hat{\mathrm{S}}_z^{\Sigma} & \\ & = & \frac{1}{2}[\hat{\mathrm{S}}_+, \hat{\mathrm{S}}_-]^{\Sigma} + \hat{\mathrm{S}}_-^{\Sigma}\hat{\mathrm{S}}_+^{\Sigma} + \hat{\mathrm{S}}_z^{\Sigma}\hat{\mathrm{S}}_z^{\Sigma} & \text{using } i \neq j \Rightarrow [\hat{\mathrm{S}}_+^{i}, \hat{\mathrm{S}}_-^{j}] = 0 \\ & = & \frac{1}{2}[\hat{\mathrm{S}}_x + i\hat{\mathrm{S}}_y, \hat{\mathrm{S}}_x - i\hat{\mathrm{S}}_y]^{\Sigma} + \hat{\mathrm{S}}_-^{\Sigma}\hat{\mathrm{S}}_+^{\Sigma} + \hat{\mathrm{S}}_z^{\Sigma}\hat{\mathrm{S}}_z^{\Sigma} & \text{using } \hat{\mathrm{S}}_\pm = \hat{\mathrm{S}}_x \pm i\hat{\mathrm{S}}_y \\ & = & -i[\hat{\mathrm{S}}_x, \hat{\mathrm{S}}_y]^{\Sigma} + \hat{\mathrm{S}}_-^{\Sigma}\hat{\mathrm{S}}_+^{\Sigma} + \hat{\mathrm{S}}_z^{\Sigma}\hat{\mathrm{S}}_z^{\Sigma} & \\ & = & \hbar\hat{\mathrm{S}}_z^{\Sigma} + \hat{\mathrm{S}}_z^{\Sigma}\hat{\mathrm{S}}_z^{\Sigma} + \hat{\mathrm{S}}_-^{\Sigma}\hat{\mathrm{S}}_+^{\Sigma} & \text{using } [\hat{\mathrm{S}}_x, \hat{\mathrm{S}}_y] = i\hbar\hat{\mathrm{S}}_z \\ & & \quad \text{or equivalently} & \\ & = & -\hbar\hat{\mathrm{S}}_z^{\Sigma} + \hat{\mathrm{S}}_z^{\Sigma}\hat{\mathrm{S}}_z^{\Sigma} + \hat{\mathrm{S}}_+^{\Sigma}\hat{\mathrm{S}}_-^{\Sigma}. & \end{array} \tag{8.7}$$

We can immediately address the first two terms of $\hat{\mathbf{S}}^2$ (and $\hat{\mathbf{L}}^2$) in Eqn. 8.6 above. It is very straight forward to show that

$$\hat{\mathbf{S}}^2 = \hbar^2(\sum_i m_i)(1 + \sum_i m_i) + \hat{\mathrm{S}}_-^{\Sigma}\hat{\mathrm{S}}_+^{\Sigma}. \tag{8.8}$$

This result becomes clear when we see

$$\hat{\mathrm{S}}_z^{\Sigma}\Psi(\mathbf{X}) = \sum_i \hbar m_i \Psi(\mathbf{X}). \tag{8.9}$$

To prove this only $\hat{\mathrm{S}}_z\chi_i = \hbar m \chi_i$ where $m = \pm\frac{1}{2}$ as described in Griffiths is needed. Since both $\hat{\mathrm{S}}_z$ and $\hat{\mathrm{L}}_z$ obey the same algebraic rules the proof is identical for each - just substitute $\hat{\mathrm{L}}$ for $\hat{\mathrm{S}}$ keeping in mind that $m = 0, \pm1, \pm2, ..., \pm l$ for $\hat{\mathrm{L}}_z$.

$$\begin{array}{rcll} \hat{\mathrm{S}}_z^{\Sigma}\Psi(\mathbf{X}) & = & \sum_i \Psi(\mathbf{X})|_{\chi_i \to \hat{\mathrm{S}}_z\chi_i} & \\ & = & \sum_i \Psi(\mathbf{X})|_{\chi_i \to \hbar m_i \chi_i} & \text{using } \hat{\mathrm{S}}_z\chi_i = \hbar m \chi_i \\ & = & \sum_i \hbar m_i \Psi(\mathbf{X}). & \end{array} \tag{8.10}$$

Amazingly, without even proceeding into further details the general results above already completely solve a large number of relevant situations. Namely, when the three terms in Eqn. 8.8 are zero the solution is trivial. We see that filled shells don't contribute to angular momentum. In the work present here we are primarily concerned with the transition metal triplet states where all the shells are filled except for 3d. For the purposes of calculating the angular momentum one only needs to consider states from that shell. These states can be understood in terms of an antisymmetric two-body function given by

$$|m_1, m_2\rangle \equiv \frac{1}{\sqrt{2}}(Y_2^{m_1}(\mathbf{r}_1)Y_2^{m_2}(\mathbf{r}_2) - Y_2^{m_2}(\mathbf{r}_1)Y_2^{m_1}(\mathbf{r}_2))$$

where Y_l^m are spherical harmonics. By applying the above relationships one can compute the proper angular momentum states. Those details are presented in Table 8.1.

Table 8.1: L and M_L for several two-body states.

L	M_L	d^2 State	d^3 State
3	3	$\vert\ 2,\ \ 1\rangle$	$\vert\ 2,\ \ 1,\ \ 0\rangle$
3	2	$\vert\ 2,\ \ 0\rangle$	$\vert\ 2,\ \ 1, -1\rangle$
3	1	$\sqrt{\frac{3}{5}}\vert\ 2, -1\rangle + \sqrt{\frac{2}{5}}\vert\ 1,\ \ 0\rangle$	$\sqrt{\frac{3}{5}}\vert\ 2,\ \ 0, -1\rangle + \sqrt{\frac{2}{5}}\vert\ 2,\ \ 1, -2\rangle$
3	0	$\sqrt{\frac{1}{5}}\vert\ 2, -2\rangle + \sqrt{\frac{4}{5}}\vert\ 1, -1\rangle$	$\sqrt{\frac{1}{5}}\vert\ 1,\ \ 0, -1\rangle + \sqrt{\frac{4}{5}}\vert\ 2,\ \ 0, -2\rangle$
3	-1	$\sqrt{\frac{3}{5}}\vert\ 1, -2\rangle + \sqrt{\frac{2}{5}}\vert\ 0, -1\rangle$	$\sqrt{\frac{3}{5}}\vert\ 1,\ \ 0, -2\rangle + \sqrt{\frac{2}{5}}\vert\ 2, -1, -2\rangle$
3	-2	$\vert\ 0, -2\rangle$	$\vert -1,\ \ 1, -2\rangle$
3	-3	$\vert -1, -2\rangle$	$\vert -2, -1,\ \ 0\rangle$
1	1	$\sqrt{\frac{2}{5}}\vert\ 2, -1\rangle - \sqrt{\frac{3}{5}}\vert\ 1,\ \ 0\rangle$	$\sqrt{\frac{2}{5}}\vert\ 2,\ \ 0, -1\rangle - \sqrt{\frac{3}{5}}\vert\ 2,\ \ 1, -2\rangle$
1	0	$\sqrt{\frac{4}{5}}\vert\ 2, -2\rangle - \sqrt{\frac{1}{5}}\vert\ 1, -1\rangle$	$\sqrt{\frac{4}{5}}\vert\ 1,\ \ 0, -1\rangle - \sqrt{\frac{1}{5}}\vert\ 2,\ \ 0, -2\rangle$
1	-1	$\sqrt{\frac{2}{5}}\vert\ 1, -2\rangle - \sqrt{\frac{3}{5}}\vert\ 0, -1\rangle$	$\sqrt{\frac{2}{5}}\vert\ 1,\ \ 0, -2\rangle - \sqrt{\frac{3}{5}}\vert\ 2, -1, -2\rangle$

8.1.2 Real Atomic Orbitals

The states given in Table 8.1 are for the standard complex spherical harmonics. However, as mentioned earlier, real wave functions are used in this work. Taking advantage of the degeneracy of the M_L states when spin orbit is not included allows for the calculation of the energy associated with a given L unambiguously. It is very straight forward to show that states given by term symbols ^3F and ^5F can be constructed to be a real single determinant as

$$^3F = |2,0\,\rangle + |-2,0\,\rangle \tag{8.11}$$

and

$$^5F = |2,1,-1\,\rangle + |-2,-1\,\rangle \tag{8.12}$$

(where normalization has been neglected). These are the states that will be looked for in Gaussian09 calculations with care taken to insure that the angular momentum states are not contaminated.

8.2 QMC methods and dependence on the trial function

To test the BFD pseudopotential with our methods, single-body calculations are done using restricted open-shell Hartree-Fock (ROHF) and unrestricted DFT with the Perdew-Burke-Ernzerhof[29, 30] (PBE) generalized gradient approximation (GGA) functional. The use of unrestricted orbitals introduces a small amount of spin contamination, however, this is generally considered to be very minimal and will be a point of testing. Comparisons between truncated triple- and quadruple-zeta Gaussian basis sets will be carried out. The truncation involves eliminating any basis function higher than d so that the possibility of angular momentum contamination is reduced. The basis sets used are those generated by BFD and can be obtained from their web site free of charge.[89] The Slater-Jastrow trial functions are constructed from the single-body orbitals derived from the Gaussian calculations. No single-body cusp conditions are required due to the use of the pseudopotential. However, the usual electron-electron cusp condition described in Sec. 5.2 will be imposed.

The Jastrow used here is that of a uniform cubic B-spline. The B-spline is partitioned with uniform knot spacings or segments and extends out to some cutoff value. The 0^{th}, 1^{st}, and 2^{nd} derivatives are continuous and go to zero at the cutoff. The B-splines used in the nucleus-electron and electron-electron Jastrows have a knot spacing of 0.5 Bohr and cutoffs of 9 and 8 Bohr respectively. These cutoffs and spacings were chosen after a significant amount of time tuning parameters so that cutoffs were not so long that regions are under-sampled and not so short that the cutoff occurred in a region of higher electron density (resulting in an increased variance). The spacing is chosen so that all important features of the Jastrow can be described.

The QMC calculations proceed as follows. Variational Monte Carlo is performed so that the B-spline parameters in the Jastrow can be optimized. This is done with modified version of a recently developed optimization method by Toulouse and Umrigar.[90, 91] After optimization is complete, DMC calculations are done at three time-step values, 0.04, 0.02 and 0.01, to verify convergence to the zero time-step limit. Localization of the pseudopotential is done by use of the variational method given by Casula in order to insure a better cancellation of localization energy errors and improved statistics.[18] Transition energies of the various states associated can then be calculated and compared.

8.3 Results

Results are present for the study of atomic transition energies in PBE-DFT and ROHF and DMC. The tables presented are designed to be somewhat self-explanatory, however, a few more words might help clear up any confusion. Comparison is made to experimental values (as given by BFD) for the 1^{st} and 2^{nd} ionization potentials and the lowest σ-excitation.[19]

The specific states studied are the ground state of Ti, which has a spin multiplicity of 3, total angular momentum $L = 3$ (^3F), and electronic configuration given by [Ar]3d^{2}4s^2. The lowest sigma excited state involves the promotion of an s-state to a d-state so that the spin multiplicity is 5, $L = 3$ (^5F), and the electronic configuration given by [Ar]3d^{3}4s^1. The ground state of the ionized Ti atom where a single electron has been removed is denoted Ti^{+1}. The removal of an s-state results in a spin multiplicity of 4, $L = 3$ (^4F) and electronic configuration [Ar]3d^2 4s^1. Finally, the ground state of an ionized Ti atom where a two electrons have been removed is denoted Ti^{+2}. The removal of the second s-state results in a spin multiplicity of 3, $L = 3$ (^3F) and electronic configuration [Ar]3d^2.

Table 8.2 presents absolute energy data for the above mentioned states using PBE-DFT and ROHF theory and bases as mentioned above. Table 8.3 gives the transition energies between the various states. Most notably, PBE-DFT gets the wrong ground state for Ti resulting in a negative value for the lowest σ-excitation. ROHF gives agreement to almost within 5 mHa. PBE-DFT does better for the 1^{st} and 2^{nd} ionization energies underestimating the first by $\sim$ 5mHa and overestimating the second by $\sim$ 15mHa. ROHF underestimates both ionization energies by $\sim$ 50 and 25mHa for the 1^{st} and 2^{nd} ionization potentials respectively.

The raw DMC energies at time-step τ=0.01 are given in Table 8.4. This data is analogous to that for the single-body results in Tab. 8.2. Time-step convergence results are given for the transition energies in Tab. 8.5 where the transition data indicates convergence has been achieved at time-step τ=0.01. Finally a summary of the converged DMC transition energy data is given in

8.6 with comparison to experiment. DMC results are not found to be strongly dependent on either single-body orbital theory or basis. The σ-excitation had the poorest agreement in being underestimated by between about 1 and 5 mHa with the ROHF trial function showing a slight advantage (all underestimated the energy). Generally speaking, however, all DMC results are found to be in reasonable agreement with experiment.

8.4 Summary and Conclusions

The single-body results for ROHF and PBE-DFT by themselves are not in very good agreement with experiment with the possible exception of the σ-excitation given by ROHF theory. Even then the result is worse than DMC in every case. Most notably, PBE-DFT gets the Ti ground state incorrectly. In all cases spin contamination is found to be very minimal. However, good agreement is found when either of these theories are used to generate single-body orbitals for use in the Slater-Jastrow trial function for DMC. DMC results are found to be weakly dependent on both the single-body theory and basis set as tested here. Moreover, it appears that the BFD pseudopotential is very suitable for application on succeeding QMC calculations.

State	Configuration	Basis	ROHF (Ha)	PBE-DFT (Ha)
Ti (^3F)	[Ar] 3d^2 4s^2	3-zeta 4-zeta	-57.7360051244 -57.7361591097	-58.1765268969 -58.1767360526
Ti (^5F)	[Ar] 3d^3 4s^1	3-zeta 4-zeta	-57.7112842540 -57.7113429640	-58.1812624443 -58.1813639005
Ti^{+1} (^4F)	[Ar] 3d^2 4s^1	3-zeta 4-zeta	-57.5314294075 -57.5320890513	-57.9299060108 -57.9307389099
Ti^{+2} (^3F)	[Ar] 3d^2	3-zeta 4-zeta	-57.0564226421 -57.0569837398	-57.4155222183 -57.4165703631

Table 8.2: Results for atomic Ti for PBE-DFT and ROHF with BFD pseudopotential. While the electron configuration given makes reference to the Argon configuration, it is understood that only the Ne core states are accounted for through the pseudopotential. Comparisons are made for truncated 3- and 4-zeta basis sets from BFD and are referenced in the main text.

Transition	Basis	ROHF	PBE-DFT	Experiment
σ-excitation Ti (^3F) → Ti (^5F)	3-zeta 4-zeta	0.0247208704 0.0248161457	-0.0047355474 -0.0046278479	0.030 Ha
1^{st} Ionization Potential Ti (^3F) → Ti^{+1} (^4F)	3-zeta 4-zeta	0.2045757169 0.2040700584	0.2466208861 0.2459971427	0.251
2^{nd} Ionization Potential Ti^{+1} (^4F) → Ti^{+2} (^3F)	3-zeta 4-zeta	0.4750067654 0.4751053115	0.5143837925 0.5141685468	0.4991

Table 8.3: Transition energies for atomic Ti for PBE-DFT and ROHF with BFD pseudopotential. Experimental numbers are included for reference. Comparisons are made for truncated 3- and 4-zeta basis sets from BFD and are referenced in the main text. Of particular note is that PBE-DFT gets the wrong ground state.

State	Configuration	Basis	DMC-ROHF (Ha)	DMC-PBE (Ha)
Ti (^3F)	[Ar] 3d^2 4s^2	3-zeta 4-zeta	-58.18216(12) -58.18114(12)	-58.18105(14) -58.18269(14)
Ti (^5F)	[Ar] 3d^3 4s^1	3-zeta 4-zeta	-58.15280(12) -58.15282(11)	-58.15542(13) -58.15441(14)
Ti^{+1} (^4F)	[Ar] 3d^2 4s^1	3-zeta 4-zeta	-57.93926(11) -57.93897(14)	-57.93959(12) -57.93952(11)
Ti^{+2} (^3F)	[Ar] 3d^2	3-zeta 4-zeta	-57.43940(10) -57.44106(12)	-57.43973(12) -57.44004(10)

Table 8.4: Results for atomic Ti for DMC using PBE-DFT and ROHF single body orbitals in the Slater-Jastrow trial function. The results given are for time step τ=0.01. Again, the BFD pseudopotential is used. The electron configuration given makes reference to the Argon configuration with the understanding that only the Ne core states are accounted for through the pseudopotential. Comparisons are made for BFD truncated 3- and 4-zeta basis (details are referenced in the main text).

	Trial function		DMC with time-step τ (Ha)		
Transition	Theory	Basis	$\tau = 0.04$	$\tau = 0.02$	$\tau = 0.01$
σ-excitation	PBE	3-zeta	0.02461(23)	0.02541(21)	0.02563(19)
	PBE	4-zeta	0.02808(25)	0.02800(18)	0.02828(20)
Ti (^3F) → Ti (^5F)	ROHF	3-zeta	0.02871(22)	0.02896(17)	0.02936(17)
	ROHF	4-zeta	0.02809(24)	0.02788(20)	0.02832(16)
1^{st} Ionization Potential	PBE	3-zeta	0.23955(24)	0.24106(20)	0.24146(18)
	PBE	4-zeta	0.24214(22)	0.24279(18)	0.24317(18)
Ti (^3F) → Ti^{+1} (^4F)	ROHF	3-zeta	0.24175(22)	0.24241(17)	0.24290(16)
	ROHF	4-zeta	0.24112(24)	0.24170(19)	0.24217(18)
2^{nd} Ionization Potential	PBE	3-zeta	0.50122(17)	0.49996(17)	0.49986(17)
	PBE	4-zeta	0.50066(19)	0.49964(16)	0.49948(15)
Ti^{+1} (^4F) → Ti^{+2} (^3F)	ROHF	3-zeta	0.50156(17)	0.50028(16)	0.49986(15)
	ROHF	4-zeta	0.49896(17)	0.49824(16)	0.49791(18)

Table 8.5: DMC time-step convergence data for transition energies of atomic Ti. The DMC Slater-Jastrow trial function uses single-body orbitals from PBE-DFT and ROHF with 3- and 4-zeta BFD basis sets that have been truncated to include orbitals no higher than d.

Transition	Basis	DMC w/ROHF	DMC w/PBE	Experiment
σ-excitation	3-zeta	0.02936(17)	0.02563(19)	0.030 Ha
Ti (^3F) → Ti (^5F)	4-zeta	0.02832(16)	0.02828(20)	
1^{st} Ionization Potential	3-zeta	0.24290(16)	0.24146(18)	0.251
Ti (^3F) → Ti^{+1} (^4F)	4-zeta	0.24217(18)	0.24317(18)	
2^{nd} Ionization Potential	3-zeta	0.49986(15)	0.49986(17)	0.4991
Ti^{+1} (^4F) → Ti^{+2} (^3F)	4-zeta	0.49791(18)	0.49948(15)	

Table 8.6: DMC time-step converged results for transition energies of atomic Ti. The DMC Slater-Jastrow trial function uses single-body orbitals from PBE-DFT and ROHF with truncated 3- and 4-zeta BFD basis sets respectively. Similar results are found for both ROHF and PBE trial functions and basis set dependence is small.

Chapter 9

Titanium Dihydride

9.1 Motivation for TiH_2

Titanium dihydride is a simple molecule with bent structure like water that can serve as a key component of potential hydrogen storage systems.[16] It turns out that the $d-$states of transition-metal atoms such as titanium are conducive to forming bonds with H_2 molecules. In fact, depending on the system, each Ti atom can bond to several intact hydrogen molecules to form what is sometimes referred to as a Kubas complex as discussed briefly in Sec. 1.2. TiH_2 represents one of the simplest systems we can study to gain insight into the d-states that give these effects. The structure and energetics of TiH_2 are studied here in some detail because it is an important building block in the hydrogen on Ti-ethylene systems that are the true focus of this thesis research.

It is important to treat systems such as TiH_2 since the $d-$ states in transition metals are strongly correlated and present inherent challenges to methods that do not address this issue directly. The QMC methods used here are especially appropriate since many-body correlation effects are implicitly built into the correlated trial functions that are optimized in the VMC calculations and used to project out the ground state in DMC. While the QMC methods used here have already demonstrated good results on atomic titanium, there are important differences in molecular systems. The present study of TiH_2 is designed to test the accuracy of our QMC methods for a small molecule directly comparable to the Ti-ethylene systems. There are two aspects of the problem that differ from the atom. One is the nature of the wave functions and the lower symmetry due to the hydrogen bonds. Here we quantify the accuracy of the nodal-surface derived from PBE-DFT single-body orbitals for this molecular system. The second aspect is that the geometry of the molecule will in general be different from that found in the density functional calculations. Thus we carry out a full minimization of the energy to find the optimal geometry within the DMC theory. This is not usually done in QMC calculations, and it is one of the most difficult parts of the work in this thesis.[44] The reason is that different symmetry states of the d-orbitals are very close in energy, and it requires extreme care to determine the energy surfaces as a function of bond lengths and angle for each symmetry. Such complete studies are not feasible for the larger Ti-ethylene-hydrogen systems presented later. This study will quantify the accuracy of the energy for the geometries found in the density functional calculations.

The work starts with PBE-DFT and Hartree-Fock (HF) studies of the potential energy surfaces of TiH_2 for the C_{2v} symmetry states. Using the single-body theory results, trial wave functions are constructed with the aid of a VMC optimized Jastrow factor. Next, DMC potential energy surfaces are constructed on configuration space grids so that optimal geometric structures can be computed within DMC and consistent with the trial functions we use. This is done by fitting a quadratic surface and sampling to estimate error bars. Finally, comparison is made between the differences arising from using single-body orbitals from PBE-DFT versus HF so that the error due to PBE-DFT geometry in DMC can be calculated. These results are then used as the basis for the final study of this research which will be presented in the next chapter.

9.2 Background

9.2.1 Experimental studies

Generally speaking, there are many experimental studies of solid-state transition metal (TM) hydrides due to their possible application to hydrogen storage. However, the focus here is specifically the ground and possibly low lying states of molecular TiH_2 which corresponds to a low temperature gas phase. Not too much experimental work has been done on this system and to the author's knowledge only experiments on molecular TiH_2 were done by Xiao, Hauge and Margrave in 1991 and Chertihin and Andrews in 1994.[92, 93] Xiao and coworkers measured both symmetric and antisymmetric stretching frequencies and intensities using a multi-surface matrix isolation spectroscopy technique. They vaporized titanium by heating a filament to 1380 - 1460°C reacting with molecular hydrogen/deuterium. Subsequently the reaction products were deposited on an inert matrix and the spectra was measured with the surface temperature of 12K. From a symmetry analysis of the modes the molecule was found to be bent. The bond angle was estimated from the intensity data and was found to be 145°. In an effort to explore possible further TiH_n chemistry, Chertihin and Andrews studied reactions of pulsed laser evaporated Ti atoms. That work served to confirm the previous work by Xiao, however, observation of additional hydride species is emphasized.

9.2.2 Previous theoretical work

Considerably more theoretical work has been done using a variety of methods. The earliest results we know of are due to Demuynck and Schaefer [94] which were published in 1980, several years before the experimental studies. Using Hartree-Fock they studied the $^3A_1$ state and found the molecular structure to be linear. Further, they find the potential energy curve to be extremely flat, varying less than 1.5 mHa from 140-179°, and with bond length 1.879Å. With such a flat potential energy curve they suggested that the molecule may appear bent in matrix experiments due to a dipole-induced dipole interaction. A single point CI calculation was also done and found to result in an energy lowering of ∼0.23 Ha. It should be noted that their CI study was limited due to computational constraints. Shortly thereafter two additional studies by Tyrrell and Youakim in 1980 and '81 were conducted.[95, 96] They compared calculations using Hartree-Fock all-electron and an Argon effective core potential (ECP) for the $^3\mathrm{B}_1$ symmetry and a lone ECP calculation for $^3\mathrm{A}_1$. They found considerably different potential energy curves from Demuynck and Schaefer, and significant differences between all electron and ECP calculations. In the all electron calculation, they found a bond angle of about 90° and 1.556 Bohr with depth of 50 mHa. The ECP calculation gave 150° and 1.704 Bohr with a well depth of 3 mHa. The followup work in 1981 studied basis effects in ECP calculations on the $^3\mathrm{A}_1$ state that suggested a more complete basis is necessary. They found that the presence of these functions resulted in an increased bonding angle. As discussed in chapter 8, this work uses a neon core pseudopotential which avoids some of the problems associated with the larger argon core.

Subsequent to the experimental work additional studies were conducted. In 1995 Kudo and Gordon [97] conducted a dedicated study of TiH_2 using all-electron State Averaged Complete Active Space Self Consistent Field Theory (SA-CASSCF) and Multi-Reference Configuration Interaction (MRCI) theory. They found that $^3\mathrm{B}_1$ state to be lower in energy than the $^3\mathrm{A}_1$ by only 0.6 mHa. The geometry of these two structures was also found to be similar where the $^3\mathrm{B}_1$ bond was 140.7° and 3.521 Bohr while $^3\mathrm{A}_1$ had a bond of 150.6° and 3.555 Bohr. The well depth of the $^3\mathrm{B}_1$ state was found to be quite shallow at 1.3 mHa. Subsequently in 1996, Fujii and Iwata conducted a study in which TiH_2 was a part.[98] This work seems a bit less careful than the previous work by Kudo. They found all the structures they studied to be linear or essentially linear. In particular, TiH_2 was found to be essentially linear with a well depth of less than 0.1 mHa.

Among the most careful work is that conducted by Ma, Collins and Schaefer [99]. They conducted all-electron Configuration Interaction Singles-Doubles and Coupled-Cluster Singles-Doubles calculations on several states of TiH_2 (and VH_2 as well). They find $^3\mathrm{B}_1$ to be the lowest energy state with $^3\mathrm{A}_1$ about 0.2 mHa above it. The geometries of these states are given by CISD theory and are 143.2° at 3.402 Bohr and 144.6° at 3.405 Bohr respectively (these numbers are with respect to the TZP+f basis). The well depth found is about 2 mHa. Finally, there is an all-electron DFT study by Platts in 2001.[100] That work uses the B3LYP functional and finds $^3\mathrm{A}_1$ to be the ground state with bond 124.6° at 3.328 Bohr.[1] We regard the CI calculations[99] as the best previous

---

[1] This is in reasonable agreement with early B3LYP test calculations I did but that are not presented as a part of my results here.

work and will use them to compare with the QMC results presented here.

9.3 Nature of the electronic states of TiH$_2$

The focus of this present chapter is the spin 1 state of TiH$_2$ with C$_{2v}$ geometric symmetry. Here, the hydrogen atoms are bound to the $4s-$ and $3d-$states of Ti through $\sigma-$bonds (see Figures 9.3a,b). This results in two unpaired electronic $d-$states so that the molecule is spin 1 in accordance with Hund's rule of maximum multiplicity. Later in Section 9.7 detailed results from PBE-DFT study of the spin 0 and spin 2 states are presented that substantiate the spin 1 system as energetically most favorable. Presently I will discuss TiH$_2$ symmetry, the Ti$-$H, bonding, and $d-$state structure with regard to both bonding and symmetry.

9.3.1 Symmetry of TiH$_2$

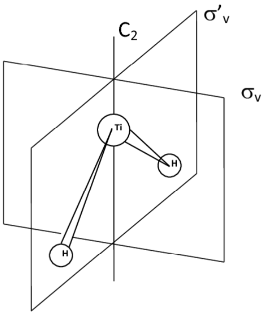

Figure 9.1: The above figure indicates the C$_{2v}$ symmetry operations and their relationship to TiH$_2$. The C$_2$ axis indicates a two-fold rotational symmetry, the σ_v and σ'_v planes indicate planes of mirror symmetry.

The TiH$_2$ molecule electronic density is invariant under the C$_{2v}$ point group symmetry operations as indicated in Figure 9.1. Here we see that TiH$_2$ has two-fold rotational symmetry about the C_2 axis and mirror symmetry about the σ_v and σ'_v planes. Thus, with the identity operation, there are four possible symmetry operations that belong to the C$_{2v}$ point group. While the electron density of the molecule is invariant under these operations, the wave function can change by a phase factor which, for real wave functions, corresponds to a change in sign. This is because the density is given by $|\Psi|^2$ where Ψ is the wave function. Therefore, given a symmetry operator $\hat{\mathrm{O}} \in \{E, \sigma_v, \sigma'_v, C_2\}$ we have $\hat{\mathrm{O}}\Psi = \pm\Psi$ so that Ψ is an eigenstate of $\hat{\mathrm{O}}$. Further, since the symmetry operators necessarily commute with the Hamiltonian (i.e. $\hat{\mathrm{O}}\hat{\mathrm{H}} = \hat{\mathrm{H}}\hat{\mathrm{O}}$ where $\hat{\mathrm{H}}$ is the Hamiltonian), the eigenstates of the Hamiltonian are simultaneous eigenstates of the symmetry operators making the symmetry of the wave function a “good” quantum number.

Given this symmetry, the sign relationship of the various states can be understood as shown in Tab. 9.1. The A$-$states (A$_1$, A$_2$) are symmetric under

	A_1	B_1	A_2	B_2
H−Ti−H	$\begin{array}{c\|c} + & + \\ \hline + & + \end{array}$	$\begin{array}{c\|c} + & + \\ \hline - & - \end{array}$	$\begin{array}{c\|c} + & - \\ \hline - & + \end{array}$	$\begin{array}{c\|c} + & - \\ \hline + & - \end{array}$

Table 9.1: Wave function symmetries for the C_{2v} point group. The TiH_2 at left indicates the molecular orientations with respect to the states and the vertical and horizontal lines in the sign tables indicate the σ_v and σ_v' mirror symmetry planes respectively with the point of intersection corresponding to the C_2 rotation symmetry axis. The A−states (A_1, A_2) are symmetric under rotation about the C_2 axis while the B−states are antisymmetric. The 1−states (A_1, B_1) are symmetric under mirroring about the σ_v plane while the 2−states are antisymmetric.

rotation about the C_2 axis while the B−states are antisymmetric. The 1−states (A_1, B_1) are symmetric under mirroring about the σ_v plane while the 2−states are antisymmetric.

	A_1	B_1	A_2	B_2
A_1	A_1	B_1	A_2	B_2
B_1	B_1	A_1	B_2	A_2
A_2	A_2	B_2	A_1	B_1
B_2	B_2	A_2	B_1	A_1

Table 9.2: C_{2v} symmetry multiplication table.

As will be seen, atomic-like d−states play an important role in TiH_2. Thus it is important to understand the d−states in terms of the above mentioned symmetries. The atomic d−states are actually spherical harmonics which are complex; however, by considering linear combinations of the spherical harmonics they can be transformed into real counterparts. Using the wave function sign symmetries outlined in Tab. 9.1, the symmetry of the d−states can be straightforwardly assigned as shown in Fig. 9.2. Given these results we are prepared to understand the details of TiH_2

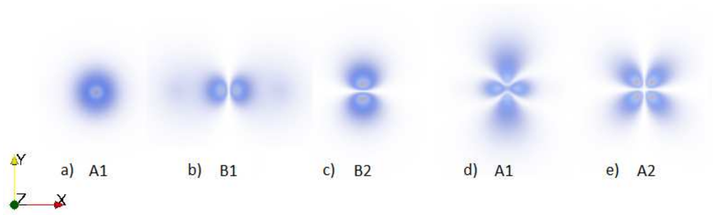

Figure 9.2: Real spherical harmonics for d-states. For reference, the TiH_2 molecule is aligned on the yz-plane with its C_2 axis aligned to the z-axis. The conventional m value for the real functions are: (a) $m = 0$ (b) $m = 1$ (c) $m = -1$ (d) $m = 2$ (e) $m = -2$.

9.3.2 Bonding and $d-$states in TiH_2

It will prove somewhat insightful to study some of the detailed results from a qualitative point of view so that the physics of the TiH_2 problem can be better understood. Consider the bonding states of the TiH_2 ground-state in PBE-DFT theory which is found to be bent. The upper occupied single-body orbitals can be seen in Fig. 9.3. In Fig. 9.3a we see an atomic Ti $4s-$state hybridized (by way of pinched orbital node) into a $\sigma-$bond state which, due to electron spin pairing, accounts for one electron in each of the Ti$-$H bonds. The other two $\sigma-$bond electrons come from a hybridized Ti $3d-$state through exaggeration/suppression of the orbital lobes. The states are spin paired with A_2 and B_2 symmetry respectively and so cannot affect the wave function sign under symmetry transformations. These bond states are lower in energy than the unpaired $d-$states by about 2-3 mHa.

Concerning the energy spacing of the single-body states in PBE-DFT, the single-body $\sigma-$bond states are lower in energy than the two unpaired 3d states by about 2 - 3 mHa. The two unpaired $d-$states are less than 0.4 mHa apart and the homo-lumo $d-$state energy gap is 0.15 - 1.5 mHa. The $d-$state degeneracy is broken due to a lack of spherical symmetry. Still, upon inspection, the unpaired d-states look fairly atomic like with some noticeable distortion due to the bonding (in some cases). The two $d-$states are occupied from the four remaining $d-$states that are not involved in the bonding so that as many as 6 occupations are possible (this is born out in UHF calculations and will be discussed later in Sec. 9.7). Consequently, it is expected that there are low lying excited states but the precise ground state symmetry is not entirely obvious.

9.3.3 $d-$state occupation in TiH_2

Earlier in this section it was mentioned that 6 $d-$state occupations were favorable given the 4 $d-$states that are not involved in the bonding. First it should be noted how the atomic $d-$states, which are the spherical harmonics, are understood in terms of C_{2v} symmetry. The spherical harmonics are complex; however, by considering linear combinations, they can be transformed into real counterparts. The relationship between symmetry states of C_{2v} and atomic $d-$states can be seen in Fig. 9.2. Upon inspection it is clear that $\sigma-$bond state shown in Fig. 9.3b has symmetry B_2. Using the remaining 4 possible d-states, 2 of which can be occupied, allows for the 6 favorable $d-$state occupations listed in Tab. 9.3 to be determined. In Sec. 9.7 more will be said in regard to these occupations.

9.3.4 Approaching linear TiH_2

A final but important point needs to be made in regard to TiH_2 as the molecular structure approaches linear. Linear TiH_2 has $D_{\infty h}$ point group symmetry where

(a) HOMO spin paired A_1 $\sigma-$bond (b) HOMO spin paired B_2 $\sigma-$bond

(c) HOMO spin unpaired B_1 $d-$state (d) HOMO spin unpaired A_1 $d-$state

Figure 9.3: Four highest HOMO states of TiH_2 in energy order. Blue and red contrast positive and negative regions respectively. Specifically, these are slices of the molecular orbitals where the molecular plane is identical to the slice plane in Figures (a) and (b). These single-body molecular orbitals were derived from the ground-state PBE-DFT calculations with a 4-zeta basis and BFD pseudopotential for Ti. (a) Top-left. Shows a Ti $4s-$state hybridized into a $\sigma-$bond state where the $4s-$orbital node is pinched. The state is spin paired with A_1 symmetry. (b) Top-right. Shows a Ti $3d-$state, normally associated with $m = \pm 1$ with respect to the linear molecule axis (if the bond were opened up to 180°), hybridized into the other $\sigma-$bond state through exaggeration/suppression of the Ti $d-$orbital lobes. The state is spin paired with B_2 symmetry. (c) Bottom-left. Is an unpaired molecular orbital with B_1 symmetry and similar to an atomic $3d-$state of Ti with $m = \pm 2$ relative to the *linear* molecule axis. (d) Bottom-right. Is the other unpaired molecular orbital but with A_1 symmetry and similar to an atomic $3d-$state of Ti with $m = 0$ relative to the *linear* molecule axis (if the bond were opened up to 180°).

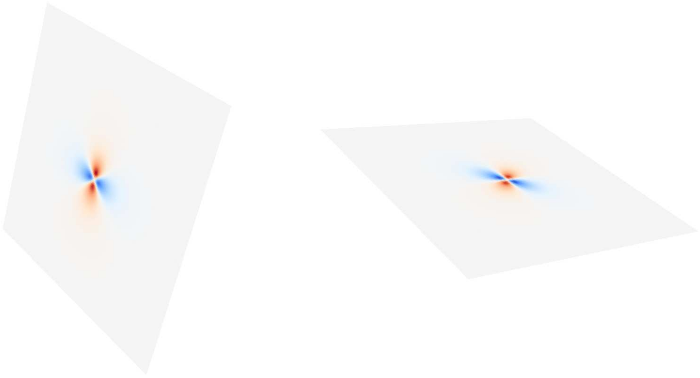

(a) LUMO A_1 $d-$state (b) LUMO A_2 $d-$state

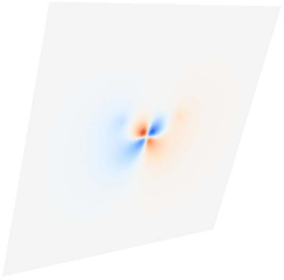

(c) LUMO σ^*-bond B_2 state

Figure 9.4: Three lowest LUMO states of TiH_2 in energy order. Blue and red contrast positive and negative regions respectively. Specifically, these are slices of the molecular orbitals where TiH_2 is oriented identical to Fig. 9.3. The states are derived from the same calculations as in Fig. 9.3 as well. (a) Top-left. Shows an unoccupied molecular orbital with A_1 symmetry and similar to an atomic $3d-$state of Ti with $m = \pm 2$ relative to the *linear* molecule axis. (b) Top-right. Shows an unoccupied molecular orbital with A_2 symmetry and similar to an atomic $3d-$state of Ti with $m = \pm 1$ relative to the *linear* molecule axis. (c) Bottom. This state is significant in that it shows an atomic-like $d-$state hybridized into an anti-bonding σ^*-state with B_2 symmetry.

Wave Function Symmetry	Orbital Symmetry	Number States
A_1	A_1, A_1	1
A_2	A_1, A_2	2
B_1	A_1, B_1	2
B_2	A_2, B_1	1

Table 9.3: Favorable d-state occupations for TiH_2. Give five d-states there are 10 possible occupations of two of those states. However, because the d-state with B_2 symmetry participates in the bonding of the hydrogen atoms, only four states remain to occupy the unpaired states. This allows for the 6 possible favorable occupations listed.

C_∞ axis is orthogonal to the C_2 axis of bent TiH_2. Upon considering the transformation of $d-$states under $D_{\infty h}$ symmetry it becomes clear that the electronic states of the linear molecule should be degenerate and correspond to the $^3\Delta_g$ symmetry in $D_{\infty h}$.

Generally speaking, it is not hard to see how the $d-$state occupations described above can become degenerate as the TiH_2 bond angle approaches 180°. First, consider the transformations of the individual $d-$states under various symmetry operations. In doing this I will refer to the $m-$value of the $d-$state where the $z-$axis is aligned to the linear (C_∞) axis as opposed to the C_2 axis of the usual bent molecule. The usual convention for describing the $m-$value will be used so that the real part of the spherical harmonic is considered $+m$ and the imaginary part $-m$. The A_1 $m = 0$ state is invariant under rotation about the C_∞ axis. The A_1 $m = 2$ state becomes B_1 $m = -2$ under 45° rotation about the C_∞ axis. Finally, the A_2 $m = 1$ states becomes B_2 $m = -1$ under 90° rotation about the C_∞ axis. These relationships are summarized in Tab. 9.4. With these relationships in place it becomes straightforward to see the degeneracy relationships when two unpaired $d-$states are occupied. In short, state A_1 and B_1 can become degenerate and states A_2 and B_2 can become degenerate as the TiH_2 molecule approaches linear geometry. The detailed results of this analysis are presented in Tab. 9.5. These degeneracies are apparent in the results that will be present later and verify the $d-$state behavior in the limit of linear structure. Finally, it should be noted that higher excitations can involve other kinds of unpaired orbitals (e.g. $4p-$states) but the arguments are the same.

9.4 Single-Body Methods used for TiH_2

This work employ the DMC method to project out the fixed-node ground state energy for several states and geometries of the TiH_2 system to determine the optimal DMC geometry with respect to symmetry. The form of the trial functions used here are the Slater-Jastrow form where the Slater determinant is

$d-$state transformation under rotation about C_∞	Rotation angle
A_1 $(m = 0)$	Invariant
A_1 $(m = 2) \leftrightarrow \mathrm{B}_1$ $(m = -2)$	45°
A_2 $(m = 1) \leftrightarrow \mathrm{B}_2$ $(m = -1)$	90°

Table 9.4: This table presents how single $d-$states with C_{2v} symmetry transform under rotations about the limiting linear TiH_2 molecular axis (C_∞ axis for $\mathrm{D}_{\infty h}$ symmetry). The A_1, B_1, A_2, B_2 states are the usual C_{2v} states of bent TiH_2, however, the $m-$values are those where the $z-$axis is aligned to the C_∞ axis of the linear molecule.

Overall wave function symmetry	$d-$states transformation under rotation about C_∞	Rotation angle
B_1	A_1, B_1 $(2, -2)$ A_2, B_2 $(1, -1)$	Invariant
$\mathrm{A}_1 \leftrightarrow \mathrm{B}_1$	A_1, A_1 $(0, 2) \leftrightarrow \mathrm{A}_1$, B_1 $(0, -2)$	45°
$\mathrm{A}_2 \leftrightarrow \mathrm{B}_2$	A_1, A_2 $(0, 1) \leftrightarrow \mathrm{A}_1$, B_2 $(0, -1)$ A_1, A_2 $(2, 1) \leftrightarrow \mathrm{A}_1$, B_2 $(2, -1)$ B_1, B_2 $(-2, -1) \leftrightarrow \mathrm{B}_1$, A_2 $(-2, 1)$	90°

Table 9.5: This table presents how two $d-$states with C_{2v} symmetry transform under rotations about the limiting linear TiH_2 molecular axis (C_∞ axis for $\mathrm{D}_{\infty h}$ symmetry). The A_1, B_1, A_2, B_2 states are the usual C_{2v} states of bent TiH_2, however, the $m-$values are those where the $z-$axis is aligned to the C_∞ axis of the linear molecule. The overall wave function symmetry can be seen to be the product of the symmetries of the two unpaired $d-$states (see Table 9.2 above).

constructed of single-body orbitals from either PBE-DFT or Hartree-Fock theory. Thus, before the QMC calculations can be done a number of single-body calculations must be conducted. By comparing DMC results from PBE-DFT and HF it can be established how sensitive the results are to the single-body theory used for the trial function. This is done in two ways. First, by comparing DMC potential energy curves and optimal DMC geometry. Second, because it is desirable to use the optimal geometry that comes out of the single-body theory we can establish what the error in DMC due to geometry is. All of this entails a fair number of single-body calculations.

The focus of the work is the triplet states of TiH_2. Prior to focussing on these states, calculations were done on the singlet and quintuplet states to show that the triplet state is indeed lowest. This was done in PBE-DFT theory only. However, no further QMC testing of these states is done since a previous study has already shown this to be the case.[97]

The triplet state calculations done here can easily result in several symmetry states for each geometry. Yet, each DFT/HF calculation gives but one result when and if convergence is achieved. Thus, conducting a single DFT/HF calculation at each geometry is insufficient to determine the ground state or low lying excited state ordering of the system for a given theory with confidence. By conducting many calculations, each with different initial conditions, several stationary states can generally be found. Combining multiple initial conditions with multiple geometries results in patterns that make the potential energy surface for several symmetries apparent. The Gaussian09[101] code was used to find the single-body orbitals that are used later in my QMC calculations. The code allows for several possible methods for constructing an initial guess. I use the orbitals that result from diagonalizing the Harris functional.[102] It is then possible to provide user-defined initial guess orbital occupations to be used in the main calculation. By supplying a variety of trial occupations I am able to find several eigenstates and generate the surfaces presented later in Sec. 9.7. It should be noted that the symmetry of the trial occupation may differ from the final state for which the calculation becomes self-consistent so all the final states were rechecked. This method produces not only ground state results for each symmetry, but also excited states.

It is recognized that DFT is a ground state theory and only the ground state of the system is considered consistent with the Hohenberg-Kohn postulates although higher states may be indicative of relevant excitations especially those close to the ground state. The calculations done here are unrestricted open shell. It is also recognized that this is a source of spin contamination because the spatial part of the spin-paired (up and down) orbitals do not exactly match. However, the amount of spin contamination of the single body calculations was found to be very small. Since we are mainly concerned with the potential energy surface of TiH_2 where spin and symmetry are constant, it is expected that this error will be somewhat uniform and not effect results in a significant way.

9.5 DMC Geometry Optimization of TiH_2

Conducting a DMC optimization of TiH_2 is one of the main goals of this present study. It should be noted in advance that this is not typically done and represents a challenge in and of itself. The main idea is to conduct DMC calculations on nine points in configuration space for the symmetries of interest and then fit a quadratic surface to that data. The nine geometries studied have bond angle 110°, 135° and 160° each with bond length 3.0, 3.3 and 3.6 Bohr. See Fig. 9.5 for an illustrative example of the grid and typical surface fit. This results in a grid that is fairly well placed so that the minimum is not too far from the center. The symmetries studied are $^3B_1$, $^3A_1$, $^3A_2$. The focus is really on the $^3B_1$ and $^3A_1$ states, the $^3A_2$ is run as a check to make sure that there are no unexpected energy reordering going on. State $^3B_2$ has been specifically neglected because in both the HF and PBE-DFT it was noted that another state of the same symmetry is near by and is probably not well represented by a single-determinant trial function.

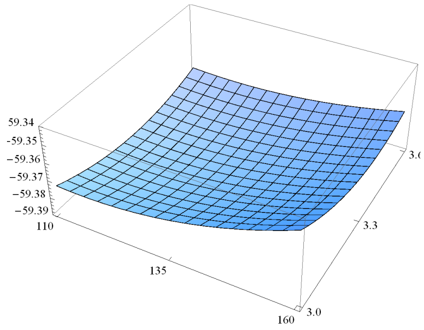

Figure 9.5: Pictured above is an example of a quadratic surface fit to 9 points. Namely, for each bond angle 110°, 135°, 160° bond lengths 3.0, 3.3 and 3.6 Bohr bond lengths are studied. This results in a function $E(\theta, r)$ satisfying $E(\theta_i, r_i) = E_i$ for $i = 1..9$ that can be minimized.

While fitting a quadratic surface is in principle straight forward, the energies that are being fit all have error bars. This results in some ambiguity regarding what the proper parameterization of the fit curve is. This ambiguity actually allows for establishing error bars on the optimal geometry and energy. To do this, the grid energies are each sampled from a normal distribution centered on the expected energy and with a standard deviation matching the error bars of the DMC results. This method certainly has limitations in that if the error bars are too big then almost any quadratic surface will fit with reasonable probability. However, with sufficiently small error bars, the fit becomes more restricted so that the likely curves are reasonably similar and all have a minimum near one another. In this work an error bar of 0.2 mHa is required to accomplish a reasonable fit. Finally, this allows for establishing optimal geometries where the bond angles, bond lengths and energies all have appropriate error bars.

9.6 Calculation Details

The calculations conducted here follow many of the procedures in the previous studies only with a few details changed. The Burkatzki-Filippi-Dolg (BFD) norm-conserving non-local pseudopotential [19] with Neon core is used for titanium and the standard Coulomb potential is used for hydrogen. The reduction in electrons is almost 50% and thus results in approximately a 5 fold reduction in computer time for all the calculations. The single-body calculations used quadruple-zeta basis sets for both Ti and H. The basis and the pseudopotential for Ti were obtained from the website maintained by BFD.[89] The H basis is the correlation consistent basis due to Dunning[66], aug-cc-pVQZ, which includes diffuse and polarization functions and was obtained from the Gaussian09 code. The single-body radial functions are transformed to a B-spline real space grid for QMC calculations. The standard fixed-node DMC implementation in the QMCPACK code [53] is used with the only modification being the Casula[18] variational treatment of the non-local part of the pseudopotential which is described in Sec. 4.4. The Jastrows used here are of the cubic B-spline form and are only used to satisfy the cusp conditions of the hydrogen electron-proton interaction and the cusp of the electron-electron interaction occurring between electrons of opposite spins. The Pauli exclusion principle generally keeps electrons of the same spin apart so that no cusp condition needs to be satisfied for that case. The resulting trial functions thus have a fairly uniform localization error since the electron-ion Jastrows used are short ranged. Avoiding the VMC optimization in this case actually serves as a significant advantage since VMC optimization can result in some variability in both the localization error and time step error of the final trial wave function DMC projection. A time-step of 0.2 is used throughout these calculations. The main point of these calculations is not to get an exactly converged result but rather to see what is going on with a DMC optimization and get results that are reflective of an exact converged result. So if the optimization error is different by a mHa (which would probably be an over estimation) that is within reason. We compare formation energies of the converged results so that this error is quantified in that regard. Individual calculations are run so that an error bar of 0.1 to 0.2 mHa is obtained for the purpose of producing a meaningful quadratic fit.

9.7 Results

The figures and tables in this section are designed to be somewhat self explanatory. All the work uses the BFD pseudopotential for Ti and the Coulomb potential for H. All single body calculations are done with BFD 4-zeta basis for Ti and the aug-cc-pVQZ basis for H. The work starts by comparing the TiH_2 singlet, triplet, and quadruplet in PBE-DFT to verify that indeed the ground state of the system is found to be triplet (as the literature suggests). Bond lengths were optimized for energy at each bond angle. Several initial conditions were attempted so as to find any states that might be lower in energy. The potential energy curves for the singlet and quintuplet states found are presented in Figs. 9.6 and 9.7. The optimal energies for each of the four C_{2v} triplet states is given in Tab. 9.7. Table 9.6 shows the relative energy for the lowest of singlet and quintuplet state with respect to the triplet state. With this starting point the work focuses on the triplet states of TiH_2.

Spin	Relative Energy (mHa)
2	87.03
0	14.03
1	0.00

Table 9.6: Relative PBE-DFT energy of the lowest state for each spin with respect to the triplet state.

At this point comparison is made between PBE-DFT and UHF for the TiH_2 triplet states. The respective potential energy curves for PBE-DFT and UHF are given in Figs. 9.8 and 9.10. Again, many initial conditions were used to look for states. This resulted in the numerous states that are seen in the UHF plot. Also, the optimal bond length at each bond angle is also given for PBE-DFT and UHF in Figs. 9.9 and 9.11 respectively. UHF gives a linear molecule for the ground state. While PBE-DFT gives a bent geometry. Previous experiments and other researchers have found a bent structure as discussed above. The optimal PBE-DFT geometries is given in Table 9.7.

wave function Symmetry	$d-$state Symmetries	Bond Angle	Bond Length	DFT-PBE Energy	DMC Energy
$^3A_1$	A_1 A_1	121.5567°	3.3116	-59.3833589988	-59.33132(24)
$^3B_1$	B_1 A_1	119.1401°	3.3080	-59.3849442432	-59.33144(24)
$^3A_2$	A_1 A_2	121.5200°	3.3537	-59.3743525255	-59.32644(26)
$^3B_2$	B_1 A_2	116.4341°	3.3586	-59.3717493232	

Table 9.7: Optimal geometry and energies for in PBE-DFT and DMC with PBE-DFT trial functions. The d-state symmetries are those of the unpaired d-orbitals. It can be seen that these symmetries result in the overall wave function symmetry using Tab. 9.2. Energies and bond lengths are in atomic units while the bond angles are in degrees. It should be noted that all of the geometries are similar, around 120° and 3.3 Bohr. The optimal energies of the two lowest states, $^3A_1$ and $^3B_1$, are less than 1.6 mHa apart.

Next, DMC results are given for trial functions with single-body orbitals derived from PBE-DFT and UHF. Potential energy curves are given for the $^3A_1$, $^3B_1$ and $^3A_2$ states for PBE-DFT and UHF trial functions in figures 9.12

Trial Function	wave function Symmetry	Angle (Deg)	Length (Bohr)	DMC Energy (Ha)
PBE	$^3A_1$	135.2(05)°	3.381(4)	-59.3326(3)
	$^3B_1$	133.5(06)°	3.384(4)	-59.3324(3)
	$^3A_2$	138.2(13)°	3.449(7)	-59.3271(2)
UHF	$^3A_1$	145.3(10)°	3.438(5)	-59.3318(2)
	$^3B_1$	142.9(09)°	3.418(5)	-59.3323(2)
	$^3A_1$	145.2(12)°	3.473(6)	-59.3282(2)

Table 9.8: Optimal DMC geometry and energies for $^3A_1$, $^3B_1$ and $^3A_2$. See Sec. 9.5 for a description of the method used to derive this data.

and 9.13 respectively. These results are derived by the quadratic fit method described above in Sec. 9.5. A summary of the optimal DMC energies and geometries for each of the states investigated is given in Table 9.8. Comparing the DMC results in Tables 9.8 and 9.7 it is seen that using the PBE-DFT geometry for DMC calculations gives an energy that is within approximately 1.5 mHa of the optimal DMC geometry. It was noted that the results here were not thoroughly converged. The DMC formation energy for TiH_2 found here is -10.04(4) mHa. This compares well to the converged result given in the next chapter of -12.60(22) mHa. Of note is that PBE-DFT over estimates this energy as -40.28 mHa while UHF underestimates it at -3.00 mHa.

9.8 Summary and Conclusions

This study presents a comparison of PBE-DFT and UHF derived trial functions in the DMC paradigm. While the PBE-DFT and UHF theory themselves give very different results for the TiH_2 structure and formation energies, the DMC results are very similar. Both trial functions give a bent molecule, however, the UHF trial function produces a geometry that is 10° closer to the $145\pm5°$ experimental number than a PBE-DFT trial function gives. The $^3A_1$ and $^3B_1$ states are almost degenerate, in general agreement with previous work that found $^3B_1$ to be lowest by only ~ 0.2 mHa. The difference in DMC energies is less than 2 mHa for the two trial functions from UHF and PBE-DFT suggesting that the fixed node error is small and of this order. We conclude that the DMC calculations provide the accuracy needed for the studies of hydrogen binding on Ti-ethylene molecules.

As mentioned from the outset, it is difficult to conduct a DMC optimization on complex molecules with many degrees of freedom. It is desirable, therefore, to use PBE-DFT optimized geometries for the DMC calculations moving forward. Here the error in using PBE-DFT geometry was found to be approximately 1.5 mHa. This is acceptable, especially since this is a variational quantity where there is always at least a partial cancellation of error. Also, while it might appear that the DMC with PBE-DFT trial function produced a slightly inferior geometry, it should be noted that the absolute energies given by the PBE-DFT trial function were actually lower than the UHF trial function for the two lowest states. Thus in the next stage of this thesis research PBE-DFT trial functions will be used exclusively.

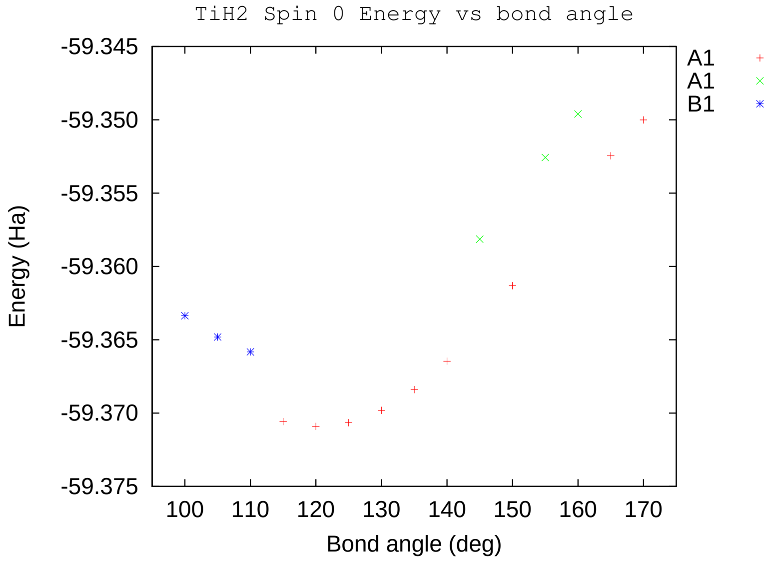

Figure 9.6: PBE-DFT optimal energy results for the TiH_2 singlet states with respect to bond angle. For each bond angle, the optimal energy is given for the state found. These calculations were done with a BFD Ti 4-zeta basis and pseudopotential while hydrogen uses a Coulomb potential and aug-cc-pVQZ basis. The optimal singlet state is found to be $^1A_1$ with geometry 120.226° and 3.290 Bohr bond length. The optimal energy is -59.37091 Ha which is found to be 14.03 mHa higher than the PBE-DFT triplet ground state.

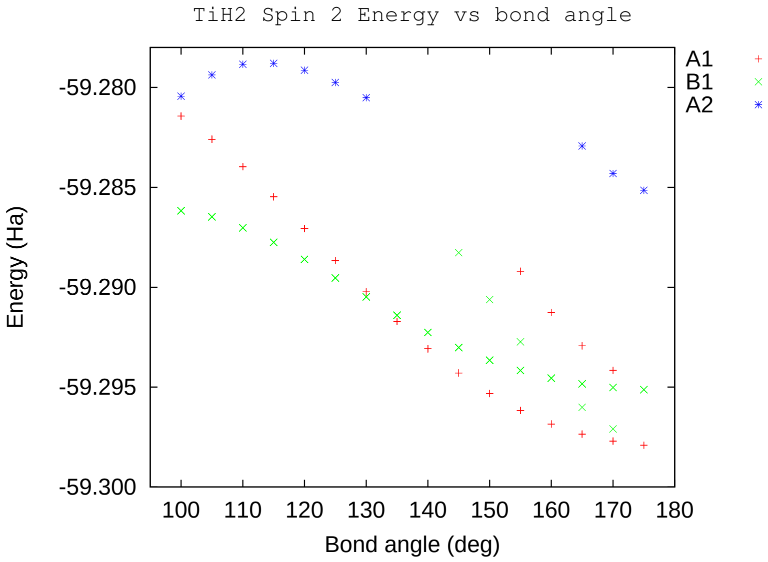

Figure 9.7: PBE-DFT optimal energy results for the TiH_2 quintuplet states with respect to bond angle. For each bond angle, the optimal energy is given for the state found. These calculations were done with a BFD Ti 4-zeta basis and pseudopotential while hydrogen uses a Coulomb potential and aug-cc-pVQZ basis. The optimal quintuplet state is found to have a linear geometry with bond length of 3.534 Bohr. The optimal energy is -59.29791 Ha which is found to be 87.03 mHa higher than the PBE-DFT triplet ground state.

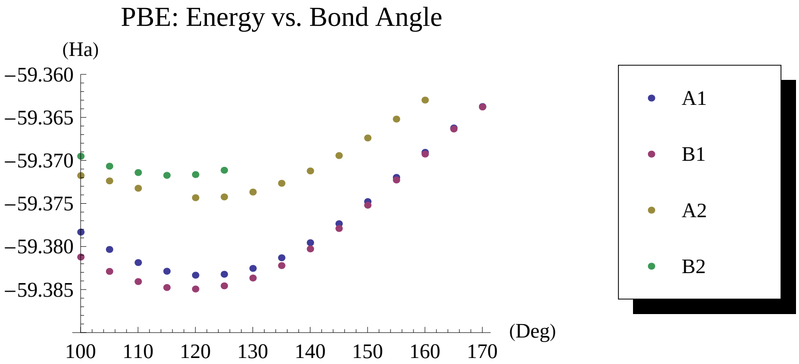

Figure 9.8: PBE-DFT optimal energy results for the TiH_2 triplet states with respect to bond angle. For each bond angle, the optimal energy is given for the state found. The optimal bond length for each state and angle can be found in Fig. 9.9. These calculations were done with a BFD Ti 4-zeta basis and pseudopotential while hydrogen uses a Coulomb potential and aug-cc-pVQZ basis. The optimal triplet state is found to be $^3B_1$ with geometry 119.1401° and 3.3080 Bohr bond length. The optimal energy is -59.38494 and is ground state.

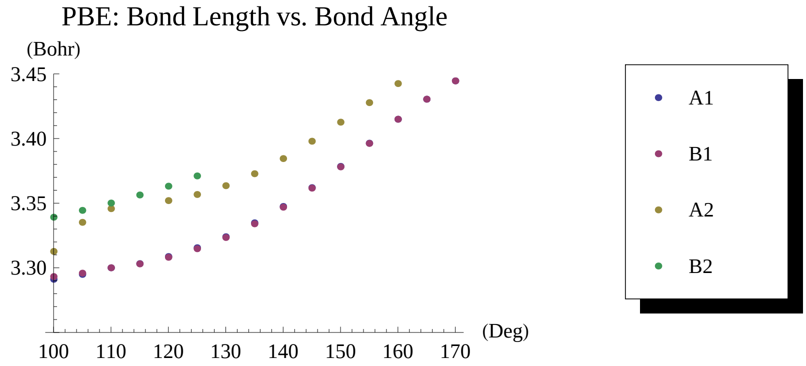

Figure 9.9: PBE-DFT optimal bond length results for the TiH_2 triplet states with respect to bond angle. For each bond angle, the optimal bond length is given for the state found. The associated optimal energy for each state and angle can be found in Fig. 9.8. These calculations were done with a BFD Ti 4-zeta basis and pseudopotential while hydrogen uses a Coulomb potential and aug-cc-pVQZ basis.

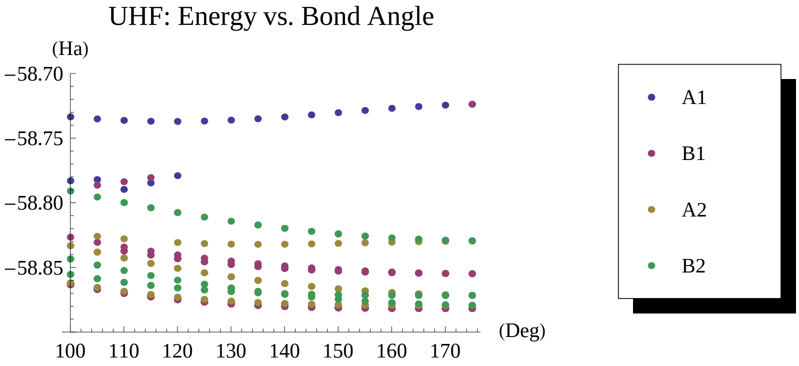

Figure 9.10: UHF optimal energy results for the TiH_2 triplet states with respect to bond angle. For each bond angle, the optimal energy is given for the state found. The optimal bond length for each state and angle can be found in Fig. 9.11. These calculations were done with a BFD Ti 4-zeta basis and pseudopotential while hydrogen uses a Coulomb potential and aug-cc-pVQZ basis. The optimal UHF triplet state is found to be linear.

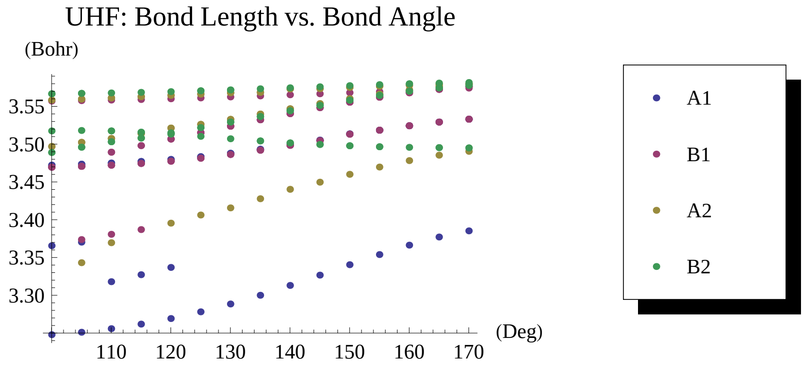

Figure 9.11: UHF optimal bond length results for the TiH_2 triplet states with respect to bond angle. For each bond angle, the optimal bond length is given for the state found. The associated optimal energy for each state and angle can be found in Fig. 9.10. These calculations were done with a BFD Ti 4-zeta basis and pseudopotential while hydrogen uses a Coulomb potential and aug-cc-pVQZ basis.

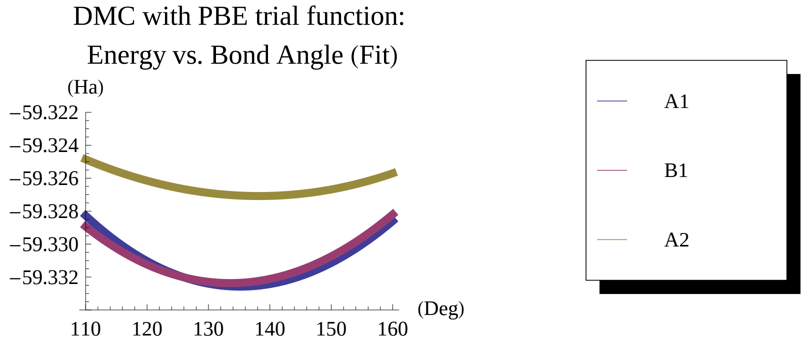

Figure 9.12: DMC results for Slater-Jastrow trial function with PBE-DFT single-body orbitals. The curves are the result of a quadratic surface fit for nine points on a configuration space grid as described in Sec. 9.5. The thickness of the plot lines are indicative of the error bars. All calculations employed the BFD Ti pseudopotential and H Coulomb potential. The basis sets used in PBE-DFT were the BFD 4-zeta basis for Ti and the aug-cc-pVQZ basis for hydrogen. Radial functions were transformed to a B-spline grid for the QMC calculations. Optimal energy and geometry for the $^3A_1$ state is -59.3326(3) Ha with bond 135.2(5)° and 3.381(4) Bohr while the optimal $^3B_1$ structure is -59.3324(3) Ha with bond 133.5(6)° and 3.384(4) Bohr. While the lowest state is found to be $^3A_1$, the energies are within the error bars.

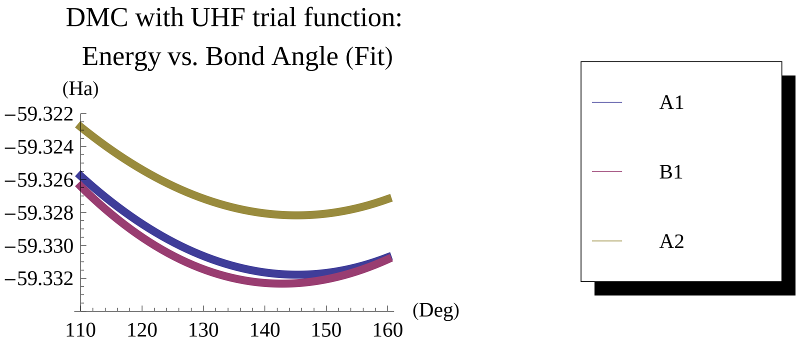

Figure 9.13: DMC results for Slater-Jastrow trial function with UHF single-body orbitals. The curves are the result of a quadratic surface fit for nine points on a configuration space grid as described in Sec. 9.5. The thickness of the plot lines are indicative of the error bars. All calculations employed the BFD Ti pseudopotential and H Coulomb potential. The basis sets used in UHF were the BFD 4-zeta basis for Ti and the aug-cc-pVQZ basis for hydrogen. Radial functions were transformed to a B-spline grid for the QMC calculations. Optimal energy and geometry for the $^3A_1$ state is -59.3318(2) Ha with bond 145.3(1.0)° and 3.438(5) Bohr while the optimal $^3B_1$ structure is -59.3323(2) Ha with bond 142.9(9)° and 3.418(5) Bohr. While the lowest state is found to be $^3B_1$, error bars are almost touching.

Chapter 10

Hydrogen on Titanium-Ethylene

As mentioned in the introduction, there is great interest in systems that exhibit reversible hydrogen storage (HS) properties that can result in practical applications for energy storage and transportation. However, many of the proposed systems, while promising, can be challenging to model so that insight might be more easily gained since they involve a larger number of atoms such as with metal-organic-framework (MOF) and fullerene systems. From the outset of this thesis research the idea of a hydrogen complex on a Ti-ethylene sorbent as described by Durgun et al. [16] has seemed to be an elegant system that captures physics and chemistry that can result in energetics suitable for reversible hydrogen adsorption. In particular, the small ethylene system allows for titanium to bond in a way similar to Ti on a C_{60} fullerene (see Fig. 10.1). The reduced system makes study of HS considerably less expensive while still allowing for relevant results. As it turns out, this area of research is currently very active and the clear pictures and results presented by Durgun et al. has proven to influence over 75 papers including some experiments. In fact, a paper published just this August 2010 [103] is very complementary to the results presented below.

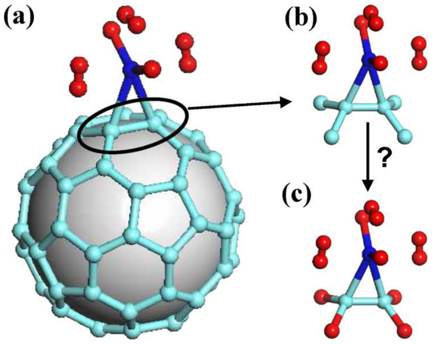

Figure 10.1: This figure is replicated from the Durgun et al., 2006. The atoms are color coded such that blue, cyan, red indicate atoms Ti, C, H respectively. (a) Shows Ti-C_{60} with a hydrogen about the Ti atom. (b) Shows the local Ti-C_{60} structure. (c) Shows the analogous $TiH_2C_2H_4{\cdot}3H_2$.

10.1 Background

10.1.1 Experimental Work

While a number of reaction dynamics studies have been performed on transition-metal (TM) ethylene structures,[104] only recently has hydrogen binding on Ti-ethylene been studied experimentally. Recently, there have been a couple experiments specifically testing hydrogen adsorption on Ti-ethylene that were conducted by Phillips and Shivaram.[105, 106] In 2008 they published results demonstrating 12% uptake of H_2 by weight in near vacuum conditions. They laser ablated Ti in ethylene gas and used a surface accoustic method to measure the mass of molecules. By comparing uptake of H_2 and D_2 (two deuteriums) they were able to confirm their results. Interestingly, they found no clustering of Ti down to the 5 nm scale. It should be noted that they also conducted a transmission electron microscope analysis of Ti clustering and found none down to 5 nm. However, in a subsequent study published in 2009 they showed that hydrogen uptake was reduced as the pressure increased. In fact, they found that pressures exceding 0.13 atm resulted in degraded uptake and increased clustering.

10.1.2 Theoretical Work

The idea of modeling Ti-fullerene hydrogen adsorption using Ti-ethylene is not too far removed from earlier work regarding titanium decorated carbon nanotubes (CNT) by Yildirim and Ciraci in 2005.[107] That work used PBE-DFT and found that a maximum of $4H_2$ molecules per Ti atom could be added with energetics favorable to reversible adsorption. Further they found that the bonding mechanism of Ti to the CNT was very similar to the Dewar mechanism that will be discussed shortly in Sec. 10.2. Further related work has pursued studies of transition-metals on benzene and organic materials. The work by Durgun et al. primarily studies hydrogen complexes on 2 Ti atoms per ethylene. This model is capable of binding up to 10 H_2 molecules with half on each of the two Ti atoms. This results in as much as ~14% hydrogen storage by weight which exceeds the hydrogen concentration of water. Molecular dynamics simulations ranging in temperature from 300-800K showed that the storage was reversible. They also discussed Ti dimerization (clustering), the impact on storage capacity and possible means to circumvent clustering.

Later in 2007, Zhou et al. (same group as Durgun et al.) conducted further work on TM-ethylene and related structures.[108] That work included PBE-DFT plane wave calculations, reaction paths calculated by nudged elastic band method and molecular dynamics calculations. They studied formation of several structures under MD conditions including Ti-ethylene and TiH_2. They find that while TiH_2 formation has favorable energetics, there is a reaction barrier on the order of 10 mHa that makes this reaction unfavorable. Further, they find complexes of Ti structurally similar to ethanol that bond up to 5 H_2 molecules.

Very recently, highly accurate calculations have been carried out on the Ti-ethylene-hydrogen system by Sun et al.[103] They compare DFT using a variety of functionals against CCSD(T) with MP2 geometries in determining average binding energies of $TiH_2C_2H_4 \cdot nH_2$ where n=1,2,3. Corrections for the complete basis set limit are also included. Of note is that this work also includes some calculations involving calcium on TPA (terephthalic acid) because Ca does not suffer from clustering issues like Ti. They find Ca bonds more weakly to ethylene than Ti; however, the energy is still within the low end for reversible adsorption. Of the functionals tested, they find the PBE functional very desirable for the systems they study. This work will serve as an excellent point of comparison for our results.

10.2 Bonding Mechanisms

As mentioned in the introduction, the systems studied here were chosen in part based on a bonding mechanism that results in stored intact H_2 on an intact adsorbant structure. The mechanism for this is the σ-bond complex which works through a donor-acceptor interaction between the occupied and unoccupied orbitals of a transition metal and H_2 and was first articulated by Kubas.[15] A similar kind of interaction can also occur between the carbon-carbon bond and a transition metal as will be discussed shortly. Both interactions are relevant for hydrogen on Ti-ethylene structures. A schematic diagram of the σ-bond interaction is shown at right in Fig. 10.2. The σ-bond mechanism can be understood in terms of the σ orbital of H_2 donating to an unoccupied d*-state of the TM. At the same time back donation occurs from an occupied d-state to unoccupied σ^* orbital of H_2. Upon consideration it is clear that the net effect of this interaction is to spread the charge on the H_2 away from the H_2 center. This mechanism always results in side-on bonding and an elongation of the hydrogen bond. Typical bond lengths for true σ-complex bonds are 0.8-0.9Å. It should be noted that if this interacion in hydrogen is too strong the bond can be broken so that a hydride forms.

The π-bond complex that results in a TM binding to a carbon is similar to the σ-bond interaction. A model to describe the π-bond complex was known well in advance of the mechanisim occuring between a TM and H_2 and was first described by the Dewar-Chatt-Duncanson model in the early 1950s.[109, 110] This interaction is shown schematically at left in Fig. 10.2. The main difference is that rather than σ-orbitals, now π-orbitals are involved in the interaction. Again, the donor-acceptor model applies so that the occupied π-orbitals donate to the unoccupied d*-state of the TM. At the same time back donation occurs from an occupied d-state to unoccupied π^* orbital of the carbon bond. This results in the elongation of the carbon bond.

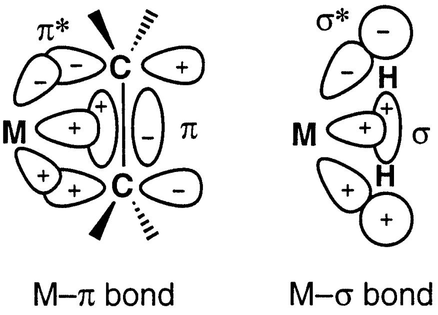

Figure 10.2: Schematic diagrams of the donor-acceptor model for σ- and π-bonding involving transition metals (M). Orbitals with an astrisk (*) indicate virtual or unoccupied orbitals. These bonding mechanisms work very similarly. The σ- and π-orbitals donate charge to the unoccupied d*-orbital of the M while the occupied d-orbital of the M back-donates charge to unoccupied σ^*- and π^*-orbitals respectively.

10.3 Methods for Hydrogen on Ti-ethylene systems

I have performed VMC and DMC calculations on several hydrogen-Ti-ethylene systems. All of these calculations use a Slater-Jastrow trial function where the single-body orbitals used in the Slater factor are derived from PBE-DFT calculations with a Gaussian 3-zeta basis using the Gaussian09.[101] In those calculations, Burkatzki-Filippi-Dolg (BFD) norm-conserving non-local pseudopotentials are used to replace the [Ne] and [He] core electrons of Ti and C respectively. The standard Coulomb potential is used for H. The QMC work was done using the QMCPACK code [53] which transforms the Gaussian radial functions onto a B-spline grid. This transformation has shown to have neglegible impact on final results while achieving a significant performance improvement. Finally, energy differences are converged for time-step error and compared to previous results.

The Jastrow factor used in this study is made up of one- and two-body terms. A detailed description of this form of trial function can be found in Chapter 5. The Jastrow allows the cusp conditions for two approaching coulomb potentials to be treated. This is necerrary because the Gaussian type orbitals used in the Slater part of the determinant are inherently unable to treat this correctly within some radius about the charge center. The two-body term addresses the electron-electron cusp conditions. Enforcing cusp-conditions for approaching electrons of identical spin is not found to be essential since the anti-symmetric property of fermions tends to keep them apart. The electron-electron Jastrow allows correlations between electrons in the trial wave function that otherwise would not be included by single-body theory alone. Besides treating the cusps, the two-body Jastrow includes correlations that result in the electrons being pushed apart. The one-body Jastrow contains all the electron-ion Jastrow terms. (It is called *one-body* because the ions can be considered as part of an external potential). In addition to treating the cusps, the one-body terms allow the spreading out of the electrons due to the two-body term to be compensated for.

The Jastrow form used throughout is that of a uniform cubic B-spline. The B-spline is partitioned with uniform knot spacings or segments and extends out to some cutoff value. The 0th, 1st, and 2nd derivitives are continuous and go to zero at the cutoff. The B-splines used in the Ti-electron, C-electron and electron-electron use a knot spacing of 0.5 Bohr and have cutoffs of 9, 7 and 8 Bohr respectively. The Jastrow used for the H-electron is somewhat different. As it is, the single-body orbitals in the Jastrow already have approximate cusp behavior, but not close to the proton where it is essential for the local-energy to remain finite. Therefore, a very short range cusp is desirable. However, it is still necerrary to have longer range behavior so that the trial function remains a reasonable description of the true ground state. This involves compensating for the electron-electron Jastrow, addressing limitations of the PBE-DFT theory and basis set. Therefore a double cusp is used for hydrogen. A short range Jastrow with a cusp is used with a 0.1 Bohr resolution and a 0.6 Bohr cutoff while a long range Jastrow with no cusp is used with a 0.5 Bohr resolution and a 10 Bohr cutoff. The larger cutoff is used for hydrogen because these atoms are mostly located on the periphery of the molecle and it is undesirable for the cutoff to occur in a region of high electron-density.

The Jastrow factor is optimized using a new stochastic method that has been developed recently by McMinis et al.[91] This method is designed to be an improvement over linear optimization method previously outlined by Toulouse and Umrigar.[90] The improvement is designed to take advantage of the bounded character of the variance in QMC calculations. The new method used here optimizes $H^2\Psi = EH\Psi$, which is essentially a vaiance equation, so that better statistics can be attained in a finite sample.

The procedure used for all the below presented results is straight forward. Calculations begin with structural optimization in PBE-DFT for several spin states. All molecular geometries involving Ti have C_{2v} symmetry. The single-body orbitals from these calculations are then used in the Slater part of the Slater-Jastrow trial function. The Jastrows are construct as described above and parameterized so as to take advantage of the symmetry in the system. At this point VMC optimization is performed with a time step of 0.25. This time step is not so important but gave an acceptance ratio of around 50%. The optimization was done over two passes (which was found to be sufficient) and generally resulted in a reduction in the variance by a factor of 8 or so. At this point DMC calculations are preformed on the resultant optimized trial function at several time steps to test for convergence. The time-steps used are 0.04, 0.02, and 0.01. Acceptence ratios for these time steps was greater than 97, 98 and 99.5% respectively. VMC results are not presented because they generally do not provide useful information with this level of Slater-Jastrow trial function. However, the DMC results are presented with convergence data.

10.4 Results

Below the results of our calculations are presented. The tables have been designed to be somewhat self explanatory, however, hopefully a few additional comments will eliminate any confusion. Table 10.1 gives PBE-DFT results for all the systems used in this present study. Note that PBE-DFT incorrectly gets the quintuplet state lower in energy than the triplet ground state (see Chap. 8 for more information). In addition, the Ti atom calculation used a 3-zeta basis that was truncated so that basis functions beyond d-states are not included. Also presented are the two lowest states of TiH_2. In PBE-DFT the $^3B_1$ state is lowest by only 1.6 mHa; however, DMC optimization results and other single point calculations have shown a smaller energy difference with $^3A_1$ a little lower in energy (but with error bars overlaping in DMC). These quantities will be used in calculating reaction energies.

The singlet, triplet and quintuplet states that could be converged in PBE-DFT have been reported along with the wave function symmetry. It should be noted that in some cases, particularily $TiH_2C_2H_4{\cdot}2H_2$ and $\cdot 3H_2$, two structures were optimized. These are denoted by an [a] or [b] next to the system name. In every case the singlet state is found to be lowest with the exception of bare TiC_2H_4, which is triplet. PBE-DFT ground state energies are again indicated in bold for each system. See Fig. 10.5 at the end of this chapter for a visualization of all the systems in Table 10.1.

It is interesting to note that for both systems $TiH_2C_2H_4{\cdot}2H_2$ and $\cdot 3H_2$ it is observed that geometry [a] has the lowest energy for the singlet state which is the ground state while [b] is optimal for the triplet state. This is somewhat explained by the geometry data which is given in Tab. 10.3. It is seen that the H-H bond length exceeds or just about exceeds 0.8Åfor all the H_2 molecules adsorbed. This is considered the threshold for true σ-bonding.

In addition, considering the PBE-DFT ground state of each structure, the bare TiC_2H_4 has a C-C bond of 1.5187Å(this seemed fairly long but is in agreement with Durgun et at.[16]). Interestingly, up until the 5$^{\text{th}}$ H_2 is added the Ti-H bond remains very close to the isolated TiH_2 bond length. One final note regarding the bond length data, the bond length of the C-H remains almost unchanged ranging from about 1.09-1.10Åso that it varies less than 1%.

Next we answer the question regarding how PBE-DFT compare to QMC. The DMC results are given it Tab. 10.4. Aside from the Ti atom and the ground state of TiH_2, the same energy ordering is observed. It is seen that the TiH_2 $^3A_1$ and $^3B_1$ states are almost on top of one another, but with $^3A_1$ now slightly lower. A more straight forward comparison of the results can be seen in Tab. 10.5 describing various reaction energies. The lines with hook-arrows represent the energy to rotate the side bonded H_2 molecules on $TiH_2C_2H_4{\cdot}2H_2$ and $\cdot 3H_2$. In order to make the raw data in these tables more understandable, see the level diagrams shown in Figs. 10.3 and 10.4. Considering the ground

System [Geometry]	PBE-DFT Optimal States and Energies (Ha)					
	Spin 0		Spin 1		Spin 2	
H_2	$^1\Sigma_g^+$	**-1.1661616989**				
Ti			^3F	-58.1765268969	$^5\mathbf{F}$	**-58.1812624443**
TiH_2			$^3A_1$	-59.3819434413		
TiH_2			$^3\mathbf{B}_1$	**-59.3835338801**		
C_2H_4	$^1\mathbf{A}_g$	**-13.7389314936**				
TiC_2H_4	$^1A_1$	-71.9586949350	$^3\mathbf{B}_1$	**-71.9725687035**	$^5A_2$	-71.9600393349
$TiH_2C_2H_4$	$^1\mathbf{A}_1$	**-73.1959118684**	$^3B_1$	-73.1679785924	$^5A_2$	-73.1419070010
$TiH_2C_2H_4{\cdot}2H_2$ [a]	$^1\mathbf{A}_1$	**-75.5550965625**	$^3B_1$	-75.5206684507	$^5A_1$	-75.4319833919
$TiH_2C_2H_4{\cdot}2H_2$ [b]	$^1A_1$	-75.5424363623	$^3B_1$	-75.5333993226	$^5B_1$	-75.4326499044
$TiH_2C_2H_4{\cdot}3H_2$ [a]	$^1\mathbf{A}_1$	**-76.7389638398**	$^3B_2$	-76.7010200213		
$TiH_2C_2H_4{\cdot}3H_2$ [b]	$^1A_1$	-76.7212680418	$^3B_2$	-76.7142993410		
$TiC_2H_4{\cdot}5H_2$	$^1\mathbf{A}_1$	**-77.8913749027**	$^3A_2$	-77.8841727344		

Table 10.1: Summary of PBE-DFT energies for all the systems studied. Energies in PBE-DFT for ethylene and various complexes of Ti and ethylene with and without additional hydrogen. Energies are given in Ha and PBE-DFT ground states are indicated in bold. Comparison is made between the different spin states with the symmetry of the state noted. The symmetry used was that found to be lowest for the given spin state. In all cases the molecular symmetry is that of the C_{2v} point group except for ethylene, Ti and H_2. Geometries are optimized individually for each system and state indicated. Triple zeta basis sets are used with aug-cc-pVTZ for hydrogen and BFD VTZ-ANO for carbon and titanium. Pseudopotentials from BFD are used for carbon and titanium while the standard Coulomb potential is used for hydrogen. Note that PBE-DFT incorrectly finds the ground state of Ti as ^5F.

state transition energies, it seems that PBE-DFT slightly overbinds by about 3.5 mHa. Also, PBE-DFT consistently gives a higher cost for rotating the side H_2 molecules.

The main disagreements between PBE-DFT and the DMC results are in the level diagrams showing the formation of $TiH_2C_2H_4$. This is in stark contrast to the agreement seen in the adsorption results (with a few less extreme exceptions). After discussing this with my research advisor Prof. Martin, it seemed notable that the DFT calculations are much more accurate for the moleculer systems despite the fact that they are so poor for the atom, even giving the wrong ground state, This can be understood from the behavior of the transition metal 3d states in other molecules[111] and solids.[112] In the atom, the states are classified by angular momentum and open shell atoms obey Hund's rule of maximum S, followed by maximum L. The degenerate orbitals with net angular momentum are not treated well in DFT since the angular momentum corresponds to a current and in principle should involve a current functional. However, in a molecule or solid the symmetry is lower and the orbital angular momentum is "quenched." For example, in a crystal cubic symmetry the orbitals split into T and E symmetries that have charge density fixed along directions in the crystal. In this case density functional theory performs very well, and the net magnetization is accounted for rather well by the spin only with no orbital component. The magnitude of the effects is similar in this case and the same reasoning is expected to carry over to Ti in all the molecules considered here.

The average formation energy per H_2 for binding 2, 3 and 4 H_2 molecules on a $TiH_2C_2H_4$ adsorbant for PBE-DFT, DMC, and resent CCSD(T) theoretical studies by Sun et al.[103] is given in Table 10.2. There is good agreement among the theories except where 4 H_2 molecules have been added. Final judjement on the performance should wait until a more extensive geometry search for $TiC_2H_4{\cdot}5H_2$ has been conducted.

Number of H_2 Adsorbed	PBE-DFT (mHa)	DMC w/PBE (mHa)	Sun et al.[103] (mHa)
2	-13.4306	-10.08(21)	-13.2
3	-14.8556	-11.26(12)	-13.6
4	-10.2720	-4.04(12)	

Table 10.2: Average formation energy per H_2 molecule for adsorption on $TiH_2C_2H_4$.

10.5 Summary and Conclusions

In conclusion, PBE-DFT is in reasonable agreement with DMC when 2 and 3 H_2 molecules are added to $TiH_2C_2H_4$. However, there is significant disagreement when the 4^{th} H_2 is added. Despite the good agreement, it seems that judgment should be somewhat restrained considering the disagreements in rotating the side H_2 molecules and the treatment of the triplet state for $TiC_2H_4{\cdot}5H_2$. Still, PBE-DFT did quite well. However, a more thorough geometry search for $TiC_2H_4{\cdot}5H_2$ is necessary. The QMC results are in good agreement with the results of Sun et al. as well.[103] The significant disagreement for the formaiton of $Ti_2C_2H_4$ may be attributable to limitations of PBE-DFT theory to treat the atom. This is especially reasonable considering how poorly PBE treats the atom. Here again it is seen that great care must be taken when applying the PBE-DFT method.

The QMC methods used here have proven successful in treating hydrogen asdorption. While a good deal of work and care is necessary in applying this method, it can give high accuracy with scaling that can carry over to larger systems. While the adsorption that occurs in this system happens on energy scales larger than physisorption, discerning the proper geometry in DMC requires resolving energies below 3.5 mHa in some cases. This is a challenge in any case but also shows how important testing the theory is.

System [Geometry]	State	Bond Lengths (Å) C−C	 C−H	 Ti−C	 Ti−H	 Ti-H_2 (side/top)	 H−H (side/top)
H_2	$^1\Sigma_g^+$						0.7509
TiH_2	$^3A_1$				1.7516		
TiH_2	$^3B_1$				1.7498		
C_2H_4	^1A_g	1.3298	1.0901				
TiC_2H_4	$^1A_1$	1.4790	1.0947	2.0250			
TiC_2H_4	$^3B_1$	1.5187	1.0985	2.0249			
TiC_2H_4	$^5A_2$	1.3908	1.0919	2.3159			
$TiH_2C_2H_4$	$^1A_1$	1.4881	1.0958	2.0274	1.7460		
$TiH_2C_2H_4$	$^3B_1$	1.3920	1.0918	2.2997	1.7620		
$TiH_2C_2H_4$	$^5A_2$	1.3895	1.0920	2.3143	1.9662		
$TiH_2C_2H_4 \cdot 2H_2$ [a]	$^1A_1$	1.4378	1.0942	2.1491	1.7442	1.8994	0.8085
$TiH_2C_2H_4 \cdot 2H_2$ [b]	$^1A_1$	1.4628	1.0912	2.0616	1.7583	2.1680	0.7662
$TiH_2C_2H_4 \cdot 2H_2$ [a]	$^3B_1$	1.3834	1.0908	2.3666	1.7600	2.0426	0.7725
$TiH_2C_2H_4 \cdot 2H_2$ [b]	$^3B_1$	1.3859	1.0933	2.3191	1.7593	1.9316	0.7998
$TiH_2C_2H_4 \cdot 2H_2$ [a]	$^5A_1$	1.3899	1.0909	2.3435	1.8655	1.9562	0.8021
$TiH_2C_2H_4 \cdot 2H_2$ [b]	$^5B_1$	1.3847	1.0956	2.3480	1.8440	1.9834	0.7999
$TiH_2C_2H_4 \cdot 3H_2$ [a]	$^1A_1$	1.4311	1.0913	2.1788	1.7497	1.8841 / 1.8492	0.8167 / 0.8383
$TiH_2C_2H_4 \cdot 3H_2$ [b]	$^1A_1$	1.3797	1.0907	2.3770	1.7651	2.0429 / 1.8755	0.7726 / 0.8403
$TiH_2C_2H_4 \cdot 3H_2$ [a]	$^3B_1$	1.4526	1.0951	2.0875	1.7630	2.1643 / 1.9385	0.7647 / 0.8122
$TiH_2C_2H_4 \cdot 3H_2$ [b]	$^3B_2$	1.3829	1.0911	2.3370	1.7609	1.9395 / 1.9163	0.7989 / 0.8186
$TiC_2H_4 \cdot 5H_2$	$^1A_1$	1.4398	1.0937	2.1471		1.8338 / 2.2832	0.8557 / 0.7589
$TiC_2H_4 \cdot 5H_2$	$^3A_2$	1.3741	1.0896	2.4331		1.8388 / 1.9532	0.8530 / 0.8058

Table 10.3: Bond length data. All bond lengths are in angstroms. The (side/top) notation refers to the [a] and [b] geometries used for $TiH_2C_2H_4 \cdot 2H_2$ and $\cdot 3H_2$. Images of these structures can be seen at the end of this chapter in Fig. 10.5.

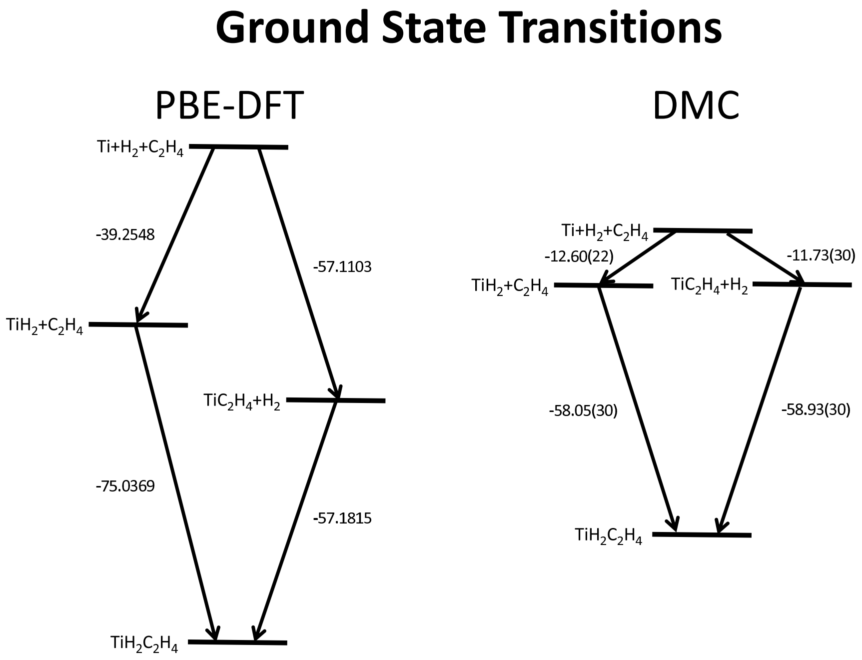

Figure 10.3: Level diagram of transitions forming $TiH_2C_2H_4$.

		DMC Energy (Ha) with time step τ		
System [Geometry]	State	$\tau = 0.04$	$\tau = 0.02$	$\tau = 0.01$
H_2	$^1\Sigma_g^+$	-1.17443(03)	-1.17440(03)	**-1.17443(03)**
Ti	^3F	-58.18286(20)	-58.18141(16)	**-58.18105(14)**
Ti	^5F	-58.15825(12)	-58.15600(13)	-58.15542(13)
TiH_2	$^3A_1$	-59.37026(19)	-59.36847(16)	**-59.36812(17)**
TiH_2	$^3B_1$	-59.36996(20)	-59.36807(17)	**-59.36799(16)**
C_2H_4	^1A_g	-13.74535(15)	-13.74418(12)	**-13.74388(14)**
TiC_2H_4	$^1A_1$	-71.92778(27)	-71.92563(24)	-71.92563(21)
TiC_2H_4	$^3B_1$	-71.93896(29)	-71.93668(24)	**-71.93666(22)**
TiC_2H_4	$^5A_2$	-71.92796(23)	-71.92744(23)	-71.92740(22)
$TiH_2C_2H_4$	$^1A_1$	-73.17146(27)	-73.16956(26)	**-73.17005(20)**
$TiH_2C_2H_4$	$^3B_1$	-73.14346(27)	-73.14346(24)	-73.14329(20)
$TiH_2C_2H_4$	$^5A_2$	-73.10612(27)	-73.10564(18)	-73.10597(25)
$TiH_2C_2H_4\cdot 2H_2$ [a]	$^1A_1$	-75.53873(30)	-75.53767(24)	**-75.53907(22)**
$TiH_2C_2H_4\cdot 2H_2$ [b]	$^1A_1$	-75.53736(28)	-75.53536(23)	-75.53560(27)
$TiH_2C_2H_4\cdot 2H_2$ [a]	$^3B_1$	-75.51441(29)	-75.51297(27)	-75.51360(29)
$TiH_2C_2H_4\cdot 2H_2$ [b]	$^3B_1$	-75.52148(26)	-75.51985(28)	-75.52057(21)
$TiH_2C_2H_4\cdot 2H_2$ [a]	$^5A_1$	-75.40417(31)	-75.40323(23)	-75.40306(21)
$TiH_2C_2H_4\cdot 3H_2$ [a]	$^1A_1$	-76.72718(29)	-76.72654(29)	**-76.72713(23)**
$TiH_2C_2H_4\cdot 3H_2$ [b]	$^1A_1$	-76.72326(28)	-76.72139(26)	-76.72046(25)
$TiH_2C_2H_4\cdot 3H_2$ [a]	$^3B_1$	-76.69749(28)	-76.69589(27)	-76.69596(25)
$TiH_2C_2H_4\cdot 3H_2$ [b]	$^3B_2$	-76.70790(32)	-76.70657(28)	-76.70722(24)
$TiC_2H_4\cdot 5H_2$	$^1A_1$	-77.88582(32)	-77.88433(25)	**-77.88394(17)**
$TiC_2H_4\cdot 5H_2$	$^3A_2$	-77.87279(47)	-77.87126(21)	-77.87153(25)

Table 10.4: The above table presents DMC convergence data for the various systems and spin states that are used in this study. The PBE-DFT results for the same systems can be found in Tab. 10.1. All energies are given in Ha and the DMC fixed-node ground state energies for our trial functions are indicated in bold. The symmetry state used is that found to be most favorable in PBE-DFT with geometry optimization. In all cases the triple zeta basis was used with aug-cc-pVTZ for hydrogen and BFD VTZ-ANO for carbon and titanium in the PBE-DFT calculations. The DMC results are for Slater-Jastrow trial function constructed from the single-body orbitals derived from the PBE-DFT calculations and Jastrow employing electron-ion and electron-electron terms. Pseudopotentials from BFD are used for carbon and titanium while the standard Coulomb potential is used for hydrogen. Convergence is tested at time-steps τ=0.04, 0.02, 0.01 and found to be converged at between τ=0.2 amd τ=0.1.

		ΔE (mHa/H_2)	
	Grond State Reactions	PBE	DMC
(a)	Ti (^{3}F) + H_2 ($^1\Sigma_g^+$) → TiH_2 ($^3A_1$)	-39.2548	-12.60(22)
(b)	Ti (^{3}F) + C_2H_4 (^1A_g) → TiC_2H_4 ($^3B_1$)	-57.1103	-11.73(30)
(c)	TiH_2 ($^3A_1$) + C_2H_4 (^1A_g) → $TiH_2C_2H_4$ ($^1A_1$)	-75.0369	-58.05(30)
(d)	TiC_2H_4 ($^3B_1$) + H_2 ($^1\Sigma_g^+$) → $TiH_2C_2H_4$ ($^1A_1$)	-57.1815	-58.92(30)
(e)	$\frac{1}{2}TiH_2C_2H_4$ ($^1A_1$) + H_2 ($^1\Sigma_g^+$) → $\frac{1}{2}TiH_2C_2H_4{\cdot}2H_2$ $^{[a]}$ ($^1A_1$)	-13.4306	-10.08(21)
	↪ $\frac{1}{2}TiH_2C_2H_4{\cdot}2H_2$ $^{[b]}$ ($^1A_1$)	6.3301	1.74(25)
(f)	$TiH_2C_2H_4{\cdot}2H_2$ $^{[a]}$ ($^1A_1$) + H_2 ($^1\Sigma_g^+$) → $TiH_2C_2H_4{\cdot}3H_2$ $^{[a]}$ ($^1A_1$)	-17.7056	-13.63(32)
	↪ $TiH_2C_2H_4{\cdot}3H_2$ $^{[b]}$ ($^1A_1$)	17.6958	6.67(34)
(g)	$TiH_2C_2H_4{\cdot}3H_2$ $^{[a]}$ ($^1A_1$) + H_2 ($^1\Sigma_g^+$) → $TiC_2H_4{\cdot}5H_2$ ($^1A_1$)	13.7506	17.62(29)
	Excited State Triplet Reactions		
(h)	TiC_2H_4 ($^3B_1$) + H_2 ($^1\Sigma_g^+$) → $TiH_2C_2H_4$ ($^3B_1$)	-29.2482	-32.16(30)
(i)	$\frac{1}{2}TiH_2C_2H_4$ ($^3B_1$) + H_2 ($^1\Sigma_g^+$) → $\frac{1}{2}TiH_2C_2H_4{\cdot}2H_2$ $^{[b]}$ ($^3B_1$)	-16.5487	-14.17(15)
	↪ $\frac{1}{2}TiH_2C_2H_4{\cdot}2H_2$ $^{[a]}$ ($^3B_1$)	6.3654	3.49(25)
(j)	$TiH_2C_2H_4{\cdot}2H_2$ $^{[b]}$ ($^3B_1$) + H_2 ($^1\Sigma_g^+$) → $TiH_2C_2H_4{\cdot}3H_2$ $^{[b]}$ ($^3B_2$)	-14.7383	-12.18(32)
	↪ $TiH_2C_2H_4{\cdot}3H_2$ $^{[a]}$ ($^3B_1$)	13.2793	11.26(35)
(k)	$TiH_2C_2H_4{\cdot}3H_2$ $^{[b]}$ ($^3B_2$) + H_2 ($^1\Sigma_g^+$) → $TiC_2H_4{\cdot}5H_2$ ($^3A_2$)	-3.7117	10.16(35)

Table 10.5: Formation energies in PBE-DFT and DMC for the various reactions are given in mHa. Negative values indicate the reaction is exothermic. Note that the hook-arrows represent transition from the above state/geometry to a new geometry (indicated as [a] or [b]). Calculations are based on results from Table 10.4. Reactions (a) through (g) are transitions between the various ground states found in DMC with PBE-DFT optimized geometries. In particular, all structures are spin 0 except for atomic Ti, TiH_2, and TiC_2H_4 which are spin 1. It should be noted that reaction (a)+(c) is identical to reaction (b)+(d), only the reaction path is different. Also, the formation energies given for reactions (e) and (i) are the average per H_2 when two hydrogen molecules are added. Reactions (h) through (k) are transitions between triplet states.

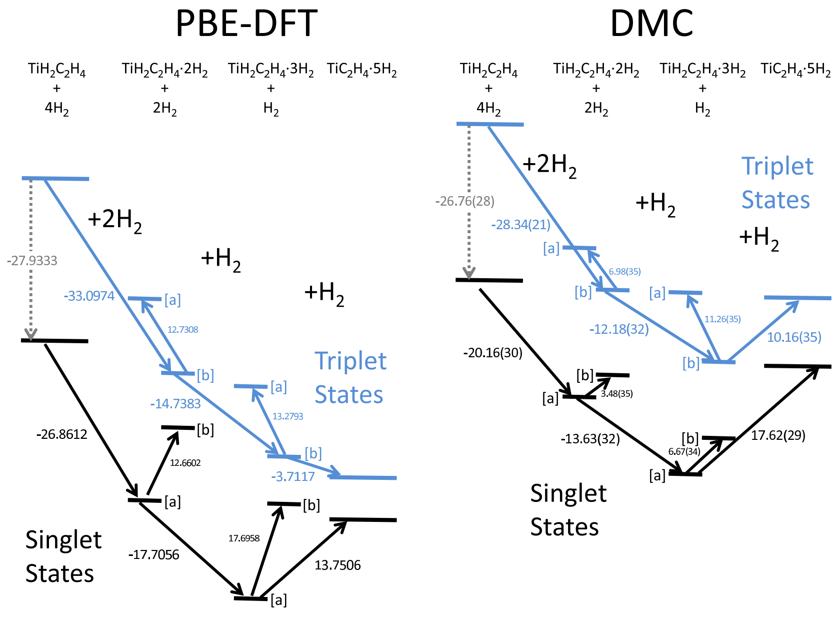

Figure 10.4: Level diagram of transitions involving adsorption and changes in geometry.

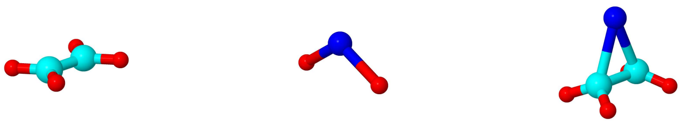

(a) C_2H_4 (b) TiH_2 (c) TiC_2H_4

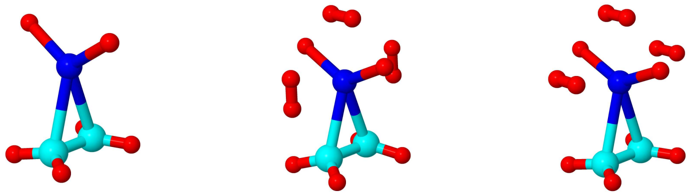

(d) $TiH_2C_2H_4$ (e) $TiH_2C_2H_4 \cdot 2H_2$ [a] (f) $TiH_2C_2H_4 \cdot 2H_2$ [b]

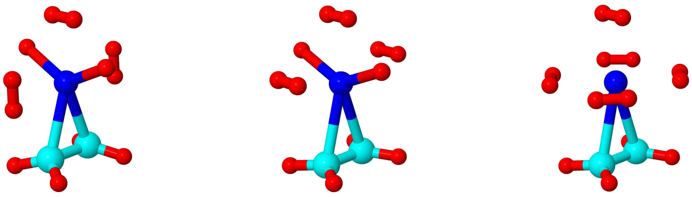

(g) $TiH_2C_2H_4 \cdot 3H_2$ [a] (h) $TiH_2C_2H_4 \cdot 3H_2$ [b] (i) $TiC_2H_4 \cdot 5H_2$

Figure 10.5: Above are the molecular structures and complexes studied. The atoms are colored such that blue, cyan, red correspond to Ti, C and H respectively. Careful distinction is made for the orientation of the side adsorbed hydrogen atoms in figures (e)-(h). When oriented vertically the geometry is denoted by an [a] while a horizontal orientation is given by [b].

Chapter 11

Conclusion

This thesis research has successfully carried out a QMC study of hydrogen adsorption on carbon and transition metal systems in the final study of hydrogen on Ti-ethylene. The research path required many steps, all of which served a purpose in qualifying the final results. The first two studies yielded results for the final adsorption study in a more general sense. The hydrogen study allowed issues regarding the Jastrow for hydrogen to be specifically understood. Those results set a template for treating new atoms as they were added to the systems being studied. It often proved somewhat challenging to decide on the cutoff for the B-spline Jastrows, however, the final result is that the cutoff should be as long as possible while still maintaining proper sampling. The next study allowed for a rigorous test of the methods used throughout in two substantial ways. First, it compared a relatively simple Slater-Jastrow (SJ) trial function to a significantly more sophisticated JAGP (Geminal) trial function. It was established that the SJ can in fact have a sufficiently good nodal surface to get accurate energy differences for the small binding energies associated with physisorption. Second, it demonstrated the feasibility of resolving binding energies under 2 mHa reliably. The hydrogen on benzene work also resulted in a publication in the Journal of Chemical Physics.

The next two studies presented were each successively more specifically relevant to the to the final adsorption study that was conducted. The atomic Ti study allowed for the testing of the BFD pseudopotential with the specific Slater-Jastrow setup used throughout this work. It was found that while PBE-DFT got the incorrect ground state, when used as a trial function in DMC very accurate energies could still be obtained. It was also shown that both PBE-DFT and UHF trial functions performed similarly so that there wasn't a strong dependence on the single-body theory used. This is essential if the QMC methods used here are to be reliable. In addition, the work on atomic Ti also gave me some needed additional experience with treating d-states and actually getting the Gaussian09 code to converge to states with which I am interested.

The TiH_2 study presented here was a tremendous learning experience and greatly added to the preparation for the final study. This work allowed for further knowledge to be gained in looking for hard to find states in the single-body methods. Also, a better understanding of the role d-states play in both the symmetry of a molecule and bonding. Constructing DMC potential energy surfaces by means of quadratic fit and comparing PBE-DFT and UHF trial functions was a rigorous test of trial function dependence in DMC. While some trial function dependence was observed, the fixed node error was on the order of less than 2 mHa in general. The error due to using the PBE-DFT optimal geometry was also established to be less than 1.5 mHa in DMC. This error partially cancels so that in practice, if the geometry is in reasonable agreement with the correct DMC geometry, this error could be lower. In that study UHF gave a linear molecule as the optimal structure which would have resulted in a significant error due to geometry. In addition, this work also found the formation energy of TiH_2 to be 12.60(22) mHa which is more likely a lower bound due to the geometry error correction. The results of this work gave a solid footing with which to proceed to the final adsorption study.

Finally, at the end of this work an adsorption study was conducted for hydrogen on Ti-ethylene. A number of structures were found using PBE-DFT theory. Applying DMC to the resultant trial functions yielded interesting results. Those results are summarized in the level diagrams given in Tables 10.3 and 10.4. Among them was fairly good agreement between PBE-DFT and DMC for the ground state adsorption transition energies. It was noted that PBE-DFT consistently was about 3.5 mHa higher in those transitions. Additionally, good agreement was found with very recent coupled cluster results.[103] However, PBE-DFT had poor agreement with QMC regarding the formation of $TiH_2C_2H_4$ and TiH_2. After significant consideration it seems that this is the result of a general failure of DFT to accurately treat atoms with proper angular momentum states. As explained in the previous chapter, when the symmetry of the atom is lowered so that its states are "quenched," DFT treats the state correctly. The energy difference between the correct treatment of the lower symmetry and the incorrect treatment of the angular momentum state is likely the cause of this issue, and in fact the error is of the proper scale. Further study regarding the adsorption of the 5th H_2 will be necessary to determine proper energetics and make a final conclusion regarding that specific structure. Also, the general result that it costs less energy to rotate the side-adsorbed hydrogens in DMC than in PBE-DFT is curious, further study of the 5th adsorbed H_2 would also show if that trend continues as well.

In all, the QMC methods used here have demonstrated great promise as a scalable alternative to other high level methods such as CCSD(T). However, great care must be taken at each step to insure that accurate results are obtained. Also, optimization of the trial function is still challenging although the recent optimization methods by Toulouse and Umrigar in conjunction with refinements by McMinis et al. have allowed for tremendous improvement in reliability.[90, 91] Optimizing geometry in DMC is even more difficult; however, a reasonably accurate PBE-DFT geometry can often be attained so as to mitigate this issue. Given the ever increasing size of parallel computing platforms and the success of QMC theory, methods like those used here may become increasingly commonplace.

References

[1] T. Graham, Philos. Trans. R. Soc. **156**, 399 (1866).

[2] T. O. Sloane, *Liquid Air and the Liquefaction of Gases*, 2^{nd} ed. (New York, Henley, 1900), chap. 11, pp. 231–285, see p. 280.

[3] R. Wiswall, *Hydrogen in Metals II. Application-Oriented Properties* volume 29 of *Topics in Applied Physics* (Springer-Verlag, 1978), chap. 5, pp. 201–242.

[4] P. Chen, J. Xiong, Zhitao amd Luo, J. Lin, and K. L. Tan, Nature **420**, 302 (2002).

[5] K. Miwa, N. Ohba, S. ichi Towata, Y. Nakamori, and S. ichi Orimo, Phys. Rev. B **71**, 195109 (2005).

[6] B. Magyari-Kope, V. Ozolins, and C. Wolverton, Phys. Rev. B **73**, 220101 (2006).

[7] C. M. Araujo, S. Li, R. Ahuja, and P. Jena, Phys. Rev. B **72**, 165101 (2005).

[8] A. C. Dillon *et al.*, Nature **386**, 377 (1997).

[9] Y. Zhao, Y.-H. Kim, A. C. Dillon, M. J. Heben, and S. B. Zhang, Phys. Rev. Lett. **94**, 155504 (2005).

[10] N. L. Rosi *et al.*, Science **300**, 1127 (2003).

[11] R. C. Lochan and M. Head-Gordon, Phys. Chem. Chem. Phys. **8**, 1357 (2006).

[12] M. Fichtner, Adv. Eng. Mater. **7**, 443 (2005).

[13] Hydrogen, Fuel Cells & Infrastructure Technologies Program Multi-Year Research, Development and Demonstration Plan section 3.3 Hydrogen Storage, Revision 1, 2005. See sec. 3.3.4.1 Technical Targets at URL http://www1.eere.energy.gov/hydrogenandfuelcells/mypp/pdfs/-storage.pdf.

[14] G. J. Kubas, Comments on Inorganic Chemistry **7**, 17 (1988).

[15] G. J. Kubas, Journal of Organometallic Chemistry **635**, 37 (2001).

[16] E. Durgun, S. Ciraci, W. Zhou, and T. Yildirim, Phys. Rev. Lett. **97**, 226102 (2006).

[17] T. D. Beaudet, M. Casula, J. Kim, S. Sorella, and R. M. Martin, The Journal of Chemical Physics **129**, 164711 (2008).

[18] M. Casula, Phys. Rev. B **74**, 161102 (2006).

[19] M. Burkatzki, C. Filippi, and M. Dolg, The Journal of Chemical Physics **129**, 164115 (2008).

[20] J. C. Slater, Phys. Rev. **34**, 1293 (1929).

[21] V. Fock, Zeitschrift fr̈ Physik A Hadrons and Nuclei **61**, 126 (1930).

[22] A. Szabo and N. S. Ostlund, *Modern Quantum Chemistry: Introduction to Advanced Electronic Structure Theory* (Dover Publications, Inc., Mineola, New York, 1996), note: This is an unaltered republication of the "First Edition, Revised" originally published in 1989 by the McGraw-Hill Publishing Company, New York.

[23] P. Hohenberg and W. Kohn, Phys. Rev. **136**, B864 (1964).

[24] W. Kohn and L. J. Sham, Phys. Rev. **140**, A1133 (1965).

[25] M. C. Payne, M. P. Teter, D. C. Allan, T. A. Arias, and J. D. Joannopoulos, Rev. Mod. Phys. **64**, 1045 (1992).

[26] R. M. Martin, *Electronic Structure: Basic Theory and Practical Methods* (Cambridge University Press, 2004).

[27] P. A. M. Dirac, Mathematical Proceedings of the Cambridge Philosophical Society **26**, 376 (1930).

[28] D. M. Ceperley and B. J. Alder, Phys. Rev. Lett. **45**, 566 (1980).

[29] J. P. Perdew, K. Burke, and M. Ernzerhof, Phys. Rev. Lett. **77**, 3865 (1996).

[30] J. P. Perdew, K. Burke, and M. Ernzerhof, Phys. Rev. Lett. **78**, 1396 (1997).

[31] A. D. Becke, The Journal of Chemical Physics **98**, 5648 (1993).

[32] C. Lee, W. Yang, and R. G. Parr, Phys. Rev. B **37**, 785 (1988).

[33] B. Miehlich, A. Savin, H. Stoll, and H. Preuss, Chemical Physics Letters **157**, 200 (1989).

[34] S. F. Boys and F. Bernardi, Mol. Phys. **19**, 553 (1970).

[35] S. Simon, M. Duran, and J. J. Dannenberg, The Journal of Chemical Physics **105**, 11024 (1996).

[36] J. Olsen, B. O. Roos, P. Jørgensen, and H. J. A. Jensen, The Journal of Chemical Physics **89**, 2185 (1988).

[37] R. J. Bartlett and M. Musia, Rev. Mod. Phys. **79**, 291 (2007).

[38] F. Coester and H. Kümmel, Nuclear Physics **17**, 477 (1960).

[39] E. F. Valeev and T. D. Crawford, The Journal of Chemical Physics **128**, 244113 (2008).

[40] C. Møller and M. S. Plesset, Phys. Rev. **46**, 618 (1934).

[41] M. Head-Gordon, J. A. Pople, and M. J. Frisch, Chemical Physics Letters **153**, 503 (1988).

[42] W. L. McMillan, Phys. Rev. **138**, A442 (1965).

[43] D. Ceperley, G. V. Chester, and M. H. Kalos, Phys. Rev. B **16**, 3081 (1977).

[44] W. M. C. Foulkes, L. Mitas, R. J. Needs, and G. Rajagopal, Rev. Mod. Phys. **73**, 33 (2001).

[45] B. L. Hammond, W. A. Lester, Jr, and P. J. Reynolds, *Monte Carlo Methods in Ab Initio Quantum Chemistry* volume 1 of *World Scientific Lecture and Course Notes in Chemistry* (World Scientific Publishing Co. Pte. Ltd., 1994).

[46] N. Metropolis, A. W. Rosenbluth, M. N. Rosenbluth, A. H. Teller, and E. Teller, J. Chem. Phys. **21**, 1087 (1953).

[47] M. Casula, C. Filippi, and S. Sorella, Phys. Rev. Lett. **95**, 100201 (2005).

[48] S. Sorella, M. Casula, and D. Rocca, J. Chem. Phys. **127**, 014105 (2007).

[49] D. R. Hamann, M. Schlüter, and C. Chiang, Phys. Rev. Lett. **43**, 1494 (1979).

[50] S. Fahy, X. W. Wang, and S. G. Louie, Phys. Rev. B **42**, 3503 (1990).

[51] D. F. B. ten Haaf, H. J. M. van Bemmel, J. M. J. van Leeuwen, W. van Saarloos, and D. M. Ceperley, Phys. Rev. B **51**, 13039 (1995).

[52] Kenneth P. Esler Jr., einspline, Carnegie Institution of Washington, http://einspline.sourceforge.net.

[53] J. Kim, *et al.*, QMCPACK, Materials Computation Center. Code available for download at http://code.google.com/p/qmcpack/.

[54] J. Bardeen, L. N. Cooper, and J. R. Schrieffer, Phys. Rev. **106**, 162 (1957).

[55] J. R. Schrieffer, *Theory of Superconductivity* (W. A. Benjamin, Inc., 1964).

[56] L. C. Pauling, *The Nature of the Chemical Bond*, 3rd ed. (Cornell University Press, 1960).

[57] M. Casula, C. Attaccalite, and S. Sorella, J. Chem. Phys. **121**, 7110 (2004).

[58] S. Sorella, M. Casula, and D. Rocca, cond-mat/0702349v1 (2007).

[59] M. Casula and S. Sorella, unpublished.

[60] J. P. Bouchaud, A. Georges, and C. Lhuillier, Journal of Physics (Paris) **49**, 553 (1988).

[61] M. Casula, *New QMC approaches for the simulation of electronic systems: a first application to aromatic molecules and transition metal compounds*, PhD thesis, Scuola Internazionale Superiore di Studi Avanzati (SISSA), Trieste, Italy, 2005.

[62] S. Fournais, M. Hoffmann-Ostenhof, T. Hoffmann-Ostenhof, and T. Ø. Sørensen, Comm. Math. Phys. **255**, 183 (2005).

[63] W. Kolos and L. Wolniewicz, The Journal of Chemical Physics **43**, 2429 (1965).

[64] M. J. Frisch *et al.*, Gaussian 03, Revision C.02, Gaussian, Inc., Wallingford, CT, 2004.

[65] M. Burkatzki, C. Filippi, and M. Dolg, J. Chem. Phys. **126**, 234105 (2007).

[66] R. A. Kendall, J. Thom H. Dunning, and R. J. Harrison, J. Chem. Phys. **96**, 6796 (1992).

[67] L. K. Wagner and L. Mitas, J. Chem. Phys. **126**, 034105 (2007).

[68] M. R. Hestenes and E. Stiefel, Journal of Research of the National Bureau of Standards **49**, 409 (1952).

[69] S. Sorella, Phys. Rev. B **64**, 024512 (2001).

[70] C. J. Umrigar, J. Toulouse, C. Filippi, S. Sorella, and R. G. Hennig, Phys. Rev. Lett. **98**, 110201 (2007).

[71] S. Sorella, *et al.*, TurboRVB, SISSA, http://www.sissa.it.

[72] S. Sorella, Phys. Rev. B **71**, 241103 (2005).

[73] C. J. Umrigar and C. Filippi, Phys. Rev. Lett. **94**, 150201 (2005).

[74] S. Hamel and M. Côté, J. Chem. Phys. **121**, 12618 (2004).

[75] O. Hübner, A. Glöss, M. Fichtner, and W. Klopper, J. Phys. Chem. A **108**, 3019 (2004).

[76] D. Feller and D. Dixon, J. Phys. Chem. A **104**, 3048 (2000).

[77] K. P. Huber and G. Herzberg, *Molecular Spectra and Molecular Structure IV. Constants of Diatomic Molecules* (Van Nostrand Reinhold Co., 1976).

[78] W. Kolos and L. Wolniewicz, J. Chem. Phys. **49**, 404 (1968).

[79] L. K. Wagner, Journal of Physics: Condensed Matter **19**, 343201 (13pp) (2007).

[80] O. V. Pupysheva, A. A. Farajian, and B. I. Yakobson, Surf. Sci. **8**, 767 (2008).

[81] Q. Wang and J. K. Johnson, The Journal of Chemical Physics **110**, 577 (1999).

[82] L. Mattera *et al.*, Surface Science **93**, 515 (1980).

[83] A. D. Crowell and J. S. Brown, Surface Science **123**, 296 (1982).

[84] M. Dion, H. Rydberg, E. Schröder, D. C. Langreth, and B. I. Lundqvist, Phys. Rev. Lett. **92**, 246401 (2004).

[85] T. Thonhauser *et al.*, Phys. Rev. B **76**, 125112 (2007).

[86] E. L. Shirley, R. M. Martin, G. B. Bachelet, and D. M. Ceperley, Phys. Rev. B **42**, 5057 (1990).

[87] W. A. Al-Saidi, H. Krakauer, and S. Zhang, Phys. Rev. B **73**, 075103 (2006).

[88] D. J. Griffiths, *Introduction to Quantum Mechanics* (Prentice Hall, New Jersey, 1994), note: See Sec. 4.3.

[89] Energy-consistent pseudopotentials for QMC calculations, M. Burkatzki, C. Filippi and M. Dolg. Pseudopotentials and basis sets available at URL http://burkatzki.com/pseudos/index.2.html.

[90] J. Toulouse and C. J. Umrigar, The Journal of Chemical Physics **126**, 084102 (2007).

[91] J. McMinis, M. A. Morales, J. Kim, and D. M. Ceperley, unpublished, 2010.

[92] Z. L. Xiao, R. H. Hauge, and J. L. Margrave, The Journal of Physical Chemistry **95**, 2696 (1991).

[93] G. V. Chertihin and L. Andrews, Journal of the American Chemical Society **116**, 8322 (1994).

[94] J. Demuynck and H. F. S. III, The Journal of Chemical Physics **72**, 311 (1980).

[95] J. Tyrrell and A. Youakim, Journal of Physical Chemistry **84**, 3568 (1980).

[96] J. Tyrrell and A. Youakim, Journal of Physical Chemistry **85**, 3614 (1981).

[97] T. Kudo and M. S. Gordon, The Journal of Chemical Physics **102**, 6806 (1995).

[98] T. S. Fujii and S. Iwata, Chemical Physics Letters **251**, 150 (1996).

[99] B. Ma, C. L. Collins, and H. F. Schaefer, Journal of the American Chemical Society **118**, 870 (1996).

[100] J. A. Platts, Journal of Molecular Structure: THEOCHEM **545**, 111 (2001).

[101] M. J. Frisch *et al.*, Gaussian 09 Gevision A.1, Gaussian Inc. Wallingford CT 2009.

[102] J. Harris, Phys. Rev. B **31**, 1770 (1985).

[103] Y. Y. Sun *et al.*, Phys. Rev. B **82**, 073401 (2010).

[104] H.-G. Cho and L. Andrews, The Journal of Physical Chemistry A **111**, 5201 (2007), PMID: 17523604.

[105] A. B. Phillips and B. S. Shivaram, Phys. Rev. Lett. **100**, 105505 (2008).

[106] A. B. Phillips and B. S. Shivaram, Nanotechnology **20**, 204020 (2009).

[107] T. Yildirim and S. Ciraci, Phys. Rev. Lett. **94**, 175501 (2005).

[108] W. Zhou, T. Yildirim, E. Durgun, and S. Ciraci, Phys. Rev. B **76**, 085434 (2007).

[109] M. Dewar, Bull. Soc. Chim. Fr. **18**, C79 (1951).

[110] J. Chatt and L. A. Duncanson, J. Chem. Soc. **111**, 2939 (1953).

[111] F. A. Cotton, *Exchange Interactions among Itinerant Electrons* (Wiley, New York, 1990).

[112] W. C. Herring, *Exchange Interactions among Itinerant Electrons* (Academic Press, New York, 1966).

Vita

Todd David Beaudet received his B.A. with Distinction in Physics from Hamline University in 2002 and an M.S. in Physics from the University of Illinois at Urbana-Champaign in 2006.